



POLITECNICO DI MILANO
DEPARTMENT OF ELECTRONICS, INFORMATION AND
BIOENGINEERING
DOCTORAL PROGRAM IN BIOENGINEERING

Optimized curvilinear path planning and pose estimation for a programmable bevel-tip needle in keyhole neurosurgery

Doctoral Dissertation of:
Alberto FAVARO
865323

Supervisors:

Prof. Elena DE MOMI

Prof. Ferdinando RODRIGUEZ Y BAENA

Tutor:

Prof. Chiara GUAZZONI

The Chair of the Doctoral Program:

Prof. Andrea ALIVERTI

Politecnico di Milano
Department of Electronics, Information and Bioengineering
Doctoral Program in Bioengineering

Abstract

Optimized curvilinear path planning and pose estimation for a programmable bevel-tip needle in keyhole neurosurgery

by Alberto FAVARO

Over the last decades, a great interest has been shown towards the development of flexible steerable needles in minimally invasive surgery.

These needles feature complex kinematics that hinders the possibility to plan the insertion trajectories unless with the aid of an automatic path planner. Solutions proposed in the literature for automatic steerable needle path planning in 3D focus either on a fast computation to allow the interactive re-planning or on path optimality at the expense of high computational time.

The needle motion plan can be executed by a robotically-assisted insertion platform. During the needle insertion, the control system needs to know the needle position and orientation in order to address for possible needle torsion that has been experimentally proven to affect percutaneous needles undermining the insertion accuracy. Because of the thin needle diameter, current tracking systems can not sense the torsion of the needle about its insertion axis.

On this background, the overall goal of this PhD thesis is to describe a pre-operative curvilinear path planner for steerable needles and to design a solution for estimating the needle tip position and orientation (i.e. the full pose) during the insertion.

In particular, the contributions of this PhD work are:

1. *A pre-operative curvilinear path planner for steerable needles able to solve the planning problem computing a kinematically-feasible path. The planner optimizes the solution according to the criteria of minimum path length and maximum obstacle clearance keeping the computational time consistent with standard pre-operative planning algorithms.*

To contextualize the planning problem with respect to the state of the art, a literature review on path planning for steerable needles is reported, with a focus on the widely used sampling-based methods.

A pre-operative curvilinear path planner is then presented. Through a bespoke evolutionary optimization, the planner can maximize the obstacle avoidance while minimizing the path length. In addition, by defining the subspace of reachability of the needle and confining the path search within this region, the algorithm achieves a computational time consistent with standard pre-operative planners. The solution was validated through multiple simulated needle insertions in a neurosurgical scenario.

2. *An on-line pose estimation solution for a multi-segment steerable needle using position measurement from sensors mounted on the needle tip.*

A solution for the accurate estimation of the needle pose is presented, based on the kinematic model of the needle and position tracking data. The position of the needle segment tips are retrieved by electromagnetic sensors and used by a kinematic-based prediction method to correct the needle state estimation and infer the angle of needle torsion. The method was tested on a two-segment steerable needle in simulation and in phantom-brain gelatine. A reliable and robust estimation was demonstrated with position and orientation errors consistent with the state of the art. The solution was later extended to a four-segment needle. In-gel validation shown the feasibility of the method although, in the latter case, a long time of convergence was evidenced for the torsion angle.

The Programmable Bevel-tip Needle (PBN) is a multi-segment steerable needle under development within the EU EDEN2020 project. It is composed of four axially-interlocked slender sections, robotically actuated to develop specific tip configurations that allow the needle to steer in the space. In this PhD dissertation, the PBN is considered as a case study for the presented methods.

Acknowledgements

I want to thank my family for the huge support provided during these four years. Your presence, love and unconditioned trust were precious in facing the demanding moments of this journey as well as in celebrating the happy ones.

I'd like to thank my supervisor, Prof. Elena De Momi, for her help, support and understanding. You always pushed me to do my best with your strong passion and enthusiasm.

Thanks to Prof. Rodriguez Y Baena for hosting me in his Lab, and thanks to the MiM Lab people: you accepted me as a colleague and as a friend, the time spent with you was precious.

Thanks to my friends and colleagues at NearLab for the innumerable happy moments, the friendly support, the talks, the laughs, the happy hours and the meaningful experiences lived together.

From the bottom of my heart,
Thank you

Contents

1	Introduction	1
1.1	Problem statement and motivation	1
1.1.1	Steerable needles for minimally invasive surgery	1
1.1.2	The Programmable Bevel-tip Needle (PBN)	2
1.1.3	Path planning	2
1.1.4	Needle control and tracking	4
1.1.5	The PBN control framework	5
1.2	Aim of the thesis	5
2	Sampling-based path planning for steerable needles in MIS	9
2.1	Introduction	9
2.2	Problem formulation	12
	Path planning in minimally invasive surgery	13
2.3	Single-query planners	14
2.3.1	Solutions based on RRT	14
2.3.2	Solutions based on RRT-Connect	16
2.3.3	Solutions based on RG-RRT and similar	16
2.3.4	Solutions based on RRT*	19
2.4	Multi-query planners	20
2.5	Conclusions	22
3	An evolutionary-optimized path planner for a PBN	25
3.1	Introduction	26
3.2	Related works	28
3.2.1	Graph-based methods	28
3.2.2	Sampling-based methods	29

3.3	Methods	31
3.3.1	Surgeon's input and patient's data elaboration	31
3.3.2	Path planning	33
3.3.3	Path approximation and optimization	36
	Population initialization	37
	Objective function	37
	Parent selection method	39
	Crossover	40
	Mutation	41
3.3.4	Exhaustive search for the best path	41
3.4	Experimental protocol	42
3.4.1	Input dataset	42
3.4.2	Simulations and data analysis	46
	Performance evaluation	46
	Computational time	47
3.5	Results	48
3.6	Discussion	51
3.7	Conclusions	53
4	Model-based pose estimation for a PBN	55
4.1	Introduction	56
4.2	Methods	59
4.2.1	Two-segment PBN (sPBN)	59
	Kinematic model	59
	Torsion model	61
	Pose estimation	63
4.2.2	Four-segment PBN	66
	Kinematic model	66
	Torsion model	71
	Pose estimation	71
4.3	Experimental Protocol	73
4.3.1	Two-segment PBN (sPBN)	73
	Simulation study	73
	Geometric approach for pose estimation	77

	In-gel experiments	78
4.3.2	Four-segment PBN	81
	In-gel experiments	81
	Geometric approach for pose estimation	81
4.4	Results	82
4.4.1	Two-segment PBN (sPBN)	82
	Simulation study	82
	In-gel experiments	82
4.4.2	Four-segment PBN	86
	In-gel experiments	86
4.5	Discussions	88
4.5.1	Two-segment PBN (sPBN)	88
4.5.2	Four-segment PBN	89
4.6	Conclusion and future developments	90
5	Conclusions	93
5.0.1	Thesis contribution	94
5.0.2	Impact and future perspective	96
5.1	Scientific publications	97
5.1.1	Journal publications	97
5.1.2	Conference proceedings	97
6	Appendices	99
6.1	Discretization of the independent variable u	99
6.2	Mutation algorithm	99
	Bibliography	103

List of Figures

1.1	In a), the cross section of the PBN with the interlocking mechanism is reported. The four needle sections are highlighted in different colors. In b), a possible PBN configuration during needle insertion is presented.	3
1.2	In the schematic, the different agents included in the robot-assisted PBN insertion framework are presented.	6
1.3	Graphical abstract of the PhD thesis. The research hypotheses that guide this PhD work are presented, along with the performed activities and the solutions employed to validate the proposed methods.	8
2.1	Schematic representation of the sampling-based planning methods.	11
3.1	Schematic representation of the workflow. The surgeon is asked to define the entry (EP_0) and the target point (TP) on the patient dataset. The Entry Area (a) is then computed and the set of possible entry points $EP_{i,a}$, $i \in 1, \dots, N_a$ is defined. Subsequently, for each $EP_{i,a}$, the algorithm performs the path planning (Section 3.3.2) and the Evolutionary Optimization Procedure (Section 3.3.3). A number of feasible solutions $\overline{\text{ind}}_j^{i,a}$ are generated. For each $EP_{i,a}$, the best path $\overline{\overline{\text{ind}}}^{i,a}$ is computed and eventually provided to the surgeon by running a cost function over the set of solutions generated by the EOP (Section 3.3.4).	32

- 3.2 A 2D representation of the Kinematics Search Volume (KSV). The insertion happens at the entry point (EP). Part \mathcal{C} can not be reached by the PBN due to the minimum bending radius and it is part of the unfeasible area. KSV is represented in gray. Its superior half-plane derives from the combination of two areas: \mathcal{A} and \mathcal{B} . These can be identified as the combination and intersection of the circumferences centered in $\mathbf{A}(x_A = 0, y_A = r)$, $\mathbf{B}(x_B, y_B)$ and the TP. The rest of the space is labelled as "unfeasible" as it can not generate any feasible trajectory to reach the TP. The value r represents the minimum bending radius admitted by the PBN and θ the insertion orientation. 34
- 3.3 In the diagram, the steps composing the EOP are depicted. The initial piece-wise linear solution ($\text{sol}_j^{i,a}$) is provided to the EOP, and the initial population of individuals is generated by providing random values to the $w_{k,t}^{j,i,a}$. F_{obj} is then run and the parent selection is carried out as explained in Sec. 3.3.3. Then the crossover (Sec. 3.3.3) and the mutation (Sec. 3.3.3) happen, according to each specific probability. The population is then updated. The process continues until a predefined number of iteration (N_{max}^{iter}) is achieved and the fittest individual ($\overline{\text{ind}}_j^{i,a}$) is returned as output. 38
- 3.4 The controlled mutation algorithm. In *a*), where part of the curve results too close to an obstacle (red points over the grey line), i.e $\{P_o\} \neq \emptyset$, the weight of $\mathbf{P}_k^{j,i,a}$ that affects that part of the curve is decreased until obstacle avoidance is obtained (green line). In *b*), the weights $\mathbf{P}_k^{j,i,a} \in \text{ind}_t^{j,i,a}$ are decreased in order to smooth the curve. 40
- 3.5 In the uppermost figure, the EOP is presented. Three piece-wise linear solutions are depicted in black ($\text{sol}_{1,\dots,3}$), along with multiple curvilinear approximations ($\text{ind}_t^{j,i,a}$) in red. The best solution for each sol_j is reported in green as $\overline{\text{ind}}_j^{i,a}$. In the picture underneath, referred as "Exhaustive search for the best path", the cost function described in Section 3.3.4 is implemented to define, among the 3 $\overline{\text{ind}}_{1,\dots,3}^{i,a}$, the best one: $\overline{\overline{\text{ind}}}^{i,a}$ 43

- 3.6 In a) a picture of the 10 entry areas defined on the brain cortex for the scope of the test (5 on the left and 5 on the right hemisphere) is presented. In b), the anatomical obstacles considered in the planning phase are depicted in different colors: ventricles (blue), thalamus (yellow), globus pallidus (green) and blood vessels (red). In c), an example of a planned curvilinear path is proposed (sharp red). The entry and target points are labelled respectively as EP and TP. The entry area is also shown in sharp green around the EP. 45
- 3.7 Results from the comparison between the presented solution (the KSV) and other two methods proposed in the literature: the ellipsoidal search method proposed in Favaro et al., 2018b (referred as "*Ellips.*") and the RG-RRT. The maximum curvature (k_{max}), the minimum and mean distance from anatomical obstacles (d_{min} , \bar{d}), the normalized path length (\hat{l}) and the overall cost (F_{cost}) are reported respectively in *a,b,c,d* and *e*. In *f*), the failure rate FR is also shown. Statistical significance between different algorithms is highlighted ($*, p < 0.05$). 50
- 4.1 *Needle kinematics*: in a), a 2D representation of the two-segment SPBN is reported. \mathbf{X}_A and \mathbf{X}_B represent the local frames of segment A and segment B. In the case depicted, $\mathbf{X}_A = \mathbf{X}_l$ and $\mathbf{X}_B = \mathbf{X}_r$. R_n is the needle radius and δ the offset at the needle base. ψ is the rotation of the needle about the z-axis. The offset at the tip, δ_t , differs from δ because of the needle bend, which generates a further curvature ξ associated to a radius R_c . In b), the effect of needle torsion on the original 2D trajectory of segment A and B, depicted on the x-y plane in light blue and light yellow, is reported. The needle moves from planar steering to a spatial movement. The local reference frames of segment A and segment B are reported. The offset between the leading segment (here the segment A) and the rear segment (here the segment B) determines a different torsion on their tips, i.e. $\phi_A \neq \phi_B$ 62

- 4.2 *Needle kinematics:* In a) the two 2D systems S_H and S_V are presented. The two segments composing S_H are in blue and yellow, while the two composing S_V are in green and white. The rear segments $\mathbf{X}_{r,V}$ and $\mathbf{X}_{r,H}$ as well as the leading segments $\mathbf{X}_{l,V}$ and $\mathbf{X}_{l,H}$ are shown. The two steering angles (ψ, θ) defined by δ_H and δ_V are plotted, together with the curvature radii and the angle ξ_V and ξ_H . The picture in b) shows the 3D representation of the four-segment PBN during insertion. All four segments are presented, identified by a unique number and color. The frames $\mathbf{X}_{1,...,4}$ are shown. In this case, $\mathbf{X}_r = \mathbf{X}_1$. ψ_1 is the torsion affecting segment 1. The offsets δ_{t_i} at the level of the needle tip are presented (as $\mathbf{X}_r = \mathbf{X}_1, \delta_{t_1} = 0$). On the left and on the bottom of the picture, the respective ideal 2D projections are depicted on the xz and xy planes. The angles ξ_{v_i} and ξ_{h_i} can be identified in the figure. The projections refer to the needle without torsion, moreover, as $\mathbf{X}_r = \mathbf{X}_1, \xi_{v_1} = \xi_{h_1} = 0$ 70
- 4.3 In a) the evolution of the offset velocities (v_2) for the four simulated insertions is shown over time. In b), the incremental step of needle rotation is shown with respect to the offset at the tip. In c), the trend of ϕ for one simulated insertion is depicted over the insertion length for segment A and B. In d), the resulting 3D reconstruction of the needle shape. In d), a schematic of the main entities coming into play in the geometric approach is presented. In e), a representation of the geometric approach discussed in Section 4.3.1 is shown. 75
- 4.4 *Experimental setup:* the PBN is inserted into gelatin and tracked by the EM field generator through the EM sensors mounted on the needle. An actuation box controls each segment of the PBN and encoders measure their insertion length. On the bottom left, a magnification of the needle insertion. 80

- 4.5 *Simulation results:* the graphs show the Euclidean and orientation errors (E_t , E_r) from the simulation trials at different values of noise σ . Results from the EKF and the geometrical approach are shown respectively in the left and right columns. As a yardstick, the 5 deg error tolerance is plotted, with the exception of the θ and ψ angles of the EKF where E_r is too small. Please note that the span of the y axis is different between the two methods for the θ and ψ angles. 83
- 4.6 *In-gel results:* on the top, the original position data from the EM sensors are shown for Trial 1, along with the needle reconstruction obtained from the EKF pose estimation. In the graphs below, on the left side the comparison between the original EM position and the one estimated by the EKF is presented. The graphs on the right, instead, allow to compare the estimated orientation with respect to the one calculated by the geometric approach, considered as gold standard. A close look at the angles estimated by the two methods is possible through the three magnification windows. 85
- 4.7 *In-gel results:* In the figure, the results from 3 PBN insertions in gelatin are presented. In the left part, the raw position measurements from the 4 EM sensors are plotted. Nearby, the reconstructions of the needle obtained from the position and orientation estimated by the EKF are presented. In the top-left corner, the CAD model used for the reconstruction is shown. On the right, the graphs report the estimated position and orientation for each insertion along with the original EM data and the orientation resulting from the geometric pose computation . . . 87

List of Tables

3.1	Parameters used in the experimental setup. From the left to the right, the PBN diameter and maximum degree of curvature are reported, followed by a the pre-set maximum number of raw path (N_{sol}^{max}) allowed at each iteration of Section 3.3.2. The EOP is defined by the initial population size N_t . The number of offspring (N_{max}^{iter}), the cross-over and mutation probabilities (P_{cross} and P_{mut}) as well as the value assigned to the selective pressure (SP) are also reported. Lastly, the values of the weight used in the Objective and the Cost functions are shown.	44
3.2	Performance test between A* algorithm and the presented solution in term of normalized path length, minimum and mean distance from obstacles and computational time as 25^{th} , 50^{th} and 75^{th} percentiles.	49
3.3	Results in term of computational time are shown for an ellipsoidal and a KSV searching space as 25^{th} , 50^{th} and 75^{th} percentiles. Statistical significance effect of the type of search space has been found through a Wilcoxon matched pairs test ($p < 0.05$). 49	
4.1	Parameters and dimensions used in the simulation trials.	74
4.2	Results from the in-gel trials. Position error E_t is computed with respect to the original EM data. Orientation error E_r is computed with respect to the orientation measured by geometric approach, considered as gold standard. For each index of performance, the 25^{th} , 50^{th} , 75^{th} quantiles are presented.	84

Chapter 1

Introduction

1.1 Problem statement and motivation

1.1.1 Steerable needles for minimally invasive surgery

Minimally invasive surgery (MIS) is widely adopted in the clinical and surgical practice for its advantages with respect to the standard open surgery in terms of patient safety, reduced tissue trauma and faster recovery time. Percutaneous interventions are MIS techniques that involve the insertion of thin devices (needles, catheters, electrodes, etc.) through the skin to reach a desired target location in the patient's body for therapeutic or diagnosis purposes (Abolhassani, Patel, and Moallem, 2007). Examples of percutaneous interventions are biopsies, brachytherapy interventions for radioactive seeds placements, drug delivery, thermal ablation and Deep Brain Stimulation (DBS).

Percutaneous devices used in clinical practice generally consist of straight tools, inserted following rectilinear trajectories. In the last decades, a great interest has been shown towards the development of flexible steerable needles whose design allows them to steer in the tissues. This property can be used to perform curvilinear insertion trajectories increasing the distance from sensitive anatomical structures that must be preserved as well as enlarging the number of possible insertion pathways in cluttered anatomical environments that would otherwise prevent the tool deployment if standard rectilinear paths are used.

1.1.2 The Programmable Bevel-tip Needle (PBN)

The Programmable Bevel-tip Needle (PBN) (Watts, Secoli, and Baena, 2019) is a flexible needle under development within the EU EDEN2020 project designed for percutaneous interventions in neurosurgery (drug infusion and in-situ optical diagnosis). The PBN is manufactured with four axially-interlocked slender sections, robotically actuated at the needle base so that to slide over one another along the main needle direction. The needle has a diameter of 2.5 mm and each section features a 0.3 mm outer diameter hollow lumen which can be used to perform drug delivery, cyst evacuation or optical-based diagnostic sensing (see Fig. 1.1a). The tip of each segment is ground in a way to form a beveled profile with an angle of approximately 30° from the needle neutral insertion axis. Further details about PBN manufacture can be found in Watts, Secoli, and Baena, 2019. The needle tip changes according to the offset generated between adjacent sections and determines the steering direction and the degree of curvature. A rendering of the PBN is shown in Fig. 1.1b. The PBN is considered as a case study for the methods described in this PhD dissertation.

1.1.3 Path planning

The increased dexterity shown by steerable needles with respect to their rigid counterparts gives them the possibility to perform a larger number of pathways for the same planning problem. Also, in case of cluttered working scenarios, the ability to steer around the obstacles allows them to reach the target in conditions where straight needles will have no chance of success.

The complex steerable needles kinematics hinders the possibility to plan the insertion trajectories unless with the aid of an automatic path planner. Such a planner should be able to account for the hard constraints related to the needle's kinematic as well as the constraints defined by the surgeon in terms of anatomical obstacles to avoid during the insertion. This generally takes the shape of a multi-objective planning problem where, in addition to the hard constraints described above, other optimality criteria are generally included: the minimization of the surgical path length and the maximization of the clearance from anatomical obstacles can be considered as general axioms

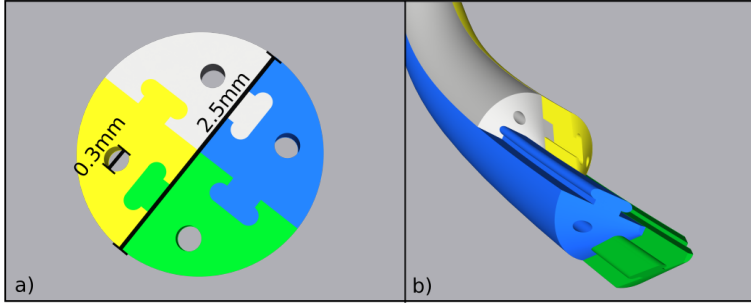


FIGURE 1.1: In a), the cross section of the PBN with the interlocking mechanism is reported. The four needle sections are highlighted in different colors. In b), a possible PBN configuration during needle insertion is presented.

in steerable needle path planning, aiming at reducing the tissue damage and providing a safety margin in case the needle deviates from the planned path. In neurosurgical applications, Essert et al., 2012 formalized these principles in the shape of hard and soft constraints used by neurosurgeons in selecting the best insertion path for DBS electrodes.

When coping with path planning, the majority of the solutions presented in the literature focus either on a fast computation or on path optimality with respect to specific criteria. In the first case, the quick planning allows the intra-operative adjustment of the plan in case insertion errors arise because of uncertainties in needle motion or in the environment (e.g. deformations, obstacles and target movements) at the expense of a sub-optimal planning. In the second case, path optimality can be found but the computational time needed for its computation becomes unbearable in case of 3D environments. Also, solutions are often tested in simulated environments with simplified geometrical obstacles (Duindam et al., 2010; Patil and Alterovitz, 2010; Torres and Alterovitz, 2011) which are far from being representative of the complexity of real anatomical scenarios. Liu et al., 2016 proposed a method suited

for the PBN and based on fractal theory which exploits the architecture of graphics processing units to achieve sub-optimal path planning but at an interactive rate. The solution was then extended by Pinzi, Galvan, and Rodriguez y Baena, 2019 including optimized geometric Hermite curves to perform a path computation accounting also for the needle orientation at the target point. At the moment, no solution exists for the pre-operative computation of optimized paths for the PBN.

1.1.4 Needle control and tracking

Precision is of paramount importance in needle insertion. The inability to accurately reach the target can undermine the therapy outcome or lead to an incorrect diagnosis while errors in following the planned path can drive the needle against delicate anatomical structures (e.g. blood vessels, brain ventricles) with risks for the patient.

Needle deployment can benefit from robotic-assisted insertion platforms combined with needle tracking solutions able to inform the control system about the current needle configuration in a closed-loop fashion (Cowan et al., 2011). Tracking solutions include standard imaging techniques such as X-ray fluoroscopy (Ralovich et al., 2014), ultrasound (Vrooijink, Abayazid, and Misra, 2013; Chatelain, Krupa, and Marchal, 2013) and electromagnetic trackers (Sadjadi, Hashtrudi-Zaad, and Fichtinger, 2012).

Specific control methods have been proposed for the PBN needle. A first closed-loop strategy was proposed in Secoli and Rodriguez Y Baena, 2013, later extended in Secoli and Baena, 2016 to counteract unmodelled steerability properties of the needle.

Some duty-cycling bevel-tip steerable needles rotate inside the tissue to correct the steering direction or, as the PBN, develop complex shapes on the tip to bend. In doing so, these needles determine frictional and shear forces on the tip or between the tissue and needle shaft (Reed, Okamura, and Cowan, 2009; Secoli and Baena, 2016) that determine a torsion of the needle resulting in a different rotation angle between the needle tip and the needle base. Torsion adds to the deflections normally evidenced in percutaneous needles due to the effect of tissue deformation and inhomogeneity (Misra et al., 2010). If not

properly addressed by the control system, torsion and deflections can drive the needle out of the planned insertion path and jeopardize the possibility to reach an accurate targeting. Unfortunately, neither imaging nor electromagnetic systems can track needle torsion as percutaneous needles are too thin for visualize a rotation about the needle insertion axis or to accommodate a 6 degrees of freedom sensor (Cowan et al., 2011). Some research groups have addressed the lack of one degree of freedom orientation information by assuming an infinite torsional stiffness of the needle (Vrooijink, Abayazid, and Misra, 2013; Shahriari et al., 2015; Abayazid, Kemp, and Misra, 2013; Abayazid et al., 2015; Patil et al., 2014). This assumption does not hold for many types of steerable needles and, while for some specific needle designs bespoke solutions have been proposed in the form of torsion model or state observers (Reed, Okamura, and Cowan, 2009; Kallem and Cowan, 2009), for the PBN torsion estimation represents still an open issue.

1.1.5 The PBN control framework

The different agents included in the PBN robot-assisted insertion framework are presented in Fig. 1.2.

In the pre-operative phase, imaging data are acquired and the patient anatomy is reconstructed through the segmentation of the relevant anatomical structures. The operator determines the planning query (i.e. the entry and target location) as well as the sensitive structures to avoid. Data are then provided to the path planner for the pre-operative plan computation.

In the intra-operative phase, the operator supervises the needle insertion and can adjust the insertion path. The control system drives the needle along the desired path and corrects for insertion errors on the basis of the PBN position and orientation information provided by the pose estimation module.

1.2 Aim of the thesis

The aim of this PhD thesis consists of developing a pre-operative curvilinear path planner for steerable needles and designing a solution for estimating the needle tip position and orientation (i.e. the full pose) during the insertion. The

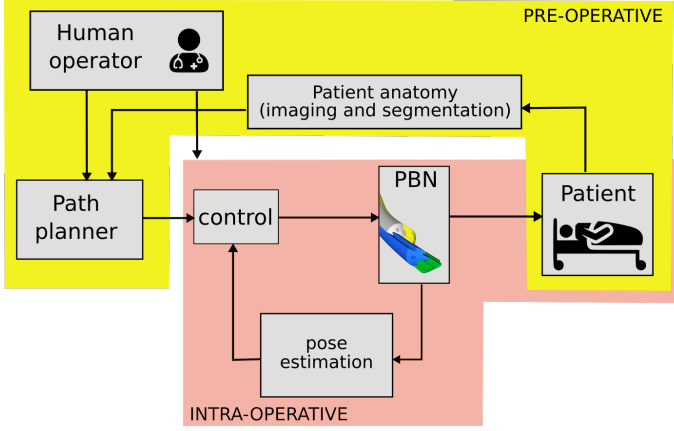


FIGURE 1.2: In the schematic, the different agents included in the robot-assisted PBN insertion framework are presented.

proposed methods consider the EDEN2020 PBN as a case study.

Starting from the open technical challenges, the research hypotheses that guide the PhD work can be summarized as follows:

1. **Hypothesis 1:** The curvilinear path planner can solve the planning query computing a kinematically feasible solution for the steerable needle.
 - (a) The path is computed in accordance with the optimization criteria of minimum path length and maximum obstacle clearance (**Hypothesis 1.1**)
 - (b) The computational time can be kept consistent with standard pre-operative planning algorithms (**Hypothesis 1.2**)
2. **Hypothesis 2:** the full pose of a multi-segment steerable needle can be estimated using position sensors mounted on the needle tip
 - (a) the full pose of a two-segment PBN can be estimated (**Hypothesis 2.1**)
 - (b) the full pose of a four-segment PBN can be estimated (**Hypothesis 2.2**)

To investigate the aforementioned hypotheses, specific research activities have been performed, which are thoroughly discussed in this PhD dissertation.

To properly contextualize the research topics expressed in **Hypothesis 1**, in Chapter 2 a literature survey was carried out by reviewing methods for steerable needles path planning. The survey focuses on sampling-based planning methods as the most popular and promising approaches.

In Chapter 3, **Hypothesis 1** is investigated and a new method for pre-operative path planning is presented using the PBN as a case study. **Hypothesis 1.1** is investigated by proposing a novel evolutionary path optimization solution while **Hypothesis 1.2** is addressed implementing a redefinition of the workspace considering needle kinematics to speed up the path computation. The method was validated against solutions from literature in simulated neurosurgical insertions.

Chapter 4 focuses on **Hypothesis 2**. A new method to estimate the pose of a multi-segment needle from data provided by position sensors is presented. The segment tips position are used as input for a kinematic-based prediction method. To answer to **Hypothesis 2.1** and **Hypothesis 2.2**, the solution was provided for both a two-segment and a four-segment PBN. Validation was performed through simulation trials and experiments in phantom-brain gelatin.

In Chapter 5, the conclusions, the scientific implications and the future perspective of this PhD work are reported and discussed.

Appendices are reported in Chapter 6.

A graphical abstract of this PhD thesis is shown in Fig. 1.3.

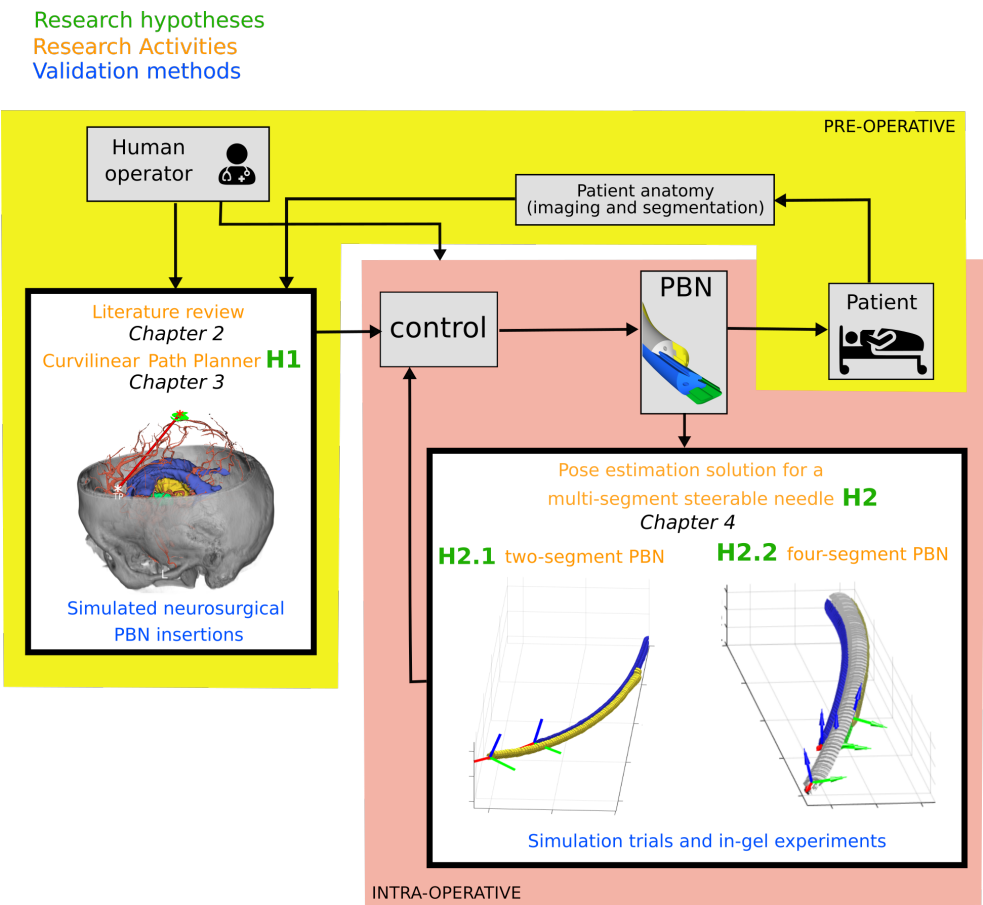


FIGURE 1.3: Graphical abstract of the PhD thesis. The research hypotheses that guide this PhD work are presented, along with the performed activities and the solutions employed to validate the proposed methods.

Chapter 2

Sampling-based path planning solutions for steerable needles in minimally invasive surgery: a survey

Automatic path planners are a fundamental tool in the task of finding feasible insertion pathways for steerable needles in minimally invasive surgery because of the complex needle kinematics. Many solutions were proposed in the literature on this topic and most of them rely on sampling-based approaches. In the present chapter, **Hypothesis 1** is contextualized by proposing a survey on the sampling-based planning algorithms presented in the literature in the last two decades. The reported methods are first subdivided into single and multi-query approaches and then reviewed in terms of the methodology used, their efficiency and how they are experimentally validated. The possibility to execute intra-operative replanning is also evaluated, along with their ability to address uncertainties in needle motion and in the environment.

2.1 Introduction

In current clinical practice, a growing number of minimally invasive procedures rely on the use of needles. Some examples are represented by biopsies, brachithrapy for radioactive seeds placement, abscess drainage and drug infusion. With respect to standard open surgeries, the small diameter of the

needles allows to reach the targeted anatomy with limited tissue damage, reducing the risks for the patient and speeding up the time for recovery.

Over the last two decades, different research groups have focused their efforts on the development on needles able to steer inside the tissue. These needles can perform curvilinear trajectories maximizing the distance from sensitive anatomical structures and reaching targets otherwise inaccessible via rectilinear insertion paths.

Different steerable needle designs and approaches have been proposed in the literature (Berg et al., 2015), including base manipulators (Glozman and Shoham, 2007), tissue manipulators (Torabi et al., 2009), bevel-tip needles (Webster et al., 2006; Engh et al., 2010; Watts, Secoli, and Baena, 2019), pre-curved stylet (Okazawa et al., 2005), concentric-tube needles (Gilbert, Rucker, and Webster, 2016), tendons actuated needles (Berg, Dankelman, and Dobbels, 2015), active cannulas (Zhao et al., 2016) and magnetically controlled needles (Petruska et al., 2016).

Differently from conventional straight needles, for which the insertion path can be planned and performed by the clinician on the basis of the target location and the patient anatomy, the complex kinematics of steerable needles make the path planning unbearable, requiring the aid of an automatic path planner. Automatic planners often require the definition of the starting and target point as inputs from the clinician, as well as the reconstruction the patient anatomy. Standard imaging modalities as X-ray fluoroscopy, ultrasound (US), computerized tomography (CT) or magnetic resonance imaging (MRI) can be used to this end. Intra-operative imaging information can be used as a feedback to correct possible insertion errors arising from tissue inhomogeneity, obstacles and target movements and errors in needle motion modelling. Sampling-based planning is a type of path planner that produce a path by sequentially sampling different points in the robot's workspace and gradually constructing a data structure that represents collision-free paths. It features probabilistic completeness, i.e. if a solution to the path planning problem exists, it will eventually find it. Sampling-based solutions are successfully used in a wide range of problems, including the determination of a suitable path for steerable needles.

To properly contextualize **Hypothesis 1**, in this chapter we propose a survey

on the principal sampling-based algorithms proposed in the literature over the last two decades for steerable needle path planning. In this review, the focus will be on the sampling-based method at the base of the proposed solutions, which can be either a single-query and multi-query approach, as from the classification proposed by Kavraki and LaValle, 2016. The methods herein reported can be further divided in classes depending on the planning algorithm they use. An overview of these planning approaches is reported in Fig. 4.2.

The possibility for the methods to recompute the path intraoperatively will be highlighted as well as the capability to address specific planning problems such as uncertainties in the needle motion model or linked to unpredictable obstacle or target movements. The approaches used by the authors to verify the performance of the proposed solutions are also presented.

In Section 2.2, relevant concepts of the path planning problem are described. In Section 2.3 and Section 2.4, single-query and multi-query planning solutions are presented, respectively. Conclusions are presented in Section 2.5.

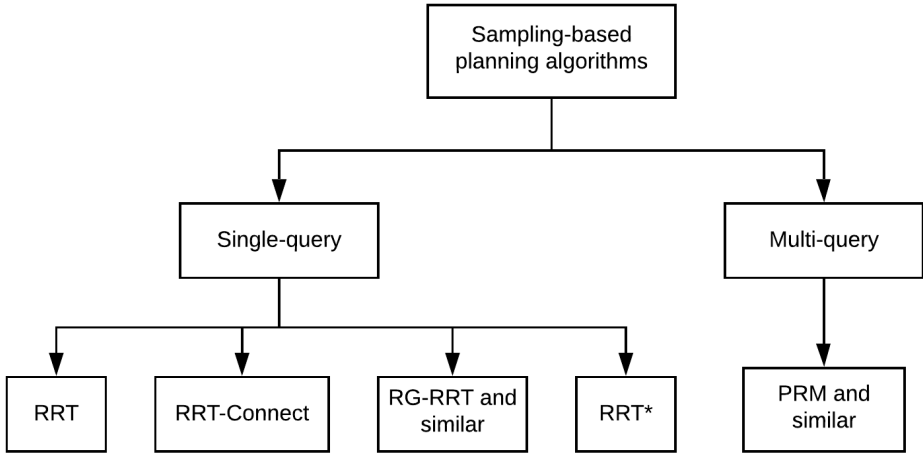


FIGURE 2.1: Schematic representation of the sampling-based planning methods.

2.2 Problem formulation

We define the path planning problem as in Kavraki and LaValle, 2016; Karaman and Frazzoli, 2011.

The workspace $\mathcal{W} = \mathbb{R}^N$ (with $N = 2$ or $N = 3$) represents the environment where the robot \mathcal{R} can move. We define $\mathcal{O} \subset \mathcal{W}$ the part of the workspace occupied by obstacles. The configuration space, or C-space, is the space of all possible robot configurations defined considered the robot kinematics. With $\mathcal{R}(\mathbf{q}) \subset \mathcal{W}$ we refer to the points in the workspace occupied by the robot in the specific configuration \mathbf{q} . The part of the configuration space occupied by the obstacles can be defined as:

$$\mathcal{C}_{obs} = \{\mathbf{q} \in \mathcal{C} | \mathcal{R}(\mathbf{q}) \cap \mathcal{O} \neq \emptyset\}$$

and the set of configurations that avoid obstacle collision is $\mathcal{C}_{free} = \mathcal{C} \setminus \mathcal{C}_{obs}$.

Definition 1: Path planning

Given a starting and goal configuration $\mathbf{q}_I, \mathbf{q}_G \in \mathcal{C}_{free}$ (i.e. a *query*), the path planning problem consists in computing a continuous path $\tau : [0, 1] \rightarrow \mathcal{C}_{free}$ in a way that $\tau(0) = \mathbf{q}_I$ and $\tau(1) = \mathbf{q}_G$.

Path planning and trajectory planning are two separate concepts. The first one concerns the computation of a continuous curve in the configuration space from \mathbf{q}_I to \mathbf{q}_G while trajectory planning refers to the problem of taking the result of the path planning algorithm and define how to move along this path in terms of velocities and accelerations. A trajectory is thus a set of states associated with time (Yang et al., 2016).

In the present chapter, the problem of trajectory planning is not covered.

Definition 2: Optimal path planning

Given a planning query and a cost function $c : \Sigma \rightarrow \mathbb{R}_{\geq 0}$, where Σ represents the set of all paths, the optimal path planner is the one able to compute a feasible path τ^* such that $c(\tau^*) = \min\{c(\tau) : \tau \text{ is feasible}\}$. If no such path exists, it reports a failure.

Path planning in minimally invasive surgery

Path planning in minimally invasive surgery has to meet multiple requirements at the same time in order to achieve the proper level of safety and efficacy. These requirements can be the needle technical specifications or the translation of clinical aspects into specific constraints.

Conceptually, the requirements can be divided in *strict* and *soft* constraints (Es-sert et al., 2012). Strict constraints are conditions that must be satisfied (e.g., the needle should not intersect any obstacle, or the path curvature should not exceed the maximum degree of curvature admissible by the needle) and define the available workspace for the path planning algorithms, limiting the path search to regions where solutions can lie, excluding the unfeasible ones. Soft constraints, instead, can be considered as the objectives of the optimization and are included in the cost function to drive the path search toward the best solution. The cost function to be minimized generally takes the following form:

$$F(x) = \sum_{i=1}^N k_i * f_i(x)$$

with f_i representing a specific soft constraint opportunely weighted by a factor k_i , which is often chosen empirically through multiple experiments or on the basis of the clinicians' suggestions.

Different planners include different objectives but, generally, one or more of the following are included:

- minimization of the path length
- maximization of the distance from one or multiple anatomical obstacles
- maximization of the probability to reach the target

Sometimes, the minimization of the path curvature is also considered, together with the reduction of its standard deviation in order to provide a smoother path and reduce the effort required to control the needle insertion.

The different objectives considered by the works reported in this survey will be mentioned.

2.3 Single-query planners

Single-query planners start from a query composed by the start and goal configurations and perform an incremental search. They randomly sample the robot configuration space to incrementally develop a tree data structure (Kavraki and LaValle, 2016). The planners herein proposed exploit the Rapidly-exploring Random Tree (RRT) structure (LaValle, 1998) or its derivatives.

2.3.1 Solutions based on RRT

The first implementation of an RRT path planner for steerable needles in 3D with obstacles was proposed by Jijie et al., 2008 for a bevel-tip needle. The planner randomly samples the space of control inputs obtaining a trade-off between exploration complexity and completeness. The method is tested also to define, given the target point, a feasible entry point for the needle within a user-defined entry area, starting the search from the target rather than from the start point in a backchaining fashion. The solution was tested in a simulated undeformable environment with ideal spherical obstacles.

Patil, Van Den Berg, and Alterovitz, 2012 proposed a solution for bevel-tip needles in 2D deformable environments by accounting for uncertainty in deformation model, noisy sensing data and unpredictable actuation. Firstly, an RRT algorithm is used to generate a set of candidate motion plans, then the plan with the highest estimated probability to successfully avoid obstacles and reaching the goal region is selected. This method was verified in 2D simulations, demonstrating a computational time in the order of minutes.

In the work of Seiler et al., 2012, a path correction algorithm is integrated into an RRT planner for bevel-tip needles in 3D static environments. A fast path correction is executed while preserving the characteristic of the initial trajectory and eliminating the need for expensive replanning from scratch. Motion uncertainties are considered while environment deformations are not covered. Sun, Patil, and Alterovitz, 2015 proposed a high-frequency planner based on multiple independent RRTs executed in parallel at every insertion step from the current needle tip position to the target point. This allows to compute, at every time step, a motion plan that asymptotically approaches the global

optimum. At each iteration step, the best plan is estimated according to two optimization objectives: the probability to successfully reach the target without colliding with obstacles and the minimization of the path length. This plan is adjusted considering sensory information and a liner feedback control. Uncertainty deriving from errors in needle kinematics, sensing noise and obstacles motion are propagated over the next insertion steps to obtain an estimation of the path uncertainty from the start to the goal position. The feasibility of the proposed solution was tested in simulation in a liver biopsy scenario, where the vasculature represents the sensitive anatomical obstacle, using a duty-cycle bevel-tip needle as a case study.

Parallel path computation is used also in the Adaptive Fractal Trees (AFT) proposed by Liu et al., 2016 for a Programmable Bevel-tip steerable Needle (PBN). This method takes advantage of the fractal theory and the architecture of graphics processing units (GPUs) to parallelize the planning process and enhance the computation performance to achieve online replanning, as demonstrated in simulated 3D liver needle insertions. AFT are the basis for the Adaptive Hermite Fractal Tree (AHFT) proposed by Pinzi, Galvan, and Rodriguez y Baena, 2019 where the fractal structure was combined with optimized geometric Hermite curves to perform a path computation accounting for the target heading (i.e. the orientation) at both the start and the target points. Although developed and tested only for a preoperative neurosurgical scenario, AHFT is suitable for GPU parallelization for a rapid intraoperative replanning.

RRT-based planners were also used in the context of design-optimization for concentric-tube needles. These needles can feature different 3D curves depending on the lengths, degree of curvature, number and stiffness of the tubes. Baykal, Bowen, and Alterovitz, 2019 developed a design optimization method to estimate design parameters the allows the concentric tube robot to reach as many desirable target regions as possible guaranteeing the obstacle clearance. In their work, they used a global optimization algorithm for the evaluation of different robot designs. Subsequently, performance were verified in the configuration space through an RRT-based motion planner to estimate the percentage of workspace the needle design is able to cover.

2.3.2 Solutions based on RRT-Connect

The RRT-Connect (Kuffner and La Valle, 2000a) is a structure that incrementally expands two RRTs rooted at the start and the target configurations. These two RRTs explore the space advancing towards each other with a simple greedy heuristic until they connect. Fauser, Sakas, and Mukhopadhyay, 2018 proposed two methods accounting for needle tip position and orientation using the RRT-Connect. The first method corresponds to an extension of Patil et al., 2014 into RRT-Connect, where the requirement of matching the initial and target needle pose is solved as a Dubins path problem. The second method uses cubic Bezier-spline to interpolate in $SE(3)$ achieving a second order trajectory differentiability. From simulated insertions performed using real patients dataset and synthetic anatomies mimicking a temporal bone surgery scenarios, the clear superiority of a specific algorithm was not evidenced even though a larger anatomical clearance was shown for the solution based on Bezier-spline at the expense of a lower number of estimated feasible paths. This solution was also tested in other kinds of surgical interventions (Fauser, Sakas, and Mukhopadhyay, 2018).

Later, it was included in a automatic preoperative pipeline for anatomical structures segmentation and path planning and tested in simulated cochlear implantation and vestibular schwannoma removal (Fauser et al., 2019b). More recently, a further extension was proposed by translating the Bezier curves into circular arcs (Fauser et al., 2019a) resulting in a further increase in the distance from obstacles in simulated temporal bone surgery and intraluminal catheter insertion scenarios.

2.3.3 Solutions based on RG-RRT and similar

Patil et al., 2014 proposed a solution for duty-cycling steerable needles able to plan and control the needle motion in a closed loop fashion guaranteeing obstacles avoidance and uncertainties compensation. Confining the search on the subset of point in the workspace that meets the kinematic constraints of the needle, this solution allows a path replanning suitable for online procedures and ensures clinically acceptable error of less than 3 mm, assessed though

experiments ex-vivo and in tissue samples. In this work, the RG-RRT was used as planning method (Patil and Alterovitz, 2010). RG-RRT are a combination of RRT and a reachability-guided sampling heuristic that constructs the path through a sequential connection of arcs with variable curvature bounded within the maximum curvature achievable by the needle. A bespoke distance metrics overlooks points of the configuration space that are not reachable from a given state. Patil and Alterovitz, 2010 express the planning objective in terms of minimizing the insertion length and maximizing the clearance from obstacles.

RG-RRT was also at the base of the work of Vrooijink et al., 2014, where the planner proposed by Patil and Alterovitz, 2010 was embedded in a needle steering system and tested in a soft-tissue phantom. Needle tip tracking was obtained through the use of US imaging so that the planner could intraoperatively re-plan the needle insertion path in a closed-loop manner to address uncertainties in steering and perturbation in obstacles and target locations. A 2D implementation of the RG-RRT was proposed by Caborni et al., 2012 for applications in the neurosurgical field.

The idea of connecting arcs with bounded curvature is at the base of the geometric-based arc planner (Arc-RRT) proposed by Bernardes et al., 2011 for 2D intraoperative path planning, with a method that demonstrated robustness in coping with modelling uncertainties, tissue deformation and inhomogeneity. This method, originally tested only in simulation, was later included in a robotically assisted system for 2D needle steering combined with image feedback and tested through experiments in a gelatine phantom (Bernardes et al., 2012). Performance has been later enhanced (Bernardes et al., 2013) by implementing an Arc-RRT with sampling performed in the control inputs rather than in the configuration space.

Zhao et al., 2015 proposed a fast computation of RG-RRT that features a greedy heuristic strategy based on the Depth First Search. This search approach stresses the search toward the target encouraging a connection through linear path where possible rather than via arcs with a bounded curvature. The best solution is determined on the basis of a cost function that fosters, in addition to

the paths length and the distance from obstacles, also both a reduced magnitude and a limited variation of the path curvature. This solution was later extended in a dynamic motion planner that addresses the uncertainty related to the movement of the obstacles and the target (Zhao et al., 2016). This method was developed for a novel flexible tool composed by a bevel-tip needle inserted into a flexible cannula. This design allows the needle to freely rotate without the effect of torsional friction between the needle shaft and the tissue and thus fostering a more precise control of the needle tip orientation. The planner includes solutions for ensuring planning convergence and solving for the large path detour problem that may arise in the presence of an unpredicted motion of the target and/or the obstacles. When tested in a simulated scenario with ideal spherical obstacles, the method resulted to be robust and suitable for real-time replanning.

Kuntz et al., 2015 developed a hybrid approach to plan the motion of a multi-lumen transoral lung access system designed to perform biopsies in the lung. The system is composed of three serial stages: a bronchoscope to access the bronchial tubes, a concentric tube to enter the lung parenchyma and a bevel-tip needle to steer in the parenchyma and reach the nodule avoiding lung vessels. The motion plan consists of a sequence of collision-free configuration of the multi-lumen system and associated control inputs. An initial sampling-based approach defines the path of the first stage as a sequence of piece-wise linear curves. The second stage is then actuated and a mechanic-based kinematic model (Rucker, 2011) is used to infer the tip position and the orientation of the concentric tube robot when it touches the parenchyma. Then the third stage follows the path in the parenchyma estimated through the RRT approach proposed by Patil et al., 2014. The system was tested in a simulated lung biopsy scenario. The method has been successively extended by Fu et al., 2018: from lung CT data, a cost map was introduced encoding the costs associated with traversing the specific voxel determined as the probability for the voxel to be part of the lung vessel tree. Over time, the planner estimates more paths and minimizes the accumulated cost.

2.3.4 Solutions based on RRT*

The RRT* (Karaman et al., 2011) represents an “anytime” variation of the original RRT: it quickly identifies an initial feasible plan and then, as the plan execution process, it improves the plan toward an optimal solution. This is achieved by rewiring the RRT removing redundant edges and keeping the shortest or the minimum-cost path. As with RRT, an initial feasible solution is found quickly but, in addition, RRT* almost surely converges to an optimal solution.

Hong et al., 2019 proposed an RRT*-based path planner for a magnetically guided flexible needle for Deep Brain Stimulation (DBS) (Petruska et al., 2016) minimizing the insertion length and maximizing the obstacle clearance.

Favaro et al., 2018b proposed a solution based on an RRT* approach that runs within a dynamic subset of the original configuration space. This subset is shaped as an ellipsoidal volume, heuristically defined so that to change according to the planning phase in view of confining the search only where better solutions can lie. This approach reduces the RRT* complexity and the computational time. Path length, curvature and obstacle clearance are optimized according to a cost function while control errors are included in the planning phase by increasing the path uncertainty over the insertion length. Simulated insertions were performed to test the method in complex DBS scenarios (Segato et al., 2019; Favaro et al., 2018a).

An evolution of Favaro et al., 2018b is reported in Chapter 3 of this PhD dissertation. The method, tested in simulated neurosurgical intervention scenarios, relies on a new heuristic which limits the search space to a subset of reachable needle configuration considering the maximum degree of curvature of the needle. In addition, path planning benefits from a novel optimization procedure intended to correct the final needle path minimizing the path length, the magnitude and the variability of the path curvature while keeping the obstacle avoidance as large as possible.

Bergeles and Dupont, 2013 proposed a path planning algorithm based on RRT* and suited for a concentric tube robots with applications in neurosurgery. The planner solves for a sequence of stable configurations to move the needle from the start to the target configuration and avoid anatomical obstacles.

2.4 Multi-query planners

Multi-query planners are intended for those conditions where it is required to perform different planning queries in the same static environment. In this case, the algorithm invests computational time in pre-processing the configuration space so that future queries can be answered efficiently. To this end, a topological graph that captures the connectivity between different configuration samples is build, taking the name of roadmap. Once the roadmap is computed, paths can be easily computed by searching the graph through a proper node-based search algorithm (e.g. Dijkstra). The general framework consists in a sampling-based roadmap and was proposed by Kavraki et al., 1996 under the name of probabilistic roadmaps (PRMs) .

Alterovitz, Siméon, and Goldberg, 2008 proposed a 2D motion planning framework for a bevel-tip needle that addresses the uncertainty in the needle motion. This is performed by considering a stochastic motion model of the needle, which represents the probability to move from one state to another as the result of a specific control action. A Stochastic Motion Roadmap (SMR) is defined by initially sampling the configuration states in a random manner to build a collision-free connectivity map. Then, for each sampled state i , the planner computes the optimal action to be performed to maximize the probability of reaching the target being i the current needle state. This represents a Markov Decision Process and it is solved using infinite horizon dynamic programming (Smith, 1996). A sequence of optimal control actions that maximize the probability to reach the target without colliding with obstacles is computed. The same SMR planned pre-operatively is used intraoperatively for fast path re-computation. This approach tends to foster lengthy but safer insertion paths. The method, originally tested in randomized simulations, was later tested in combination with an integrated needle-steering system composed by a needle pose estimator, a torsion compensator and a planar controller (to guarantee the needle to move on the ideal insertion plane) and evaluated in a brachitherapy scenarios with artificial and ex-vivo tissues (Reed et al., 2008; Reed et al., 2011).

A Rapidly-Exploring Roadmap (RRM) was firstly proposed by Alterovitz, Patil, and Derbakova, 2011 and consists in an optimal motion planning that

perform a trade-off between random-sampling exploration of the configuration space and refinement of the existing path according to a user-specified parameter. It guarantees probabilistic completeness and asymptotic convergence to the optimal solution sparing computational time by focusing the refinement procedure only on paths that can reach the target configuration. Torres and Alterovitz, 2011 developed a preoperative motion planner built on an accurate kinematic model and an RRM for a concentric tube needle able to cope with needle actuation uncertainties. A directed graph is defined, having different needle configurations as vertices and edges weighted according to the cost linked to moving from one configuration to another. The path with lower cost is selected over the RRM using the Dijkstra algorithm. An extension of the presented method was reported in Torres, Baykal, and Alterovitz, 2014 where the motion planner for concentric tubes achieved an interactive rate. In this work a roadmap is computed pre-operatively using a variant of rapidly exploring random graph (RRG). Once computed, the roadmap is quickly explored through the A* search algorithm (Hart et al., 1968) to look for the shorter motion plan in the roadmap any time the user defines a new planning query. This planner, initially tested in simulation, was later implemented in a tele-operated control framework in an environment with tubular obstacles, achieving promising accuracy and an interactive execution speed. Lobaton et al., 2011 developed an approach for optimal, collision-free path planning to visit multiple goals in any order. The method builds a roadmap by sampling circles of constant curvature and generates feasible transition between circles. The multiple goals objective takes the shape of a multi-query planning problem, solved by the algorithm using a minimum directed Steiner tree on the roadmap. The optimal path can visit all the target locations while minimizing the extent of tissue cut, i.e. the path length. Simulations are performed in 2D and 3D static environments ignoring possible tissue deformations.

A PRM is at the base of the works of Leibrandt *et al.* (Leibrandt, Bergeles, and Yang, 2016; Leibrandt, Bergeles, and Yang, 2017), where it is used to define active constraints for the definition of stable needle configurations to reach the desired target. The PRM is computed off-line exploiting a parallel computer architecture and it can be queried on-line whenever it is required to find the

shortest path between the current and the target configuration.

Sudhakara, Ganapathy, and Sundaran, 2018 enhanced the classical PRM method using shape preserving Piece-wise Cubic Hermite Interpolation technique to generate smooth trajectories in 2D considering direction constraints on both the start and the target positions. Simulation experiments were carried out in a 2D environment with static geometrical obstacles.

Since PRM does not show a great performance in dynamic environments, a combination of PRM and Reinforcement Learning was proposed by Baek et al., 2018 for path planning in laparoscopic robotic surgeries. The method was tested in a simulated laparoscopic surgery robotic system under the assumptions that the tissue moves constantly and the path is performed in 2D.

2.5 Conclusions

The complex kinematics of steerable needles require automatic solutions for the path planning task. Planners are asked to find feasible paths solving a multi-objective planning problem that requires to meet specific criteria such as the maximization of the distance from anatomical obstacles and the minimization of the path length. Many solution have been proposed in the literature, a great number of them rely on sampling-based approaches to find the optimal path. In this chapter, we propose a survey of the sampling-based path planning algorithms reported in the literature in the past two decades with the aim of laying the foundation for addressing **Hypothesis 1**.

The methods herein reported are divided in single-query or multi-query solutions depending on whether the computation they perform on the workspace can be reused to solve multiple path planning queries. Solutions are analyzed in terms of the methodology used, their efficiency as well as the possibility to perform intra-operative replanning and deal with uncertainties in needle motion and/or in the environment. The approaches used by the authors to validate their solutions are also reported.

The great possibilities associated with steerable needles in terms of therapy outcome and patient safety make path planning a topic of great interest for

researches and engineers. Many solutions have been proposed to cope with this task, including but not limited to the sampling-based solution reported in this chapter.

A relevant aspect evidenced in several of the works herein reported consists in the uncertainty associated to needle motion and tissue deformation that can arise during needle deployment and jeopardise the insertion accuracy. Despite the remarkable performance and the level of readiness reached in simulations by many solutions reported in this survey, what is often missing is a thorough evaluation of the planning performance in conditions that mimic a real needle insertion through e.g., in-gel or ex-vivo experiments. This would make possible to assess the feasibility of the proposed algorithm in presence of tissue and modelling uncertainties which represents, in our opinion, one of the big open questions in steerable needle path planning.

Recently, big efforts have been made to explore new optimization strategies and methods, e.g. the use of Reinforcement Learning, but the high complexity of needle kinematics combined with the uncertainties and the dynamic nature of the environment in which they operate lead path planning open to further relevant improvements.

Chapter 3

An evolutionary-optimized surgical path planner for a programmable bevel-tip needle

Path planning algorithms for steerable needles in medical applications must guarantee anatomical obstacle avoidance, reduce the insertion length and ensure the compliance with the needle kinematics. The majority of the solutions from the literature focus either on fast computation or path optimality, the former at the expense of sub-optimal paths, the latter by making unbearable the computation in case of high dimensional workspace.

In this chapter we investigate **Hypothesis 1**. We implemented a 3D pre-operative path planner for steerable needles for neurosurgical applications which keeps the computational cost consistent with standard pre-operative planning algorithms guaranteeing the kinematic feasibility and the quasi-optimality of the estimated pathways.

From a user-defined entry point, our method confines a sampling-based path search within a subsection of the original workspace considering the curvature admitted by the needle. **Hypothesis 1.1** has been addressed by developing an evolutionary optimization procedure to maximize the obstacle avoidance and reduce the insertion length. The pool of optimized solutions is examined through a cost function to determine the best path.

Simulations on one dataset showed the ability of the planner to compute the path within a computational time consistent with pre-operative planning (**Hypothesis 1.2**) by exploiting the smart redefinition of the search space. The method

proved to overcome the state of the art in terms of obstacle avoidance, insertion length and probability of failure, proving this algorithm as a valid planning method for complex environments.

The application of the method resulted in a journal paper ¹ currently under review

3.1 Introduction

Flexible, small-scale catheters allow reaching deep regions inside the human body. Continuous robots represent a category of robotic tools that provides the required level of dexterity and reliability to perform delicate surgical procedures (Burgner-Kahrs, Rucker, and Choset, 2015). As they are flexible and can be built in small-scale, they can be useful in neurosurgery for situations where the access to anatomical structures is particularly challenging due to a cluttered anatomical workspace.

The steering of a flexible robotic probe is achieved using a bevel-tip needle with a fixed shape which rotates according to a duty-cycle that determines the bending of the needle toward the desired direction (Engh et al., 2010; Kallem and Cowan, 2009; Reed et al., 2011). Glozman and Shoham, 2007 used an external base to which the needle is anchored to drive the insertion and to follow a desired trajectory. Pre-bent concentric elastic tubes use an axial rotation and translation at the base to make the entire needle shape varies through the interaction between the elastic tubes (Rucker, Jones, and Webster, 2010). A bio-inspired, multi-segment programmable bevel-tip needle (PBN) is currently under development as core technology of the EDEN2020 project (Secoli and Baena, 2016). PBN consists of a continuous robot manufactured with four axially-interlocked sections. These segments are robotically actuated at the base so that, sliding over each other, they can generate an offset on the needle tip and determine a curvature in the 3D space. The kinematics of the probe is still under investigation but a PBN control strategy is proposed in Secoli, Rodriguez, and Baena, 2018.

The benefits in maneuverability exhibited by flexible manipulators give rise to

¹A. Favaro, A. Segato, F. Muretti and E. De Momi, "An evolutionary-optimized surgical path planner for a programmable bevel-tip needle", *IEEE Transaction on Robotics (TRO)*, under review

an increased number of possible needle pathways that can be correctly handled only by an automatic planner. Such a planner can be designed to tune the pathway according to specific optimality criteria. Essert et al., 2012 and Patil et al., 2014 formalized the implicit and explicit principles used by neurosurgeons for the definition of optimal trajectories. The minimization of the surgical path length and the maximization of the clearance from anatomical obstacles can be considered as general axioms aiming at limiting the tissue damage while providing a proper safety margin in case deviations from the planned path occur.

In our previous work (Favaro et al., 2018b), we presented a neurosurgical planner for PBN. The algorithm solves a single-query planning task, i.e. it connects an entry point to a target, guaranteeing the clearance from anatomical obstacles and complying with PBN's kinematic limits.

The present work aims at addressing **Hypothesis1** by describing a novel approach that improves the performance of our previous method on different aspects. Tailored to the PBN, the algorithm focuses the search using a smart redefinition of the search space so that the desired target point can be reached guaranteeing the compliance with the maximum degree of curvature admitted by the needle. This approach permits to save time by examining only the part of the workspace which will end up in providing feasible solutions, reducing the computational cost correlated to this initial search phase and, in this, addressing **Hypothesis 1.2**. **Hypothesis 1.1** is investigated by proposing a method that uses an innovative evolutionary procedure to optimize the path. Optimality criteria provide for the path length minimization, the reduction of the magnitude and the variability of the path curvature and the maximization of the obstacle avoidance. A cost function fed to these parameters is designed to provide an overall optimality index for each solution and ultimately to define the best one.

The chapter is structured as follows. In Section 3.2, an overview of the path planning approaches proposed in the literature is presented. Section 4.2 outlines our planning method, with a focus on the redefinition of the search space and on the evolutionary optimization. Section 3.4 describes the experimental protocol. Section 4.4 presents the comparison between the presented solution and other methods from literature. Discussion and conclusions are reported

in Section 4.5 and Section 5, respectively.

3.2 Related works

In the context of path planning, a variety of approaches has been proposed in the literature.

In Schulman et al., 2014, the non-convex path optimization problem is subdivided in convex sub-problems, solved via sequential convex optimization. The method is feasible for underactuated non-holonomic systems as flexible medical needles. Although the method does not guarantee to find a solution if it exists, it can provide optimal locally collision-free paths.

Duindam et al., 2010 proposed a solution for estimating catheter pathways totally described in geometric terms and inspired by the Paden-Kahan sub-problem, an explicit solution to inverse kinematics used as alternative to the implicit expression provided by the Denavit-Hartenberg parameters. The method was tested in a simplified environment and showed a high speed in the path computation with limited obstacle avoidance capabilities.

Potential field methods, based on the idea originally introduced by Khatib, 1986, compute a potential field similar to the one generated by electrical charges. The potential field results by the interaction between the attractive effect of the target contrasted by the repulsive action of the obstacles. This approach has the drawback of generating local minima. To address this problem, Li et al., 2014 proposed an artificial potential field method where a conjugate gradient algorithm was exploited and suggested an application of their solution for brachytherapy. The clearance from anatomical obstacles was achieved but the method, as such, does not comply with other requirements as the optimization of the total path length or the catheter kinematics.

Other approaches fall back into two main categories:

3.2.1 Graph-based methods

Graph-search methods are based on the discrete approximation of the planning problem. They are “resolution complete” as they can determine in a finite time whether a solution exists, and “resolution optimal” since they can

estimate the best path given a specific resolution.

Likhachev et al., 2005 proposed the incremental A* solution for 2D applications, which extended the original A* planning method so that to reuse previous information and drive the path towards optimality.

These methodologies show high computational time as the discretization of the environment becomes finer. For this reason, they are not suitable for neurosurgical applications as high-resolution 3D datasets are normally used (order of magnitude: $\sim 10^7$ points).

Leibrandt, Bergeles, and Yang, 2017 presented a multi-node computational framework for fast path planning for concentric tube robots. The method builds an undirected graph of possible transition of needle configurations and queries the graph using A* search to extract the shortest path between the current and the desired tip pose. To address the high computational effort required by the graph search and achieve interactive rates, a parallel computation is used and the search is confined in a subset of needle configurations close to the current one.

3.2.2 Sampling-based methods

Sampling-based methods are built on the random sampling of the workspace. Rapidly-exploring Random Trees (RRT) and RRT-Connect (Kuffner and La Valle, 2000b) are able to cope better with dense workspace than graph-based approaches. RRT* (Karaman and Frazzoli, 2011) and bidirectional-RRT (Jordan and Perez, 2013), are "probabilistically complete": as the number of samples tends to infinity the probability of finding a solution, provided that it exists, tends to one. Moreover, they are also "asymptotically optimal" as they can refine the initially-estimated raw path when new points are sampled and compute the shortest pathway to connect the start and target point as the number of iterations tends to infinity. These sampling-based methods have been widely used for steerable needles path planning, an overview of which is reported in Chapter 2.

A combination of RRT and a reachability-guided sampling heuristic (RG-RRT) was used in the work of Patil and Alterovitz, 2010 to compute motion plans

for steerable needles in complex 3D environments by constructing the tree via a sequential connection of arcs with bounded curvature. These solutions can be used in real-time applications, but performance have been assessed only in simplified workspaces. A neurosurgical 2D implementation of RG-RRT was proposed by Caborni et al., 2012.

Patil et al., 2014 proposed a solution for duty-cycling steerable needles able to plan and control the needle motion in a closed loop fashion, guaranteeing obstacles avoidance and uncertainties compensation. Confining the search on the subset of point in the workspace that meet the kinematic constraints of the needle, this solution allows a path replanning suitable for online procedures ensuring clinically acceptable error.

The planning approach proposed by Patil et al., 2014 has been used also by Kuntz et al., 2015 for motion planning of a multi-lumen system for lung biopsy. The system consisted in a concentric tube robot with a beveled tip steerable needle. Simulations demonstrated the ability to quickly computes plans with high clearance from obstacles.

Gammell, Srinivasa, and Barfoot, 2015 proposed the Batch Informed Tree (BIT*) algorithm. BIT* confines the search within an ellipsoidal region whose size relates to the cost of the current solution in a way that, any time a shorter path is found, the search occurs within a subspace progressively smaller in size. In our previous work (Favaro et al., 2018b), a similar approach has been implemented for the developing of a steerable needles path planner where the cost used to shape the search region is a function only of the length of the current best path and includes parts of the workspace that cannot be reached by the catheter due to its kinematic limits. Additionally, the path optimization was hindered by the intrinsically limited flexibility of cardinal splines used in the work for the path interpolation.

In the present work, we propose a new path planning solution where the heuristic path search is confined within the region of the workspace that can actually be reached by the needle, exploiting the capability of sampling-based planner in dealing with dense workspace. This prevent the planner to sample the workspace where no feasible solutions can be found, reducing the computational cost. Additionally, an innovative evolutionary procedure based on a

different path interpolation method and supported by a bespoke cost function is proposed to optimize the path in terms of path length, distance from relevant anatomical structures and path curvature.

3.3 Methods

Our 3D path planner method consists of three main steps: Path planning (Section 3.3.2, where a set of piece-wise linear paths is computed for the planning query), Path approximation and optimization (Section 3.3.3, where an evolutionary optimization procedure generates smooth paths, reduces their length and maximizes the obstacle avoidance) and Exhaustive search for the best path (Section 3.3.4, where an exhaustive search is performed over the set of paths for determining the best planning solution). The workflow of our solution is reported in Fig. 3.1.

3.3.1 Surgeon's input and patient's data elaboration

In this section, the user input and how it is interpreted as input to the algorithm is described.

As first step, the surgeon is asked to select the desired target point (TP) within the brain and the entry point (EP_0) on the cortex. The system delineates an entry area (a) around the EP_0 excluding the sulci due to the presence of blood vessels, as in De Momi et al., 2014. A mesh decimation is performed over a and a pool of feasible entry points $EP_{i,a}$, $i \in 1, \dots, N_a$ is defined, as in Favaro et al., 2018a. The total number of entry points (N_a) depends upon the radius of the entry area and the decimation level.

The anatomical obstacles are segmented in the patient image dataset and a distance map is computed Danielsson, 1980.

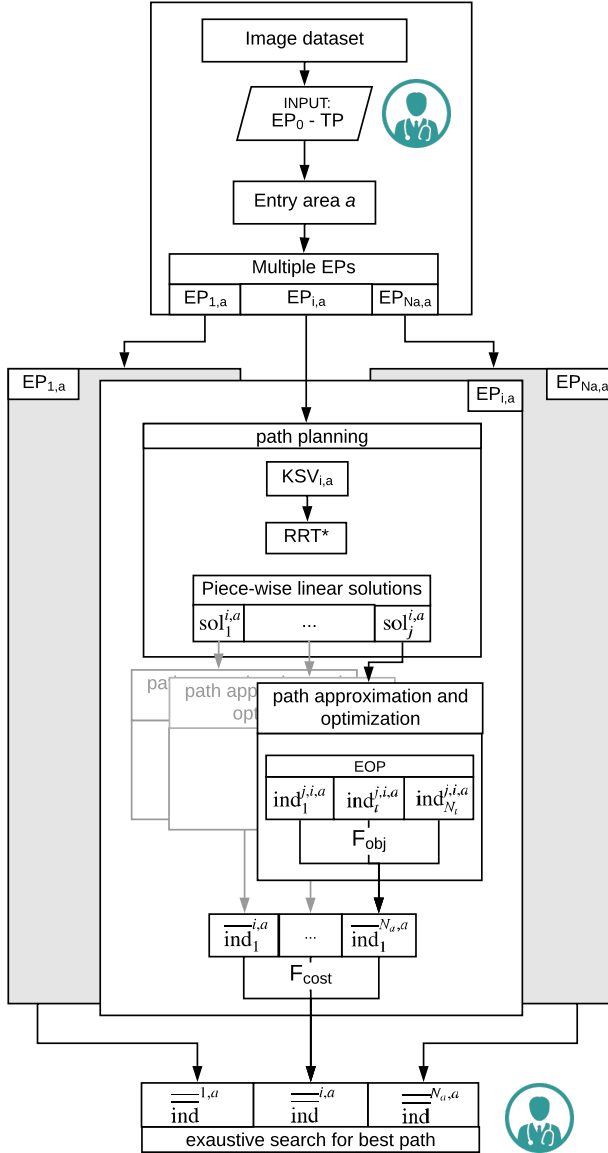


FIGURE 3.1: Schematic representation of the workflow. The surgeon is asked to define the entry (EP_0) and the target point (TP) on the patient dataset. The Entry Area (a) is then computed and the set of possible entry points $EP_{i,a}$, $i \in 1, \dots, N_a$ is defined. Subsequently, for each $EP_{i,a}$, the algorithm performs the path planning (Section 3.3.2) and the Evolutionary Optimization Procedure (Section 3.3.3). A number of feasible solutions $\overline{\text{ind}}_j^{i,a}$ are generated. For each $EP_{i,a}$, the best path $\overline{\text{ind}}^{i,a}$ is computed and eventually provided to the surgeon by running a cost function over the set of solutions generated by the EOP (Section 3.3.4).

3.3.2 Path planning

In the following, we describe our approach of minimizing the search space for achieve fast path planning. Geometrical properties derived from needle kinematics are considered to design the search space.

The original workspace consists of the volume represented by the patient's brain. In order to obtain a uniformly-distributed set of 3D points, this volume is intersected with an evenly-spaced grid featuring a distance between adjacent points equal to 1.3 mm^3 , empirically defined.

For each $\text{EP}_{i,a}$, $i \in 1, \dots, N_a$, a Kinematics Search Volume ($\text{KSV}_{i,a} \in \mathbb{R}^3$) is defined, representing the "smart redefinition of the search space" for path planning. A schematic 2D description of the proposed approach is reported in Fig. 3.2.

The reason for defining the $\text{KSV}_{i,a}$ is to identify a 3D space ("feasible space" in Fig. 3.2) where, considering the maximum curvature of the PBN (k_{PBN}), its tip can be oriented at any $\theta \in [-\frac{\pi}{2}, \frac{\pi}{2}]$ without preventing the possibility for the needle tip to reach the TP. The remaining workspace, referred as "unfeasible space", would imply a curvature greater than k_{PBN} to connect the $\text{EP}_{i,a}$ to the TP. Case when $\theta \notin [-\frac{\pi}{2}, \frac{\pi}{2}]$ is not considered as far-fetched for the intended application.

In a 2D view, the superior half-plane of the KSV consists in the combination of two areas, \mathcal{A} and \mathcal{B} , defined by the coordinates (x, y) , such that:

$$\mathcal{A} = \{(x, y) \in \mathbb{R}^2 : x^2 + (y - y_A)^2 \geq r^2, \\ (x - x_B)^2 + (y - y_B)^2 \geq r^2, 0 \leq y \leq y_P\},$$

$$\mathcal{B} = \{(x, y) \in \mathbb{R}^2 : (x - x_B)^2 + (y - y_B)^2 \leq r^2, y \geq 0\}$$

while the circular area \mathcal{C} is part of the unfeasible space and is defined as:

$$\mathcal{C} = \{(x, y) \in \mathbb{R}^2 : x^2 + (y - y_A)^2 < r^2\}$$

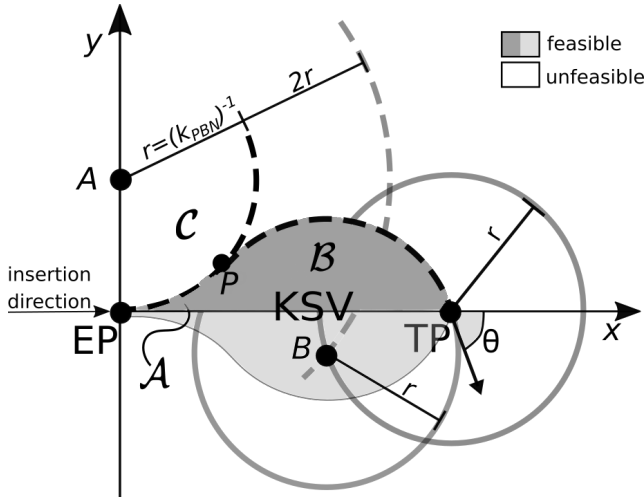


FIGURE 3.2: A 2D representation of the Kinematics Search Volume (KSV). The insertion happens at the entry point (EP). Part C can not be reached by the PBN due to the minimum bending radius and it is part of the unfeasible area. KSV is represented in gray. Its superior half-plane derives from the combination and intersection of the circumferences centered in $A(x_A = 0, y_A = r)$, $B(x_B, y_B)$ and the TP. The rest of the space is labelled as "unfeasible" as it can not generate any feasible trajectory to reach the TP. The value r represents the minimum bending radius admitted by the PBN and θ the insertion orientation.

where $r = \frac{1}{k_{PBN}}$. $\mathbf{B}(x_B, y_B)$ is the intersection between the r -radius circle centered in the TP and the $2r$ -radius circle centered in $\mathbf{A}(x_A = 0, y_A = r)$. \mathbf{B} represents the center of a r -radius circle in the negative half-plane. The point $\mathbf{P}(x_P, y_P)$ is the intersection between the circle centered in \mathbf{B} and the r -radius circle with center \mathbf{A} .

With a similar approach, it is possible to compute the inferior half-plane, represented in Fig. 3.2 in light grey. This method is applicable until the condition $\|TP - EP\| < \sqrt{8}r$ is valid, i.e. until it is possible to define the point \mathbf{B} . For the present application, this condition is satisfied unless the Euclidean distance between EP and TP is greater than 202 mm, which is large enough to cover the entire working volume.

For each $EP_{i,a}$, $i \in 1, \dots, N_a$ defined in Section 3.3.1, the smart redefinition of the workspace is performed by considering, for the path planning, only the uniformly-distributed points included in the $KSV_{i,a}$, in 3D.

The planning is performed similarly to Favaro et al., 2018b: in a random fashion, the samples included in the $KSV_{i,a}$ are sequentially provided to the planner, which builds a connected graph. The graph is composed by vertexes, \mathbf{P} , corresponding to samples in the free space of $KSV_{i,a}$. Linear edges are used to connect adjacent vertexes. When a new sample is probed, the vertex that features the shortest path to $EP_{i,a}$ is identified and, as the obstacle clearance of the new edge is verified, the connection is performed. The collision check is carried out considering a minimum distance from obstacles equal to half the PBN diameter for guaranteeing the practicability of the edge. The graph keeps evolving following an RRT* approach until a piece-wise linear pathway able to connect the $EP_{i,a}$ to the TP is found. A first raw path, $\text{sol}_1^{i,a}$, is thus defined as a sequence of vertexes:

$$\{\text{sol}_1^{i,a}\} = \{\mathbf{P}_{k,1}^{i,a} \in \mathbb{R}^3, k = 1, \dots, N_{\mathbf{P},1}^{i,a}\}$$

where $\mathbf{P}_{1,1}^{i,a} = \text{EP}_{i,a}$ and $\mathbf{P}_{1,N_{\mathbf{P},1}}^{i,a} = \text{TP}$. The length ($l_{pw}^{sol_j^{i,a}}$) is considered as an index of goodness for a generic piece-wise linear solution $sol_j^{i,a}$:

$$l_{pw}^{sol_j^{i,a}} = \sum_{k=1}^{N_{\mathbf{P},1}^{i,a}-1} \|\mathbf{P}_{k+1,j}^{i,a} - \mathbf{P}_{k,j}^{i,a}\|$$

and represents the sum of the distances between consecutive $\mathbf{P}_k^{i,a}$ in the sequence from the $\text{EP}_{i,a}$ and the TP.

Every time a new sample is provided to the planning algorithm, the planner verifies whether the new sample allows to define $sol_j^{i,a}$ featuring a shorter length.

This step ends when either all the samples in $\text{KSV}_{i,a}$ are provided to the planner or the number of computed $sol_j^{i,a}$ reaches a predefined threshold (N_{sol}^{max}).

3.3.3 Path approximation and optimization

In this section the objective is to generate smooth paths based on the previously computed way-points. We employed an evolutionary optimization process to optimize the weights for the NURBS, used to represent the smooth trajectory.

Each $sol_j^{i,a}$ defined in the previous section needs to:

1. be smoothed, to comply with the \mathcal{C}^2 continuity required by the PBN;
2. be checked for the obstacle clearance;
3. have minimum length.

Additionally, they have to comply with the maximum curvature achievable (k_{PBN}). An Evolutionary Optimization Procedure (EOP) is then run for each $sol_j^{i,a}$. In the work of Jalel, Marthon, and Hamouda, 2015, a solution for path optimization based on NURBS tuning in simplified 2D workspace is proposed. In the present paper, a similar approach is used for defining \mathcal{C}^2 curves in 3D using the way-points discovered in the path planning phase and obtain smooth, curvature-constrained paths with minimal length and minimal variations of curvature.

A scheme of the EOP is reported in Fig. 3.3 and a simplified 2D depiction is shown in Fig. 3.5.

Population initialization

A general p^{th} -degree NURBS for $\text{sol}_j^{i,a}$, is defined in parametric form as:

$$C(u)_j^{i,a} = \frac{\sum_{k=0}^{N_{\mathbf{P},j}^{i,a}} B_{k,p}(u) w_k^{j,i,a} \mathbf{P}_k}{\sum_{k=0}^{N_{\mathbf{P},j}^{i,a}} B_{k,p}(u) w_k^{j,i,a}}$$

where \mathbf{P}_k are the control points, $w_k^{j,i,a}$ are the weights linked to each \mathbf{P}_k and $B_{k,p}(u)$ are the p^{th} -degree B-spline basis functions defined on $u \in [0, 1]$. If the weight $w_k^{j,i,a}$ coupled to a control point \mathbf{P}_k is moved, this affects only a portion of $C(u)_j^{i,a}$, allowing the local shape control: increasing (decreasing) the magnitude of $w_k^{j,i,a}$ pulls (pushes) the curve closer to (away from) \mathbf{P}_k . For further details about NURBS, the reader is referred to Piegl and Tiller, 1996.

The EOP generates a primitive population of Non-Uniform Rational Beta Splines (NURBS) from $\text{sol}_j^{i,a}$. Each NURBS is referred as “individual” (ind) and has the vertexes $\mathbf{P}_k \in \text{sol}_j$ as control points. By randomly initializing the weights $w_k^{j,i,a}$ associated to $\mathbf{P}_k \in \text{sol}_j$, the individuals in the population of NURBS are obtained:

$$\{\text{ind}_t^{j,i,a}\} = \{\mathbf{P}_k^{j,i,a} \in \mathbb{R}^3, w_{k,t}^{j,i,a} \in \mathbb{R}, t = 1, \dots, N_t\}$$

where N_t represents a constant, pre-set number of individuals in the population.

Objective function

the variable $u \in [0, 1]$ used to define each $\text{ind}_t^{j,i,a}$ in parametric form undergoes a discretization, as explained in Appendix 6.1.

An objective function F_{obj} is defined, which is used by the EOP to rank the performance of each $\text{ind}_t^{j,i,a}$, as in Jalel, Marthon, and Hamouda, 2015:

$$F_{obj}(\text{ind}_t^{j,i,a}) = \alpha \cdot l(\text{ind}_t^{j,i,a}) + \beta \cdot \#P_o + \gamma \cdot \#P_c + \delta \cdot SD$$

which minimizes:

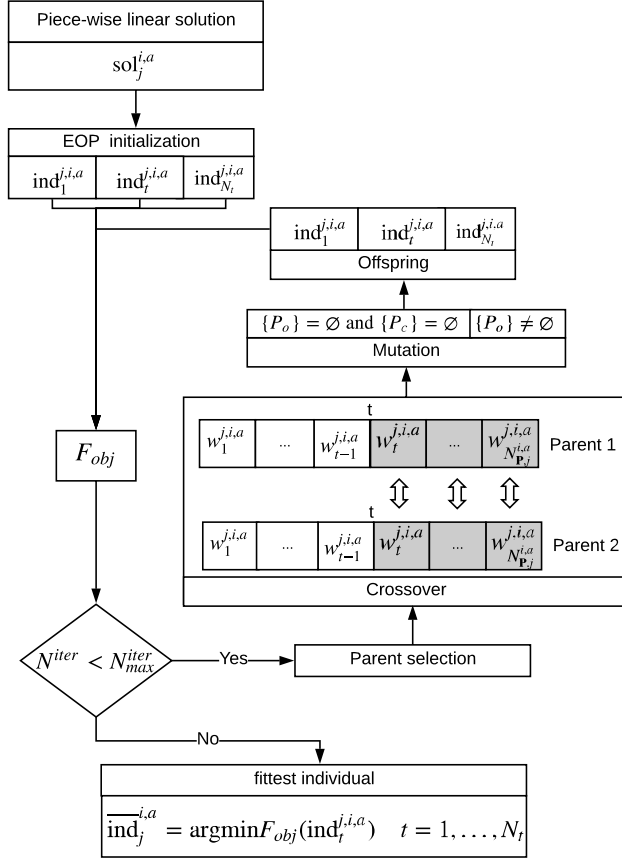


FIGURE 3.3: In the diagram, the steps composing the EOP are depicted. The initial piece-wise linear solution ($\text{sol}_j^{i,a}$) is provided to the EOP, and the initial population of individuals is generated by providing random values to the $w_{k,t}^{j,i,a}$. F_{obj} is then run and the parent selection is carried out as explained in Sec. 3.3.3. Then the crossover (Sec. 3.3.3) and the mutation (Sec. 3.3.3) happen, according to each specific probability. The population is then updated. The process continues until a predefined number of iteration (N_{max}^{iter}) is achieved and the fittest individual ($\overline{\text{ind}}_j^{i,a}$) is returned as output.

- the length l : the integral of the derivative of $\text{ind}_t^{j,i,a}$ over its length, calculated as in Piegl and Tiller, 1996:

$$l(\text{ind}_t^{j,i,a}) = \int_{EP_{i,a}}^{TP} \|\text{ind}'_t^{j,i,a}(u)\| du$$

- $\#P_o$: the number of points $\in \text{ind}_t^{j,i,a}$ intersecting an obstacle:

$$\{P_o\} : \{\text{ind}_t^{j,i,a} \cap \Omega_{obs}\}$$

where $\{\Omega_{obs}\} \subset \text{KSV}_{i,a}$ is the set of 3D points representing the obstacle space.

- $\#P_c$: the number of points $\in \text{ind}_t^{j,i,a}$ to which a curvature (as the second derivative of $\text{ind}_t^{j,i,a}$) larger than k_{PNB} is associated:

$$\{P_c\} = \{\text{ind}''_t^{j,i,a} > k_{PNB}\}$$

- SD : the standard deviation of the curvature of $\text{ind}_t^{j,i,a}$, associated to the smoothness of the path whose reduction leads to a lower effort from the needle control system:

$$SD = \sqrt{\frac{1}{N_{samp}} \sum^{N_{samp}} (\text{ind}''_t^{j,i,a} - \mu_{\text{ind}''_t^{j,i,a}})^2}$$

where $\mu_{\text{ind}''_t^{j,i,a}}$ and N_{samp} are the mean and the number of samples of $\text{ind}''_t^{j,i,a}$ that depend upon the discretization of $u \in [0, 1]$.

α, β, γ and δ values are reported in Table 3.1.

Parent selection method

Differently from the solution proposed in Jalel, Marthon, and Hamouda, 2015, a linear Rank-based Roulette Wheel method (Razali and Geraghty, 2011) is used for parent selection. This selection strategy prevents from the risk to fall

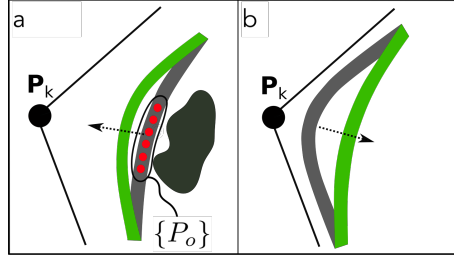


FIGURE 3.4: The controlled mutation algorithm. In *a*), where part of the curve results too close to an obstacle (red points over the grey line), i.e. $\{P_o\} \neq \emptyset$, the weight of $P_k^{j,i,a}$ that affects that part of the curve is decreased until obstacle avoidance is obtained (green line). In *b*), the weights $P_k^{j,i,a} \in \text{ind}_t^{j,i,a}$ are decreased in order to smooth the curve.

into a local minimum during the EOP. At any new generation, it assigns to each $\text{ind}_t^{j,i,a}$ in the population a probability p to be selected as a parent:

$$p(\text{ind}_t^{j,i,a}) = \frac{\text{rank}(\text{ind}_t^{j,i,a})}{\sum_{t=1}^{N_t} \text{rank}(\text{ind}_t^{j,i,a})}$$

where *rank* is defined as:

$$\text{rank}(\text{ind}_t^{j,i,a}) = 2 - SP + \frac{2(SP - 1)(\text{pos}_t^{j,i,a} - 1)}{N_t - 1}$$

where $\text{pos}_t^{j,i,a}$ is the hierarchical position of $\text{ind}_t^{j,i,a}$ in the population according to F_{obj} and SP represents the “selective pressure”, a favorable bias given to individuals having low F_{obj} . With $SP = 1$, all the individuals of the population have the same rank and thus the same probability to be chosen. If $SP = 2$, high-performing parents (the ones with low F_{obj}) have a high rank and thus a higher probability to be selected with respect to less-performing ones.

Crossover

Crossover consists in switching part of the weights between two parent individuals. In this work, a single-point crossover is used, with a cutting point (t) randomly selected at each iteration. The crossover can happen according to a predefined probability p_{cross} . Due to its random nature, crossover can lead to

offspring that do not meet the condition $\{P_o\} \wedge \{P_c\} = \emptyset$. This possibility is envisaged by the algorithm, and regardless if such a situation happens or not, the offspring are stored.

Mutation

Mutation can happen at each iteration of the EOP according to a predefined probability p_{mut} . To avoid the definition of unfeasible path, we implemented a controlled mutation method similar to Jalel, Marthon, and Hamouda, 2015, using a supervised adjustment of the weights in the new individual of the offspring as presented in Appendix 6.2 and shown in Fig. 3.4. If part of the curve results too close to an obstacle, i.e $\{P_o\} \neq \emptyset$, the weight of $\mathbf{P}_k^{j,i,a}$ that controls that part of $\text{ind}_t^{j,i,a}$ is increased until the condition $\{P_o\} = \emptyset$ is achieved (Fig. 3.4a). If part of the curve shows $\{P_c\} \neq \emptyset$, the weights $\mathbf{P}_k^{j,i,a} \in \text{ind}_t^{j,i,a}$ are decreased until all the curve points meet the curvature limit. Additionally, whenever possible, the weights $\mathbf{P}_k^{j,i,a} \in \text{ind}_t^{j,i,a}$ are decreased in order to smooth the curve but without voiding the condition $\{P_o\} \neq \emptyset$ (Fig. 3.4b). In case, as the result of the mutation, the new individual shows a higher value of objective function than the original one, the new individual is rejected and the original one restored.

The EOP stops when the number of generations reaches a predefined threshold (N_{max}^{iter}). For each sol_j , the individual of the NURBS population that features the lower F_{obj} while guaranteeing the condition $\{P_o\} \wedge \{P_c\} = \emptyset$ is stored as $\overline{\text{ind}}_j^{i,a}$:

$$\overline{\text{ind}}_j^{i,a} = \text{argmin } F_{obj}(\text{ind}_t^{j,i,a}) \quad t = 1, \dots, N_t.$$

If no individual meets the condition $\{P_o\} \wedge \{P_c\} = \emptyset$, the algorithm returns no solution for the specific sol_j .

3.3.4 Exhaustive search for the best path

In this section, the cost function used to perform an exhaustive study of the paths discovered in the previous section is presented.

In order to define the optimal path for the specific EP_i in the entry area a , the algorithm performs an evaluation over $\overline{\text{ind}}_j^{i,a}, \forall j$ through a cost function F_{cost}

defined as:

$$F_{cost}(\overline{\text{ind}}_j^{i,a}) = a \frac{1}{d_{min} + \bar{d}} + b \frac{l - l_{min}}{l_{min}} + c \frac{k_{max}}{k_{PBN}}$$

where d_{min} represents the closest distance from an obstacle calculated over the whole length l of $\overline{\text{ind}}_j^{i,a}$, d_{safe} is a safety margin used to take into consideration possible control errors that may happen during the PBN insertion and that linearly increases as the insertion proceeds, as in Favaro et al., 2018b. The mean value of the distance from the obstacles is \bar{d} , while l_{min} is the Euclidean distance between EP_i and TP and $k_{max} = \max(\overline{\text{ind}}_j^{i,a}(u))$.

With $\overline{\text{ind}}_j^{i,a}$ we refer to the best curvilinear path corresponding to the one among all $\overline{\text{ind}}_j^{i,a}$ that has the lower value of F_{cost} . A representation of the EOP and the Exhaustive search for the best path is shown in Fig. 3.5.

As the EOP and the exhaustive search is performed for all the EP_i belonging to the entry area a , a number of best pathways (that, if the planning does not fail, correspond to the number of EP_i) are provided to the surgeon as output of the algorithm. If no solution exists for the specific entry area a , the planner returns a failure.

3.4 Experimental protocol

3.4.1 Input dataset

The dataset used for the experimental trials consists of one brain reconstructed from Magnetic Resonance Imaging acquisitions performed at the Excellence Centre for High Field MR (CERMAC), Vita-Salute San Raffaele University, Milano, Italy.

The anatomical obstacles were identified and segmented in the patient dataset using 3D Slicer© and consist in blood vessels, ventricles, thalamus and globus pallidus. The curvature of the brain cortex was computed using Freesurfer Fischl, 2012.

10 entry areas of 10mm-radius (a dimension consistent with the one employed in Scorza et al., 2017), were defined on the cortical surface resembling possible entry areas in clinical practice, 5 on the left and 5 on the right hemisphere (Fig.

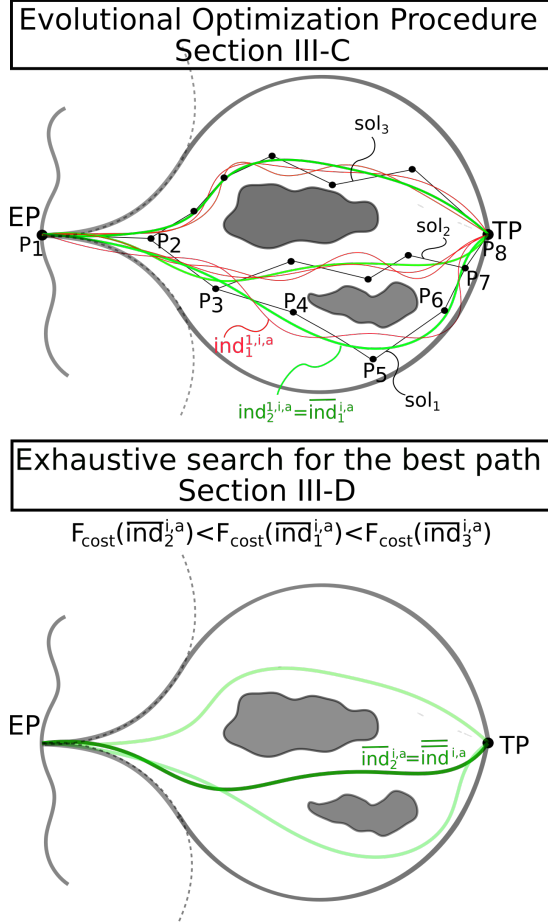


FIGURE 3.5: In the uppermost figure, the EOP is presented. Three piecewise linear solutions are depicted in black ($\text{sol}_{1,\dots,3}$), along with multiple curvilinear approximations ($\text{ind}_t^{j,i,a}$) in red. The best solution for each sol_j is reported in green as $\overline{\text{ind}}_j^{i,a}$. In the picture underneath, referred as “Exhaustive search for the best path”, the cost function described in Section 3.3.4 is implemented to define, among the 3 $\overline{\text{ind}}_1^{i,a}, \dots, \overline{\text{ind}}_3^{i,a}$, the best one: $\overline{\text{ind}}^{i,a}$.

TABLE 3.1: Parameters used in the experimental setup. From the left to the right, the PBN diameter and maximum degree of curvature are reported, followed by a the pre-set maximum number of raw path (N_{sol}^{max}) allowed at each iteration of Section 3.3.2. The EOP is defined by the initial population size N_e . The number of offspring (N_{iter}^{max}), the cross-over and mutation probabilities (P_{cross} and P_{mut}) as well as the value assigned to the selective pressure (SP) are also reported. Lastly, the values of the weight used in the Objective and the Cost functions are shown.

PBN params		Path planner		EOP settings			Objective Function				Cost Function			
$\varnothing[mm]$	$k_{PBN}[mm^{-1}]$	N_{sol}^{max}	N_t	N_{iter}^{max}	P_{cross}	P_{mut}	SP	α	β	γ	δ	a [mm]	b	c
2.5	0.014	5	20	50	0.5	0.1	1.8	100	1	1	100	0.01	0.5	0.5

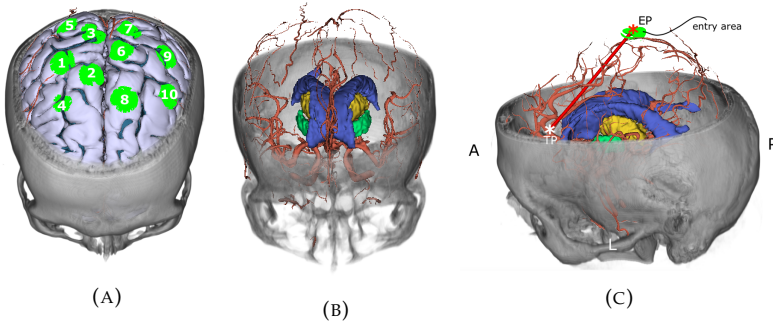


FIGURE 3.6: In a) a picture of the 10 entry areas defined on the brain cortex for the scope of the test (5 on the left and 5 on the right hemisphere) is presented. In b), the anatomical obstacles considered in the planning phase are depicted in different colors: ventricles (blue), thalamus (yellow), globus pallidus (green) and blood vessels (red). In c), an example of a planned curvilinear path is proposed (sharp red). The entry and target points are labelled respectively as EP and TP. The entry area is also shown in sharp green around the EP.

3.6).

10 TPs were set (one for each entry area) in different location within the brain. Using the method described in Section 3.3.1, the maximum number of 20 EPs was been set for each entry area, resulting in a distance between EPs and TPs having a median value of 78.02mm. The entire workflow described in Fig. 3.1 is run over all the entry areas.

All the relevant parameters used in the simulations for the presented method are reported in Table 3.1. The maximum number of raw paths (N_{sol}^{max}) as well as the parameters included in the cost functions were defined empirically. Parameters included in the Evolutionary Optimization Procedure, including those used in the objective function, were empirically adapted to values close to the ones used in Jalel, Marthon, and Hamouda, 2015.

3.4.2 Simulations and data analysis

Performance evaluation

In the first performance evaluation test, our solution was compared with two sampling-based planning methods: the previous version of the planner (Favaro et al., 2018b), referred as “Ellipsoidal”, and the RG-RRT proposed by Patil et al. Patil and Alterovitz, 2010. The latter consists in a combination of the RRT-based search and a reachability-guided sampling heuristic.

The comparison between the different algorithms was carried out in terms of mean distance from anatomical obstacles (\bar{d}), the normalized path length (\hat{l}) as the percentage the path length exceeds the Euclidean distance between the $EP_{i,a}$ and the TP, the minimum distance along the entire path from the closest anatomical obstacle (d_{min}) and the value of F_{cost} . The maximum curvature (k_{max}) was checked as a critical parameter which relates to a higher risk of inaccuracies in the control of the PBN during the trajectory tracking (Ko, Frasson, and Rodriguez Y Baena, 2011). The failure rate (FR) was also evaluated, defined considering the number of best solution computed by the planning algorithm ($\#\{\overline{\text{ind}}^a\}$) and the number of original EPs defined over the entry area a ($\#\{EP_{i,a}\}$), such that:

$$FR_a = \frac{\#\{\overline{\text{ind}}^a\}}{\#\{EP_{i,a}\}}.$$

The maximum curvature value achievable by the needle (k_{PBN}) was used in the simulation and the nominal catheter thickness is considered for assessing obstacles avoidance, as reported in Table 3.1. For all the algorithms, the search is biased by providing the TP as new sample with a probability of 10%. When analyzing a new sample, the maximum Euclidean distance between the sample and the closest vertex in the graph is 40mm for the KSV and the Ellipsoidal method. No maximum Euclidean distance is considered for arc reachability in the RG-RRT. As foci for the Ellipsoidal method, the EP and TP are considered. Variation in the ellipsoidal shape happens when a number $N_v = 5 * k * N_{reshape}$ of new vertexes are added to the graph without reaching the TP, where $N_{reshape}$ is the number of reshape iterations and $k = 1.5$ is an

increasing factor. Ellipsoidal shape variation is carried out by enlarging the minor axis by a factor k , starting from a value of 10 mm. An upper limit of 1000 samples is considered for all algorithms before quitting the search.

A Friedman non-parametric statistical analysis was used ($p < 0.05$), followed by a post-hoc Wilcoxon matched pairs test ($p < 0.016$, Bonferroni correction).

A second performance test have been conducted to compare the proposed solution with an optimal planner. For this scope, an A* algorithm has been implemented. Tests were performed on one insertion point, corresponding to the centre point of the entry area 1 in Fig. 3.6. A total of 5 repetitions of the KSV algorithm have been run. As a minimum distance from the obstacle, the nominal catheter thickness is considered. As a terms of comparison, the normalized path length, the minimum and mean distance from obstacles and computational time are considered. The maximum curvature is disregarded in the comparison as A* provides piece-wise linear paths.

Computational time

A further test has been designed for evaluating the benefit in terms of computational time of associated to confining the path planning within a subset of the original workspace where kinematically-feasible solutions can lie. To this end, a path planning comparison was performed between the herein-presented KSV and the Ellipsoidal method described in Favaro et al., 2018b. In the test, only the time required to find the set of piece-wise linear raw paths ($\text{sol}_j^{i,a}$) is measured as the subsequent steps of approximation and optimization are independent of the workspace size and different between the two algorithms. Results from the RG-RRT are not considered in this test as the method does not include an intermediate step of raw paths estimation (as in the KSV and Ellipsoidal method), but provides paths that are already curved. 10 trials were performed using the 10 EPs and the 10 TPs described in Section 3.4.1. A pairwise comparison was performed via Wilcoxon matched pairs tests ($p < 0.05$).

All simulation tests were performed using 3D Slicer© , on a MacBook Pro

(MacOS 10.14.6, 2,7 GHz Intel Core i5, 8 GB of RAM) and the same parameterization has been used in the test of performance and computational time.

3.5 Results

Results from the first performance evaluation are presented in Fig. 3.7, where the method herein presented is compared to the ellipsoidal solution of Favaro et al., 2018b ("*Ellips.*") and the RG-RRT by Patil and Alterovitz, 2010. In Fig. 3.7a, the highest value of curvature reached along the path (k_{max}) shows respectively a median value of 0.01 mm^{-1} (radius of curvature $r=100 \text{ mm}$), $6.2 \times 10^{-3} \text{ mm}^{-1}$ ($r=161.3 \text{ mm}$) and $6 \times 10^{-4} \text{ mm}^{-1}$ ($r=1667 \text{ mm}$) for the RG-RRT, Ellipsoidal and KSV algorithm, respectively ($p < 0.01$).

The median minimum distance from anatomical obstacles (d_{min}) resulted in 0.19 mm for the KSV, 0.63 mm for the RG-RRT and 0.34 mm for the Ellipsoidal (Fig. 3.7b) while the mean distance (\bar{d}) showed a median value of 9.1 mm for the KSV, 6.06 mm for the RG-RRT and 7.26 mm for the Ellipsoidal ($p < 0.01$) (Fig. 3.7c).

With regard to the normalized path length (\hat{l}), its median values were equal to 1.19 %, 2.92 % and 2.35 % for the KSV, RG-RRT and Ellipsoidal, respectively ($p < 0.01$) (Fig. 3.7d).

For the KSV, F_{cost} demonstrates a median value of 0.017, a value of 0.35 was found for the RG-RRT and of 0.215 for the Ellipsoidal method ($p < 0.01$) (Fig. 3.7e).

For the last parameter analyzed, the failure rate FR , its median value for the KSV was 5.2 %, for the RG-RRT was 33.7 % and for the Ellipsoidal was 21.1 % ($p < 0.05$) (Fig. 3.7f).

From the comparison of the presented solutions with the A* algorithm, results are presented in Table. 3.2, where the difference in term of normalized path length, minimum and mean distance from obstacles and computational time are reported.

TABLE 3.2: Performance test between A* algorithm and the presented solution in term of normalized path length, minimum and mean distance from obstacles and computational time as 25th, 50th and 75th percentiles.

A* - KSV performance comparison				
	A*	KSV		
		25 th	50 th	75 th
\hat{l}	1.017	1.0005	1.0015	1.0029
d_{min} [mm]	1.04	0.028	0.25	0.39
\bar{d} [mm]	4.89	5.43	5.94	6.17
comp. time [sec]	126	34.0226	45.2476	55.5795

TABLE 3.3: Results in term of computational time are shown for an ellipsoidal and a KSV searching space as 25th, 50th and 75th percentiles. Statistical significance effect of the type of search space has been found through a Wilcoxon matched pairs test ($p < 0.05$).

Computational time			
	25 th	median	75 th
ellipsoidal [sec]	89.58	96.75	107.95
KSV [sec]	4.19	4.28	5.29

Results from the computational time are shown in Table 3.3, where the difference between a KSV and an ellipsoidal search space are reported. In the estimation of the initial raw paths, KSV showed a median value of 4.28 sec while the ellipsoidal approach resulted in a median computational time of 96.75 sec ($p < 0.01$).

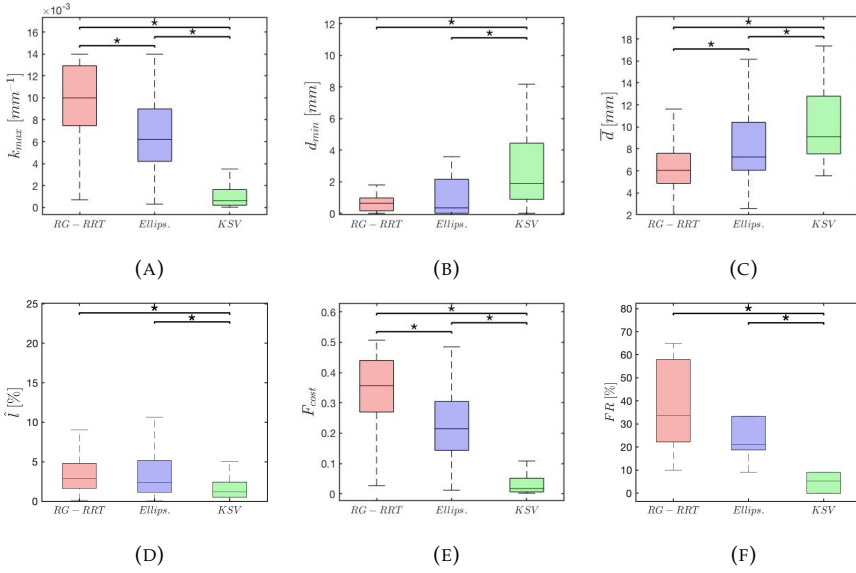


FIGURE 3.7: Results from the comparison between the presented solution (the KSV) and other two methods proposed in the literature: the ellipsoidal search method proposed in Favaro et al., 2018b (referred as “Ellips.”) and the RG-RRT. The maximum curvature (k_{max}), the minimum and mean distance from anatomical obstacles (d_{min} , \bar{d}), the normalized path length (\hat{l}) and the overall cost (F_{cost}) are reported respectively in a,b,c,d and e. In f), the failure rate FR is also shown. Statistical significance between different algorithms is highlighted (*, $p < 0.05$).

3.6 Discussion

This work presents a planning solution for computing pathways suitable for being performed by a flexible catheter (PBN) in neurosurgical applications and used combined with a bespoke control and actuating systems so that they can be used as surgical trajectories.

A smart redefinition of the search space, i.e. the KSV, considers the curvature limit of the PBN (k_{PBN}) and ignores those parts of working domain that will give rise to unfeasible paths. This allows the algorithm to save time. By looking at Table 3.3, where the KSV is compared to the ellipsoidal search volume used in Favaro et al., 2018b, a significant decrease of the computational time (~ 20 times) can be noticed. Furthermore, a new approximation method, based on the use of NURBS, provides the C^2 continuity required by the PBN and a local control of the approximated path allowing, together with a bespoke evolutionary optimization procedure, to optimize each solution according to several parameters. The combination of these two elements provides a high level of flexibility thanks to the chance to modify the weight associated to each control point in a way to privilege some aspects (e.g. the distance from obstacles) more than others and at a level that was not achievable by other approaches as those based on inverse kinematics (Duindam et al., 2010) or potential fields methods (Li et al., 2014) that have, on the other hand, the benefit of allowing a quasi-real-time path computation. The evolutionary optimization procedure, even if it cannot be expected assuredly to find the global optimum (which can be, instead, obtained if a graph-based approach is used), can generate an excellent quasi-optimal solution (Razali and Geraghty, 2011) without the extreme computational payload that characterizes graph-based approaches.

When compared with two other sampling-based planning solutions (Favaro et al., 2018b and Patil and Alterovitz, 2010), our method was able to outperform them in two relevant parameters: the distance from anatomical obstacles and the normalized path length, as shown in Fig. 3.7. The obtained path was also smoother, which represents a good starting point in the view of reducing the possible control error in trajectory tracking. The obtained overall cost resulted smaller in our solution with respect to the other two algorithms and

demonstrated a lower risk of failure in the path search: the KSV algorithm failed respectively 4 times and 6 times less frequently than Favaro et al., 2018b and Patil and Alterovitz, 2010.

Despite the proposed approach is intended for pre-operative applications, the fast computation exhibited by the planner for the definition of the KSV and the estimation of the raw path ($\text{sol}_j^{i,a}$) suggests the possibility to achieve computational time compatible with intra-operative planning if implemented in C/C++ (rather than in Python, as in this paper). Additionally, the introduction of a bidirectional-RRT search (Jordan and Perez, 2013) would further speed up the initial search for the raw paths by letting the graph evolving from the EP_i^a and the TP at the same time. To this end, benefits deriving from the use of reinforcement learning approaches will be also evaluated. The real bottleneck of the presented solution in terms of computational cost is represented by the evolutionary optimization procedure, which may be speed up by reducing the computational cost associated to the mutation of the individuals.

In terms of path optimality, our solutions demonstrated results that closely resemble the one obtained by the A* algorithm, considered as our gold standard in terms of path optimality. The safer paths provided by the A* algorithm in terms of minimum distance from obstacles were found at the expense of a slightly longer path and longer computational time, as expected from a graph-based planning method in 3D scenarios.

The quasi-optimal path estimated by the proposed solution assumes a kinematic model of motion for the PBN during insertion and a proper control system exist. In Secoli, Rodriguez, and Baena, 2018, an adaptive controller combined with a kinematic model of the PBN needle in Parallel Transport Frame are proposed. Test performed in-vitro demonstrated the ability of the controller method to perform curvilinear paths, provided that they meet the PBN curvature limit. The test were performed over multiple curvilinear paths comparable to the one estimated in this work in terms of insertion length and curvature. This implies that the present solution can be considered as a feasible path planner for such a control method. Further in-vitro tests will be conducted using paths estimated by the present solution in order to evaluate the system tracking error and determine the uncertainty margin.

3.7 Conclusions

The chapter addresses **Hypothesis 1** describing a solution for the definition of feasible pathways for robotically-actuated flexible needles in a neurosurgical scenario, which represents a typical example of dense environment characterized by narrow spaces.

A smart redefinition of the working space based on the maximum curvature of a neurosurgical steerable needle (in the present case, the PBN) is used to limit the sampling-based path search within a confined region where feasible solutions can lie, guaranteeing a computational time consistent with standard pre-operative planning (**Hypothesis 1.2**). This, combined with an optimization based on a bespoke evolutionary procedure, results in providing a significant improvement of the performance in terms of a higher obstacle avoidance and a reduced path length (**Hypothesis 1.1**). The planning solution could also reduce the failure rate in finding a path for a specific query, augmenting the pool of possible solution where to look for the best path. This lies the foundation for a further enhancement in the quality of the estimated paths as well as for a real-time path computation through the reduction of the computational cost.

Chapter 4

Model-based robust pose estimation for a multi-segment, programmable bevel-tip steerable needle

Bevel-tip steerable needles for percutaneous intervention are prone to torsion determined by the interaction forces with the human tissue. If disregarded, torsion can affect the insertion accuracy inducing a change in the needle tip orientation, which is generally undetectable by tracking devices because of the small diameter of the needle. In this chapter, we investigate **Hypothesis 2** and present a method for estimating the tip pose (i.e. position and orientation) of a multi-segment needle. We initially address **Hypothesis 2.1** with an implementation of the method for a simplified version of the PBN (referred as sPBN hereinafter) featuring two segments. **Hypothesis 2.2** is then addressed extending the proposed solution on the four-segment PBN needle, for which a novel 3D kinematic model is developed. In the solution, a kinematic based Extended Kalman Filter (EKF) is used. The tip position of the steering segments is tracked by electromagnetic sensors and used as input measurement. Simulation trials and experiments in phantom-brain gelatin were performed to prove the performance of the method and mimic real case scenarios. In the case of the sPBN, the solution show state-of-the-art performances in pose estimation with a bounded position error of < 1 mm and orientation error of < 5 deg. Results obtained using the four-segment PBN demonstrated a small position error (RMSE <0.6 mm) and good accuracy in comparison to a bespoke geometric pose reconstruction method.

The application of the method on the two-segment PBN resulted in a journal paper ¹ currently under review.

The application of the method on the four-segment PBN resulted in a conference paper ² currently under review.

4.1 Introduction

Percutaneous needle insertion is a common medical approach used for procedures such as biopsy, brachytherapy, drug delivery and thermal ablation to achieve minimally-invasive access to different organs and body regions as the breast, kidney, liver, prostate and brain (Cowan et al., 2011; Abolhassani, Patel, and Moallem, 2007). In these contexts, this approach is often preferred to standard open surgery for the reduced tissue trauma and the faster recovery time.

Nonetheless, percutaneous interventions can be challenging when the targeted tissue is deep inside the body due to the presence of anatomical structures to be avoided and the onset of needle deflection caused by tissue inhomogeneity and deformation (Misra et al., 2010).

Recent effort has been applied to the design of steerable percutaneous needles, the steering of which can be robotically controlled so as to perform nonstraight paths, allowing the needle to avoid the anatomical obstacles and increase the tip placement accuracy. An overview of steerable needle designs is reported in Berg et al., 2015. These include the Programmable Bevel-tip Needle (PBN), a multi-segment steerable needle composed of four axially-interlocked slender sections, which are robotically actuated to develop specific tip configurations that allow the needle to steer.

A significant component required to bring these robotically-actuated steerable needles into use is the development of appropriate control strategies to achieve an accurate insertion. This can be obtained in a closed-loop fashion

¹A. Favaro, R. Secoli, F. Rodriguez y Baena and E. De Momi, "Model-based robust pose estimation for a multi-segment, programmable bevel-tip steerable needle", *Robotics and Automation Letters*, under review

²A. Favaro, R. Secoli, F. Rodriguez y Baena and E. De Momi, "Optimal pose estimation method for a multi-segment, programmable bevel-tip steerable needle", *International Conference on Intelligent Robots and Systems (IROS)*, under review

if the position and the orientation of the needle (i.e. its full pose) are known. An overview of the recent progress made in closed-loop needle steering is reported in Rossa and Tavakoli, 2017. Still, with flexible needles, closed-loop control is not trivial as the tip is not rigidly connected to the base. Needle tracking methods can thus be used, as X-Ray fluoroscopy (Ralovich et al., 2014), ultrasound (US) (Vrooijink, Abayazid, and Misra, 2013; Chatelain, Krupa, and Marchal, 2013) and electromagnetic (EM) tracking systems (Sadjadi, Hashtrudi-Zaad, and Fichtinger, 2012). However, imaging methods cannot track the rotation of the needle about its insertion axis (the roll angle) because of its small diameter (Cowan et al., 2011), which also precludes the possibility to accommodate a 6 Degrees of Freedom (DoF) EM sensor.

In Vrooijink, Abayazid, and Misra, 2013, this limitation in needle tracking was handled by considering the roll angle at the needle tip as equal to the one measured at the base, assuming infinite torsional stiffness of the needle. This assumption underlies several control systems and shape reconstruction methods (Shahriari et al., 2015; Abayazid, Kemp, and Misra, 2013; Abayazid et al., 2015), as well as motion planners (Patil et al., 2014; Wooram Park et al., 2005) and kinematic models (Webster et al., 2006).

For the PBN, closed-loop control was achieved by using adaptive control strategies to compensate for unknown, nonlinear mechanical properties (Secoli and Baena, 2016; Secoli, Rodriguez, and Baena, 2018). More recently, these nonlinearities were modelled by using finite-element techniques (Watts, Secoli, and Baena, 2019), creating a new optimised control for the configuration of the segments.

For most of the steerable needle designs, the effect of needle-tissue interactions determines a significant torsional moment. In the case of PBNs, for some tip configurations, experiments demonstrated the onset of an unmodelled needle torsion during the insertion, ascribed to needle-tissue shear forces, which can increase the error in tracking if not measured and subsequently compensated for.

Reed, Okamura, and Cowan, 2009 proposed a solution to model the torsion experienced by a bevel-tip needle controlled through base rotation. This model was later expanded by Swensen et al., 2014 with a length-varying torsional dynamics component. They introduced it in a closed-loop control framework

in combination with C-arm fluoroscopy imaging for needle position tracking. Kallem and Cowan, 2009 presented a feedback controller that stabilizes a bevel-tip steerable needle to a desired 2-D plane. In their work, they used the 3-D needle tip position and estimated the needle torsion applying a Luenberger observer to the reduced and feedback-linearized Webster's model of the needle (Webster et al., 2006). These works, however, are designed for a steerable needle that strongly differs from the PBN in terms of structure, kinematics and steering mechanism (Secoli and Baena, 2016), making them unsuitable for this type of needle.

A solution for the full pose tracking of a PBN was proposed by Khan et al., 2019, where multi-core optical fibers with embedded Fiber Bragg Grating sensors were used. Errors in pose reconstruction were identified since the fibers are not bonded to the needle and can thus experience a different level of torsion with respect to the needle body.

This chapter investigates **Hypothesis 2**. A solution for estimating the full pose of a PBN during the insertion is proposed, which addresses the case of needle torsion. A simplified two-segment PBN (sPBN) (**Hypothesis 2.1**) and the four-segment PBN (**Hypothesis 2.2**) are considered. For some configurations, these PBN designs have shown experimentally to be affected by the onset of a torsional effect around the insertion axis. The method involved an Extended Kalman Filter (EKF) defined on the kinematic model of the needle. Solutions based on Kalman Filters have been widely adopted in the literature for needle tracking and pose estimation. In our work, we used a 2D model of the sPBN and a 3D model of the PBN that originate from the one proposed by Ko, Frasson, and Rodriguez Y Baena, 2011 in 2D, properly extended to contemplate the torsion of the needle and, in case of the PBN, a 3D steering. sPBN and PBN respectively feature two and four axially-interlocked segments, robotically actuated at the base. Their steering direction is determined by the offset at the needle tip between segments. For some configurations, such needle designs have shown experimentally the onset of a torsional effect around the insertion axis. As assumption for mimicking a real test scenario where conventional imaging systems are used, to estimate the full 6 DoF pose only the position of the tip of the needle segments is considered as measurement. Such a solution can be used as a means to inform the PBN control system about the

pose taken by the needle during the insertion process, allowing the controller to compensate for the potential onset of needle torsion.

As the presented method is tested on two different needle designs (sPBN and PBN), with the exception of the Conclusions presented in Section 4.6, the content of each section is first presented with regard to the sPBN design and then to the PBN design.

4.2 Methods

4.2.1 Two-segment PBN (sPBN)

Kinematic model

The sPBN needle can generate a controlled steering in a plane according to the relative offset between the two active beveled-tip segments, as shown in the schematic representation of Fig. 4.1a. The two segments are identified as A and B . Their local frames, \mathbf{X}_A and \mathbf{X}_B , are on the segment tips.

The needle kinematic model described in Ko, Frasson, and Rodriguez Y Baena, 2011 is the following:

$$\begin{bmatrix} \dot{x} \\ \dot{y} \\ \dot{\psi} \\ \dot{\delta} \end{bmatrix} = \begin{bmatrix} \cos(\psi) \\ \sin(\psi) \\ k_1(\delta - \epsilon\psi) \\ 0 \end{bmatrix} v_1 + \begin{bmatrix} 0 \\ 0 \\ 0 \\ 1 \end{bmatrix} v_2 \quad (4.1)$$

where x, y represent the x -axis and y -axis coordinates of the rear segment frame (\mathbf{X}_r) with respect to the global reference frame O . Based on the needle configuration, \mathbf{X}_r can be either \mathbf{X}_A or \mathbf{X}_B , depending on which segment (A or B) is the one ahead of the other. In Fig. 4.1a, \mathbf{X}_r is \mathbf{X}_B while the leading segment (\mathbf{X}_l) is \mathbf{X}_A . The variable ψ represents the angle of rotation of the tip around the z -axis and δ is defined as the relative offset between the two segments at the needle base (see Fig. 4.1a). The coefficient k_1 is a constant defined during the calibration described in Ko, Frasson, and Rodriguez Y Baena, 2011.

v_1 is the cruise speed, i.e. the forward velocity of the whole needle body, while v_2 is the offset velocity, i.e the rate of change of δ .

The sPBN is formed by two segments able to slide relatively to each other. According to this principle, when the needle bends, the inner part of \mathbf{X}_l is in compression and the inner part of \mathbf{X}_r is in tension, resulting in a difference between the offset at the tip (δ_t) and the offset at the base (δ). As reported in Ko, Frasson, and Rodriguez Y Baena, 2011, the relationship between the two offsets is:

$$\delta_t = \delta - \epsilon\psi \quad (4.2)$$

with $\epsilon = (8R_n)/(3\pi)$ for a needle made by two segments, where R_n the radius of the needle.

The rotational velocity $\dot{\psi}$ is linked to the cruise speed v_1 as follows:

$$\dot{\psi} = \rho v_1 \quad (4.3)$$

where ρ is the instantaneous curvature that the needle tip follows. In Ko et al. Ko, Frasson, and Rodriguez Y Baena, 2011, ρ is considered as proportional to δ_t with a coefficient k_1 as follows:

$$\rho = k_1 \delta_t \quad (4.4)$$

and, from (4.2), the expression of $\dot{\psi}$ reported in (4.21) is obtained.

At each time step, δ_t defines the leading segment and the rear segment, such as:

$$\delta_t > 0 \begin{cases} \mathbf{X}_l = \mathbf{X}_A \\ \mathbf{X}_r = \mathbf{X}_B \end{cases} \quad \delta_t < 0 \begin{cases} \mathbf{X}_l = \mathbf{X}_B \\ \mathbf{X}_r = \mathbf{X}_A \end{cases} \quad (4.5)$$

When the offset of the tip is null, i.e. $\delta_t = 0$, frames \mathbf{X}_l and \mathbf{X}_r coincide. Their poses with respect to the world frame O are ${}^O\mathbf{T}_l = {}^O\mathbf{T}_r$.

When $\delta_t \neq 0$, a steering angle ξ is shown between \mathbf{X}_l and \mathbf{X}_r (Ko, Frasson, and Rodriguez Y Baena, 2011), expressed as:

$$\xi = k_1 \delta_t^2 \operatorname{sgn}(\delta_t). \quad (4.6)$$

The radius of curvature (R_c) associated with the angle ξ is defined as:

$$R_c = \frac{\delta_t}{\xi} \text{sgn}(\delta_t). \quad (4.7)$$

The translation ${}^r\mathbf{P}_l$ from \mathbf{X}_r to \mathbf{X}_l (in Fig. 4.1a, respectively \mathbf{X}_B and \mathbf{X}_A) is defined as:

$${}^r\mathbf{P}_l = [R_c \sin(\xi), R_c(1 - \cos(\xi)), 0]^T. \quad (4.8)$$

The transformation ${}^r\mathbf{T}_l$ between \mathbf{X}_r and \mathbf{X}_l is defined as:

$${}^r\mathbf{T}_l = \begin{bmatrix} \mathbf{R}_z(\xi) & {}^r\mathbf{P}_l \\ 0 & 0 & 0 & 1 \end{bmatrix} \quad (4.9)$$

where $\mathbf{R}_z(\xi)$ is the rotation between \mathbf{X}_r and \mathbf{X}_l due to the presence of ξ . The transformation ${}^O\mathbf{T}_l$ between O and \mathbf{X}_l can be computed as:

$${}^O\mathbf{T}_l = {}^O\mathbf{T}_r {}^r\mathbf{T}_l. \quad (4.10)$$

Torsion model

Differences in the roll angle (ϕ) between the tip and the base are a well-known fact for needle that require rotation to steer (Reed et al., 2011; Kallem and Cowan, 2009). In the case of the sPBN, the needle undergoes a torsion because of the interaction between the needle tip and the tissue when an offset δ_t is generated, or for frictional components between segments. This torsion determines a rotation by an angle ϕ about the x-axis that drives the needle from an ideal 2D motion to a 3D displacement (see Fig. 4.1b) and an orientation discrepancy between the needle tip and the base, which does not rotate. The poses of the two segment tips become:

$${}^O\mathbf{T}'_r = \mathbf{R}_x(\phi_r) {}^O\mathbf{T}_r \quad (4.11)$$

and

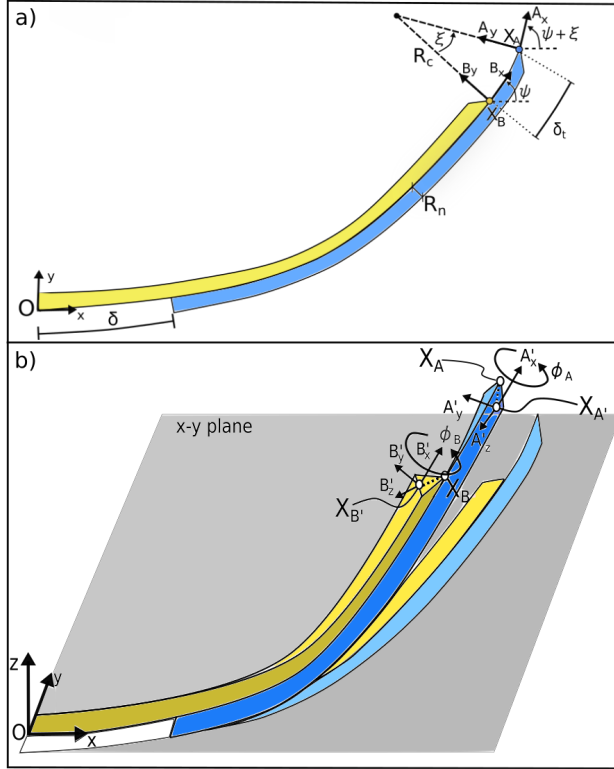


FIGURE 4.1: *Needle kinematics*: in a), a 2D representation of the two-segment sPBN is reported. \mathbf{X}_A and \mathbf{X}_B represent the local frames of segment A and segment B. In the case depicted, $\mathbf{X}_A = \mathbf{X}_l$ and $\mathbf{X}_B = \mathbf{X}_r$. R_n is the needle radius and δ the offset at the needle base. ψ is the rotation of the needle about the z -axis. The offset at the tip, δ_t , differs from δ because of the needle bend, which generates a further curvature ξ associated to a radius R_c . In b), the effect of needle torsion on the original 2D trajectory of segment A and B, depicted on the x - y plane in light blue and light yellow, is reported. The needle moves from planar steering to a spatial movement. The local reference frames of segment A and segment B are reported. The offset between the leading segment (here the segment A) and the rear segment (here the segment B) determines a different torsion on their tips, i.e. $\phi_A \neq \phi_B$.

$${}^O\mathbf{T}'_l = \mathbf{R}_x(\phi_l){}^O\mathbf{T}_r {}^r\mathbf{T}_l \quad (4.12)$$

where ϕ_l and ϕ_r are the torsion angles on \mathbf{X}_l and \mathbf{X}_r , as depicted in Fig. 4.1b.

Pose estimation

The state vector \mathbf{x} describes the needle status and is defined as follows:

$$\mathbf{x} = [x, y, \psi, \delta, k_1, \phi_A, \dot{\phi}_A, \ddot{\phi}_A, \phi_B, \dot{\phi}_B, \ddot{\phi}_B]^T \quad (4.13)$$

where the first 5 parameters come from (4.1). The torsion experienced by the two segments enters in the state vector by ϕ_A and ϕ_B . Torsion is assumed to have a second order dynamics: in the case study herein considered, the torsion affecting the sPBN changes during the insertion as a function of the current offset δ_t and can increase or reduce its speed according to the acceleration determined by variations in δ_t during the insertion.

The extended kinematic model, is defined as:

$$\mathbf{x}(k+1) = f(\mathbf{x}(k)) + b(\mathbf{u}(k+1)) + n(k+1) \quad (4.14)$$

where \mathbf{u} is the vector of inputs made of the cruise speed and the offset velocity:

$$\mathbf{u} = [v_1, v_2]^T. \quad (4.15)$$

The process noise $n(k)$ is assumed to be drawn from a zero-mean normal distribution $n(k) \sim \mathcal{N}(0, \mathbf{Q}_p)$ with variance \mathbf{Q}_p .

The function $f(\cdot)$ is defined as:

$$f(\mathbf{x}(k)) = \begin{bmatrix} \mathbf{I}_{[5 \times 5]} & & 0 \\ & \mathbf{A}_{[3 \times 3]} & \\ 0 & & \mathbf{A}_{[3 \times 3]} \end{bmatrix} \begin{bmatrix} x(k) \\ y(k) \\ \psi(k) \\ \delta(k) \\ k_1(k) \\ \phi_A(k) \\ \dot{\phi}_A(k) \\ \ddot{\phi}_A(k) \\ \phi_B(k) \\ \dot{\phi}_B(k) \\ \ddot{\phi}_B(k) \end{bmatrix} \quad (4.16)$$

where \mathbf{I} is the identity matrix and \mathbf{A} describes a second-order dynamics:

$$\mathbf{A} = \begin{bmatrix} 1 & \Delta t & \frac{1}{2}\Delta t^2 \\ 0 & 1 & \Delta t \\ 0 & 0 & 1 \end{bmatrix} \quad (4.17)$$

where Δt is the sampling time.

The control-input function $b(\cdot)$ is defined as:

$$b(\mathbf{u}(k+1)) = \begin{bmatrix} \cos(\psi(k))\Delta t & 0 \\ \sin(\psi(k))\Delta t & 0 \\ k_1(\delta(k) - \epsilon\psi(k))\Delta t & 0 \\ 0 & \Delta t \\ \vdots & \vdots \\ 0 & 0 \end{bmatrix}_{[11 \times 2]} \begin{bmatrix} v_1(k+1) \\ v_2(k+1) \end{bmatrix}. \quad (4.18)$$

The proposed method makes use of the 3 DoF position of the two segment tips. Such information can be obtained through embedded sensors, e.g. EM sensors, or via a suitable imaging modality, such as ultrasound. In case of sensors mounted on the segment tip, a further translation is included to link the sensor local frame to the segment tip, as in Fig. 4.1b. The sensor local frames, $\mathbf{X}_{A'}$ and $\mathbf{X}_{B'}$, result from the transformation ${}^O\mathbf{T}_{A'}$ and ${}^O\mathbf{T}_{B'}$, including translations $\Delta S_{x,y,z'}^A$, $\Delta S_{x,y,z}^B$ from the segment tip to the sensor positions. For the sake of simplicity, no rotation is assumed in ${}^O\mathbf{T}_{A'}$ and ${}^O\mathbf{T}_{B'}$. The observation at time k is expressed as:

$$y(k) = h(\mathbf{x}(k)) + v(k) \quad (4.19)$$

where the measurement function $h(\cdot)$ is a non-linear function defined as:

$$h(\mathbf{x}(t)) = [\mathbf{p}_A, \mathbf{p}_B]^T \quad (4.20)$$

where \mathbf{p} are the translation component of ${}^O\mathbf{T}_{A'}$ and ${}^O\mathbf{T}_{B'}$ and $v(k)$ the measurement noise. In this work, $v(k)$ represents the noise over the EM measurement, for which a zero-mean Gaussian nature is supposed, as in Navaei Lavasani et al., 2020, i.e. $v(k) \sim \mathcal{N}(0, \mathbf{Q}_m)$. Variance \mathbf{Q}_m is unknown a-priori and has to be guess in the filter calibration on the basis of the experimental data.

At each time step, the pose of the segment tips \mathbf{X}_A and \mathbf{X}_B can be computed from the parameters in the state vector \mathbf{x} through (4.11) and (4.12).

4.2.2 Four-segment PBN

Kinematic model

We consider the four-segment PBN as the combination of 2 two-segment needle systems. These two systems are positioned orthogonally so that the first, S_H , controls the horizontal steering in the xy plane and the second, S_V , the vertical steering in the xz plane, as shown in Fig. 4.2a. The needle is oriented as shown in the bottom-left part of Fig. 4.2b, corresponding to the configuration in Secoli and Rodriguez Y Baena, 2013 twisted of $\pi/4$ about the x axis. From Ko, Frasson, and Rodriguez Y Baena, 2011, the kinematic models of the two systems can be written as:

$$\begin{aligned}
 S_H : \begin{bmatrix} \dot{x}_H \\ \dot{y}_H \\ \dot{\psi} \\ \dot{\delta}_H \end{bmatrix} &= \begin{bmatrix} \cos(\psi) \\ \sin(\psi) \\ k(\delta_H - \epsilon\psi) \\ 0 \end{bmatrix} v_1 + \begin{bmatrix} 0 \\ 0 \\ 0 \\ 1 \end{bmatrix} v_{2,H} \\
 S_V : \begin{bmatrix} \dot{x}_V \\ \dot{z}_V \\ \dot{\theta} \\ \dot{\delta}_V \end{bmatrix} &= \begin{bmatrix} \cos(\theta) \\ -\sin(\theta) \\ k(\delta_V - \epsilon\theta) \\ 0 \end{bmatrix} v_1 + \begin{bmatrix} 0 \\ 0 \\ 0 \\ 1 \end{bmatrix} v_{2,V}
 \end{aligned} \tag{4.21}$$

Where x_H, y_H are the coordinates of the local frame $\mathbf{X}_{r,H}$ positioned on the tip of the rear segment of S_H . The variable ψ is the steering angle about the z axis that defines the curvature on the xy plane. This angle is determined by the offset δ_H between the two segments measured at the needle base. The same considerations apply for S_V , with x_V, z_V being the coordinates of the local frame $\mathbf{X}_{r,V}$ on the tip of the rear segment and θ being the steering angle about

the y axis, determined by δ_V . The coefficient k , estimated in Ko, Frasson, and Rodriguez Y Baena, 2011, links the offsets with the steering angle. To address the discrepancy between the offset shown at the needle base and the one at the tip due to the needle steering, the components $\epsilon\psi$ and $\epsilon\theta$ are included, with ϵ function of the needle radius (see Ko, Frasson, and Rodriguez Y Baena, 2011). The velocities v_1 and v_2 represent the cruise speed of the needle during the insertion and the rate of change in δ_H and δ_V . Velocities δ_H and δ_V define the radii of curvature R_H and R_V of the needle in the horizontal and vertical planes, two virtual plane that rotate together with the current configuration of the needle tip. R_H and R_V are expressed as:

$$\begin{aligned} R_H &= \frac{1}{k(\delta_H - \epsilon\psi)}, \\ R_V &= \frac{1}{k(\delta_V - \epsilon\theta)}. \end{aligned} \quad (4.22)$$

The position and orientation of the leading segments, $\mathbf{X}_{l,H}$ and $\mathbf{X}_{l,V}$, with respect to $\mathbf{X}_{r,H}$ and $\mathbf{X}_{r,V}$ are defined as:

$$\begin{aligned} {}^r\mathbf{T}_{l,H} &= \begin{bmatrix} & R_H \sin(\xi_H) & & \\ & \mathbf{R}_z(\xi_H) & R_H(1 - \cos(\xi_H)) & \\ & & 0 & \\ 0 & 0 & 0 & 1 \end{bmatrix}, \\ {}^r\mathbf{T}_{l,V} &= \begin{bmatrix} & R_V \sin(\xi_V) & & \\ & \mathbf{R}_y(\xi_V) & 0 & \\ & & -R_V(1 - \cos(\xi_V)) & \\ 0 & 0 & 0 & 1 \end{bmatrix} \end{aligned} \quad (4.23)$$

with \mathbf{R} representing a rotation about the specified axis and ξ_V , ξ_H the angles between $\mathbf{X}_{r,H}$ and $\mathbf{X}_{l,H}$ and between $\mathbf{X}_{r,V}$ and $\mathbf{X}_{l,V}$, respectively, as in Fig.

4.2a.

By merging the horizontal and vertical steering of S_H and S_V , the 4-segment needle model is obtained. A schematic representation is presented in Fig. 4.2b. The resulting kinematic model of the PBN is:

$$\begin{bmatrix} \dot{x} \\ \dot{y} \\ \dot{z} \\ \dot{\theta} \\ \dot{\psi} \\ \dot{\delta}_V \\ \dot{\delta}_H \end{bmatrix} = \begin{bmatrix} \cos(\theta)\cos(\psi) \\ \cos(\theta)\sin(\psi) \\ -\sin(\theta) \\ k(\delta_V - \epsilon\theta) \\ k(\delta_H - \epsilon\psi) \\ 0 \\ 0 \end{bmatrix} v_1 + \begin{bmatrix} 0 & 0 \\ \vdots & \vdots \\ 0 & 0 \\ 1 & 0 \\ 0 & 1 \end{bmatrix} \mathbf{v}_2. \quad (4.24)$$

Similarly to (4.21), x, y, z , represent the coordinates of the rear segment \mathbf{X}_r . In the case presented in Fig. 4.2b, $\mathbf{X}_r = \mathbf{X}_1$. The variables θ and ψ are the steering angles while δ_V and δ_H are the offsets between segments 1 and 3 for the vertical displacement and between segment 2 and 4 for the horizontal displacement. The correction factor ϵ is $\epsilon = 8r_n\sqrt{2}/(3\pi)$ for a four-segment needle, with r_n the needle radius. Given l_1, l_2, l_3, l_4 as the insertion lengths of the four segments, the vector of the offset velocities is:

$$\mathbf{v}_2 = \begin{bmatrix} \frac{d(l_1-l_3)}{dt} \\ \frac{d(l_2-l_4)}{dt} \end{bmatrix} \quad (4.25)$$

and the cruise speed v_1 is $v_1 = \frac{dl_r}{dt}$.

From (4.24), we define the pose of \mathbf{X}_r as:

$${}^O\mathbf{T}_r = \mathbf{P}(x, y, z)\mathbf{R}_z(\psi)\mathbf{R}_y(\theta) \quad (4.26)$$

where \mathbf{P} represents a pure translation.

We call $\delta_{t,i}$ the offset between the rear segment \mathbf{X}_r and the tip \mathbf{X}_i of segment i , $i \in 1, \dots, 4$, as in Fig.4.2b. The offset is defined as follows:

$$\delta_{t,i} = \begin{cases} l_i - l_r - \epsilon\theta, & \text{if } i = 1, 3 \wedge i \neq r \\ l_i - l_r - \epsilon\psi, & \text{if } i = 2, 4 \wedge i \neq r \\ 0, & \text{if } i = r \end{cases} \quad (4.27)$$

where the $\epsilon\theta$ and $\epsilon\psi$ are the offset corrections due to needle steering. Any variation in the length of the segments due to compression is considered negligible.

As in (4.23), for each segment i we define two angles (ξ_{V_i}, ξ_{H_i}) between \mathbf{X}_r and \mathbf{X}_i in the vertical and horizontal axes as:

$$\begin{aligned} \xi_{V_i} &= \delta_{t,i} / R_V \\ \xi_{H_i} &= \delta_{t,i} / R_H \end{aligned} \quad (4.28)$$

with R_V and R_H coming from (4.22). As in (4.23), the transformation ${}^r\mathbf{T}_i$ between \mathbf{X}_r and \mathbf{X}_i is:

$${}^r\mathbf{T}_i = \mathbf{P}(x_{r,i}, y_{r,i}, z_{r,i}) \mathbf{R}_z(\xi_{H_i}) \mathbf{R}_y(\xi_{V_i}) \quad (4.29)$$

where the translation components are:

$$\begin{aligned} x_{r,i} &= \max(R_H \sin(\xi_{H_i}), R_V \sin(\xi_{V_i})) \\ y_{r,i} &= R_H (1 - \cos(\xi_{H_i})) \\ z_{r,i} &= -R_V (1 - \cos(\xi_{V_i})). \end{aligned} \quad (4.30)$$

The transformation ${}^O\mathbf{T}_i$ between O and each \mathbf{X}_i is:

$${}^O\mathbf{T}_i = {}^O\mathbf{T}_r {}^r\mathbf{T}_i. \quad (4.31)$$

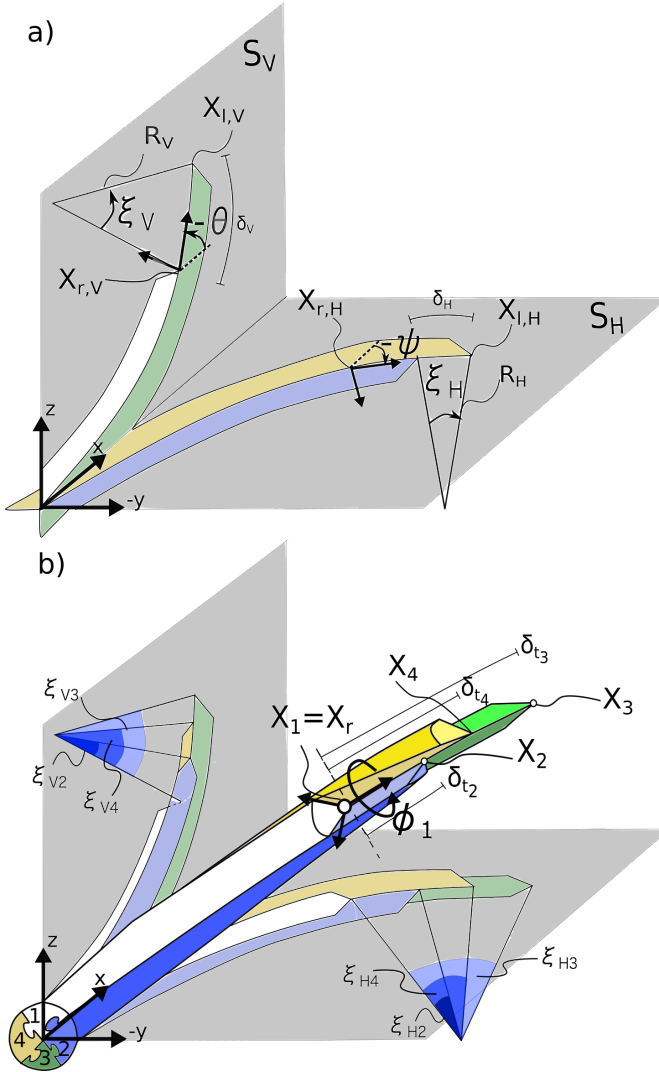


FIGURE 4.2: *Needle kinematics*: In a) the two 2D systems S_H and S_V are presented. The two segments composing S_H are in blue and yellow, while the two composing S_V are in green and white. The rear segments $X_{r,V}$ and $X_{r,H}$ as well as the leading segments $X_{l,V}$ and $X_{l,H}$ are shown. The two steering angles (ψ, θ) defined by δ_H and δ_V are plotted, together with the curvature radii and the angle ξ_V and ξ_H . The picture in b) shows the 3D representation of the four-segment PBN during insertion. All four segments are presented, identified by a unique number and color. The frames X_1, \dots, X_4 are shown. In this case, $X_r = X_1$. ψ_1 is the torsion affecting segment 1. The offsets δ_{t_i} at the level of the needle tip are presented (as $X_r = X_1$, $\delta_{t_1} = 0$). On the left and on the bottom of the picture, the respective ideal 2D projections are depicted on the xz and xy planes. The angles ξ_{v_i} and ξ_{h_i} can be identified in the figure. The projections refer to the needle without torsion, moreover, as $X_r = X_1$, $\xi_{v_1} = \xi_{h_1} = 0$.

Torsion model

In the same way as for the sPBN, for each segment i of the actual PBN embodiment, the tip pose becomes:

$${}^O\mathbf{T}'_i = \mathbf{R}_x(\phi_i){}^O\mathbf{T}_i. \quad (4.32)$$

Pose estimation

The state vector \mathbf{x} describes the needle status and is defined as follows:

$$\mathbf{x} = [x, y, z, \theta, \psi, \phi_1, \phi_2, \phi_3, \phi_4, \delta_v, \delta_h, \delta_{t_1}, \delta_{t_2}, \delta_{t_3}, \delta_{t_4}]^T \quad (4.33)$$

where the first 5 parameters come from (4.24), $\delta_{t_1, \dots, 4}$ from (4.27) and $\phi_1, \dots, 4$ express the torsion experienced by the four segments. The state at time k evolves according to:

$$\mathbf{x}(k+1) = f(\mathbf{x}(k)) + b(\mathbf{u}(k+1)) + n(k+1) \quad (4.34)$$

where \mathbf{u} is the vector of inputs, represented by the insertion and offset velocities:

$$\mathbf{u} = [v_1, l_1, l_2, l_3, l_4, l_r]^T \quad (4.35)$$

where $l_r = \min(l_1, l_2, l_3, l_4)$. The process noise $n(k)$ is assumed to be drawn from a zero-mean normal distribution $n(k) \sim \mathcal{N}(0, \mathbf{Q}_p)$ with variance \mathbf{Q}_p .

The update function $f(\cdot)$ is defined as:

$$\begin{aligned} f(\mathbf{x}(k)) = & [x(k), y(k), z(k), \theta(k), \psi(k), \phi_1(k), \phi_2(k), \phi_3(k), \\ & \phi_4(k), 0, 0, -\epsilon\theta(k), -\epsilon\psi(k), -\epsilon\theta(k), -\epsilon\psi(k)]^T. \end{aligned} \quad (4.36)$$

The control-input function $b(\cdot)$ is defined as:

$$b(\mathbf{u}(k+1)) = \begin{bmatrix} \cos(\theta(k))\cos(\psi(k))\Delta t \cdot v_1(k+1) \\ \cos(\theta(k))\sin(\psi(k))\Delta t \cdot v_1(k+1) \\ -\sin(\theta(k))\Delta t \cdot v_1(k+1) \\ k_1(\delta_v(k) - \epsilon\theta(k))\Delta t \cdot v_1(k+1) \\ k_1(\delta_h(k) - \epsilon\psi(k))\Delta t \cdot v_1(k+1) \\ 0 \\ \vdots \\ 0 \\ l_1(k+1) - l_3(k+1) \\ l_2(k+1) - l_4(k+1) \\ l_1(k+1) - l_r(k+1) \\ l_2(k+1) - l_r(k+1) \\ l_3(k+1) - l_r(k+1) \\ l_4(k+1) - l_r(k+1) \end{bmatrix} \quad (4.37)$$

where Δt is the sampling time.

The measurements are given by embedded sensors, e.g. electromagnetic sensors, or via a suitable imaging modality. The observation at time k is expressed as:

$$y(k) = h(\mathbf{x}(k)) + v(k) \quad (4.38)$$

where the measurement function $h(\cdot)$ is the results of a non-linear function defined as:

$$h(\mathbf{x}(t)) = [\mathbf{p}_1, \mathbf{p}_2, \mathbf{p}_3, \mathbf{p}_4]^T \quad (4.39)$$

with \mathbf{p}_i is the translation component of ${}^O\mathbf{T}'_i$ from (4.32). representing the x ,

y, z coordinates retrieved by the four sensors located in the needle segments. The measurement noise $v(k)$ is supposed to be a zero-mean Gaussian noise $v(k) \sim \mathcal{N}(0, \mathbf{Q}_m)$ with variance \mathbf{Q}_m .

4.3 Experimental Protocol

4.3.1 Two-segment PBN (sPBN)

Simulation study

The EKF has been tested over a set of simulated insertions. These tests aimed at evaluating the accuracy of our pose estimation method with respect to the noise on the measurement data in order to determine the maximum level of noise that still guarantees acceptable estimation performance. This is done by artificially adding a measurement noise in the simulated data.

A set composed of four variable offset velocities (v_2), whose trend is shown in Fig. 4.3a, was used in the 2D kinematic model described in Section 4.2.1 to generate four simulated needle insertions.

Two 3 DoF position sensors were ideally mounted on the segment tips, located at a known distance ($\Delta S_{x,y,z}^A, \Delta S_{x,y,z}^B$) with respect to the tip reference frames ($\mathbf{X}_A, \mathbf{X}_B$). The insertions feature different values of k_1 , used to obtain different steering responses. These dimensions and parameters are presented in Tab. 4.1.

To mimic the torsion of the needle during the insertion, at every time step a rotation ϕ about the needle insertion axis is simulated to both needle segments.

We simulated ϕ on the leading segment with the following function:

$$\phi_l(t) = \begin{cases} \phi_l(t-1) + \Delta\phi(\delta_t(t)) & \text{if } |\phi_l(t-1)| < \phi_{max} \\ \phi_l(t-1) + \Delta\phi(\delta_t(t))e^{-d|\phi_l(t-1)-\phi_{max}|} & \text{if } |\phi_l(t-1)| \geq \phi_{max} \end{cases} \quad (4.40)$$

Needle				EKF				Noise (σ [mm])				
R_n [mm]	ΔS^A [mm]		ΔS^B [mm]	Q_p	Q_m [mm]		σ_1	σ_2	σ_3	σ_4		
1	-1	-1	0	-1	1	0	10^{-9}	1	0.07	0.14	0.21	0.28
\mathbf{k}_1 [mm $^{-2}$]				Torsion function				Setup				
$k_{1,1}$	$k_{1,2}$	$k_{1,3}$	$k_{1,4}$	a	b	c	d	ϕ_{max}	v_1	L_i	f	
				[deg]				[deg]	[mm/s]	[mm]	[Hz]	

TABLE 4.1: Parameters and dimensions used in the simulation trials.

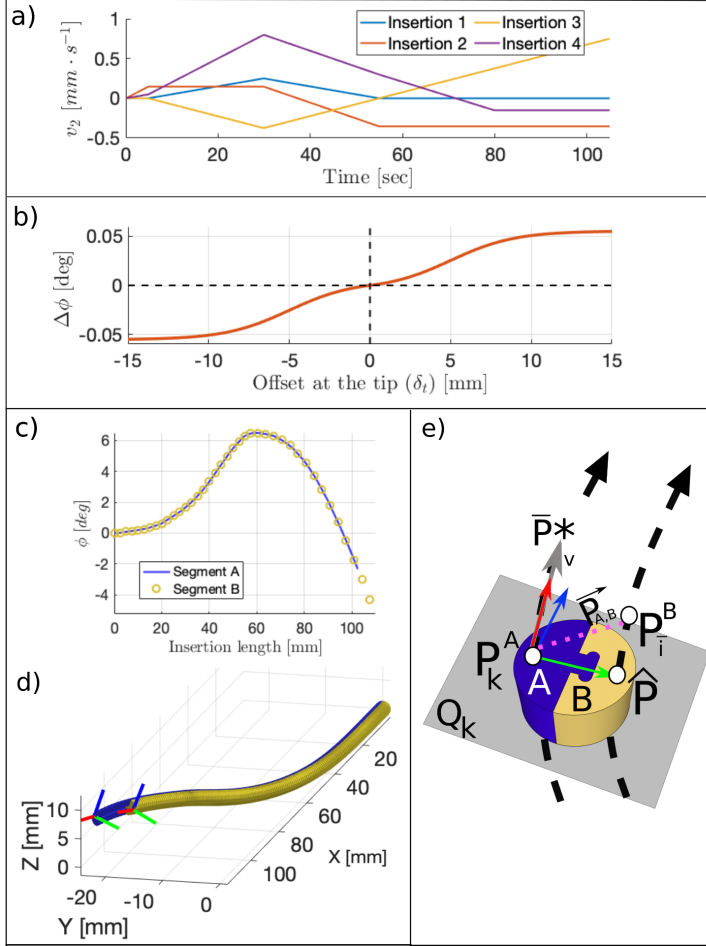


FIGURE 4.3: In a) the evolution of the offset velocities (v_2) for the four simulated insertions is shown over time. In b), the incremental step of needle rotation is shown with respect to the offset at the tip. In c), the trend of ϕ for one simulated insertion is depicted over the insertion length for segment A and B. In d), the resulting 3D reconstruction of the needle shape. In d), a schematic of the main entities coming into play in the geometric approach is presented. In e), a representation of the geometric approach discussed in Section 4.3.1 is shown.

where $\Delta\phi$ represents the incremental step of rotation affecting the leading segment. ϕ_{max} is a maximum angle of needle torsion after which we assumed the needle torsional compliance decreases. This limits further rotations and is simulated by the exponential decay that multiplies $\Delta\phi$ in the second case of (4.40).

$\Delta\phi$ is defined as follows:

$$\Delta\phi(\delta_t) = \text{sgn}(\delta_t) \cdot \left[\frac{a}{1 + e^{(-b(\delta_t - c))}} - \frac{a}{1 + e^{bc}} \right] \quad (4.41)$$

we assumed $\Delta\phi$ having a quasi-linear behaviour. Values of δ_t near to zero induce a slow increase in the rotation angle; the slope of $\Delta\phi$ rises for larger values of δ_t up to $|\delta_t| \geq 15$ mm, where the incremental step of rotation becomes constant. The second addendum in (4.41) is required to have $\Delta\phi(0) = 0$ deg. The slope $\Delta\phi$ is symmetrical about the y axis, thus positive values of δ_t drive the needle to twist toward positive values of ϕ and vice-versa. Such a behaviour, designed for the scope of simulation and presented in Fig.4.3b, represents an assumption based on experimental evidence (Watts, Secoli, and Baena, 2019). Parameters of (4.40) and (4.41), presented in Tab. 4.1, have been defined empirically on the basis of the expected needle behaviour and the experimental evidence.

We hypothesised a follow-the-leader condition for which, at a specific insertion length l , the rear segment features an angle of torsion ϕ_r equal to the one shown earlier by the leading segment at the same insertion length, i.e. $\phi_r(l) = \phi_l(l)$.

In Fig.4.3c, the torsion angle featured by segments A and B in one of the simulated insertions is presented. The resulting needle shape is shown by the 3D reconstructions in Fig. 4.3d.

White noise with different levels of standard deviation (σ) were added on the different simulations. As the lower value of noise, $\sigma_1 = 0.07$ mm measured in-gel during a static EM acquisition is considered (EM sensors: 5 DoF, 0.3 mm diameter, AuroraTM, NDI[®], Waterloo, Ontario, Canada). As performance metrics for needle position estimation, the Euclidean error (E_t) between the true segment position and the estimated one is used. The orientation error

(E_r) is computed individually for each Euler angle as the absolute error between the true angle and the estimated one. We consider as acceptance criteria $E_t < 1$ mm and $E_r < 5$ deg, comparable with state of the art (Kallem and Cowan, 2009; Ralovich et al., 2014). With these criteria, an upper bound σ_4 was defined and it is reported in Tab. 4.1 along with two intermediate steps σ_2 and σ_3 included in the test to evaluate the performance of the solution at different levels of measurement noise. The EKF has been tested three times over each insertion and each level of σ . In simulations, Q_m was chosen empirically by tuning the nominal accuracy of the EM sensors used in in-gelatin experiments to the value that guarantees the best estimation performance. Similarly, Q_p was chosen as $Q_p = 10^{-j}$ in the set $j \in [0, \dots, 10]$ as the value that provides the best prediction accuracy. The values of Q_m , Q_p , the insertion speed (v_1), the insertion length (L_i), the sample rate (f) and further simulation parameters are presented in Tab. 4.1.

Tests were performed using MATLAB® R2019a, on a MacBook Pro (MacOS 10.14.6, 2,7 GHz Intel Core i5, 8 GB of RAM).

Geometric approach for pose estimation

A geometric approach is used as a term of comparison for the proposed EKF solution. This method, run offline, relies only on geometric relationships to compute the pose of segment A and B and consists in the definition of a cross-plane Q_k at each time step, as shown in Fig. 4.3e. In the following, the description of the method for defining the pose of segment A at time k and point P_k^A is presented.

At first, the insertion direction, \mathbf{v} , is defined by finding the point \bar{P} as the average of the $n=25$ future insertion points with respect to k :

$$\bar{P} = \frac{1}{n} \sum_{i=1}^n (P_{k+i}^A) \quad (4.42)$$

$$\mathbf{v} = \frac{\bar{P} - P_k^A}{|\bar{P} - P_k^A|}. \quad (4.43)$$

For a sampling frequency of 2 Hz and a cruise speed $v_1 = 1 \text{ mm} \cdot \text{sec}^{-1}$, $n=25$ corresponds to 12.5 secs of acquisition and 12.5 mm of needle insertion.

The plane Q_k is defined as follows:

$$a(x - P_{k,x}^A) + b(y - P_{k,y}^A) + c(z - P_{k,z}^A) = 0 \quad (4.44)$$

where $a = \mathbf{v}_x$; $b = \mathbf{v}_y$; $c = \mathbf{v}_z$.

From the EM data of segment B, the closest point P_i^B to Q_k is found, where \bar{i} is such that:

$$\bar{i} = \operatorname{argmin}(\overrightarrow{P^{A,B}} \cdot P_k^A) \quad \forall i \in [0, k_{end}] \quad (4.45)$$

where k_{end} is the last sample of the EM acquisition and

$$\overrightarrow{P^{A,B}} = P_i^B - P_k^A. \quad (4.46)$$

The projection \hat{P} of P_i^B on Q_k is computed and the reference frame at P_k^A is obtained as:

$$\mathbf{x} = \frac{\mathbf{v}}{|\mathbf{v}|}; \quad \mathbf{y} = \frac{\hat{P} - P_k^A}{|\hat{P} - P_k^A|}; \quad \mathbf{z} = \mathbf{x} \times \mathbf{y}. \quad (4.47)$$

The performance of the geometric method has been evaluated in simulation over different levels of noise σ . As this set includes the noise measured in gelatin during static EM acquisitions (σ_1), the test aims at demonstrating the suitability of the method to be used as way to compare phantom-brain gelatin experiments.

Similarly to the EKF, the geometric approach has been tested three times for each simulated insertion and noise level.

In-gel experiments

Three needle insertions were performed on phantom-brain gelatin (10% by weight bovine gelatin - Chef William Powdered Gelatin) to assess the performance of the proposed solution in conditions which replicate real insertion scenarios.

In-gel trials were performed using a four-segment PBN design, whose details can be found in Watts, Secoli, and Baena, 2019. The PBN is formed by four

segments featuring one lumens of 0.3 mm each, with a needle of an overall outer diameter of 2.5 mm. To reproduce the sPBN model, the four segments were coupled two by two. We can thus define two couples of segments, cpl_A and cpl_B , with the first controlling the left steering and the second controlling the right steering. In such a way, we transform defacto the four-segment PBN design into a two-segment design with cpl_A and cpl_B representing segment A and segment B.

The EKF requires the tip position of segment A and B as measurement data. This is obtained by accommodating an EM AuroraTM sensor (5 DoF, 0.3 mm diameter, Northern Digital inc.) inside a lumen of cpl_A and a lumen of cpl_B . Only the 3 DoF position of each segment was used as measurement input in the proposed method. This approach was chosen to make the solution feasible also for applications where the orientation cannot be measured. As for simulation trials, Q_p and Q_m were set through a tuning process to values that provided the best prediction results, namely $Q_p = 1 \cdot 10^{-3}$ and $Q_m = 1 \text{ mm}^2$. The experimental setup is presented in Fig. 4.4 and described hereinafter. The insertion of the needle was driven by a robotic system composed of four linear actuators (one per each PBN segment, linear pitch 1mm/rev). Each segment of the needle is linked to the linear actuator by a flexible transmission made of a nitinol wire. Per each segment, a rotational encoder at the motor (Maxon motor DC16XS - Res 1200 pulse/rev) assures the precision motion of each segment. The needle is inserted for 20mm in the gelatin with all four segments aligned, then the desired offset is generated by pushing a couple of adjacent segments ahead (e.g. cpl_A if $\delta > 0$). The needle is then inserted at a constant cruise speed of $1 \text{ mm} \cdot \text{sec}^{-1}$ as in previous studies (Ko, Frasson, and Rodriguez Y Baena, 2011; Watts, Secoli, and Baena, 2019), resembling the speed of manual insertion of a standard deep brain stimulation electrode performed by an expert neurosurgeon. Encoders record the insertion length of the segments, from which the cruise speed v_1 and the offset velocity v_2 can be computed. A sample rate of 2 Hz was used, which was assumed as appropriate, considering the low magnitude of v_1 . A desktop PC with Linux Ubuntu 16.04 operating system running the Robotic Operating System (ROS) was used to control the needle insertion and for data storage.



FIGURE 4.4: *Experimental setup*: the PBN is inserted into gelatin and tracked by the EM field generator through the EM sensors mounted on the needle. An actuation box controls each segment of the PBN and encoders measure their insertion length. On the bottom left, a magnification of the needle insertion.

4.3.2 Four-segment PBN

In-gel experiments

As for the sPBN, 3 needle insertions were performed in a 10% by weight bovine gelatin (Chef William Powdered Gelatin) using a medical-grade, 2.5 mm outer diameter PBN (Watts, Secoli, and Baena, 2019).

The PBN working channels were used to embed 4 EM AuroraTM sensors (5 DoF, 0.3mm diameter, Northern Digital inc.). Only the 3 DoF sensor positions have been used as measurement data but, differently from the in-gel experiments conducted on the sPBN (4.3.1), the position of each PBN segment is considered individually.

The process variance (Q_p) and the measurement noise variance (Q_m), have been set as the ones that provide the best prediction results, namely $Q_p = 1 \cdot 10^{-2}$ and $Q_m = 1 \text{ mm}^2$.

The insertion of the needle was driven by a robotic system. Details about the robotic insertion setup are presented in 4.3.1.

Geometric approach for pose estimation

The estimated needle position was compared with the EM measurement in terms of RMSE to verify the filter accuracy. As no orientation data is used, a geometric approach is exploited to compute the orientation of the needle and as term of comparison for the EKF.

The geometric approach used for PBN validation differs from the one used for the sPBN validation. For each time step, a plane orthogonal to the insertion axis is defined. A centerline point is computed by averaging the position of the 4 points corresponding to the intersection of the EM traces with the plane. The local frame is centered on the centerline point. The x axis is defined as the needle insertion direction and the y and z axes are defined along the conjunctions between the origin of the local frame and the intersection points between the trace of sensor 4 and 1 with the orthogonal plane.

4.4 Results

4.4.1 Two-segment PBN (sPBN)

Simulation study

The results of simulated trajectories at the different levels of measurement noise are presented in Fig. 4.5 for the EKF and the geometric approach. As no significant difference has been detected from segments A and B and from different simulated insertion profiles, results have been combined. In the top row, the Euclidean error (E_t) with respect to the reference trajectory is presented for both the estimation methods. This shows a positive linear trend over the increasing of σ still maintaining the position error far lower than the 1 mm margin of acceptability.

The orientation errors (E_r) are presented in the rows below. As a yardstick, the 5 deg error considered to be acceptable is shown in the graphs, except for θ and ψ in the EKF results, where it was omitted to improve readability, as E_r was found to be particularly small.

For the EKF, the ϕ angle shows the largest error. The 5 deg yardstick is reached for a measurement noise (σ_4) equal to four times the one evidenced in static in-gelatin EM acquisitions (σ_1). This value can be considered the upper bound accuracy for a tracking system to be used with the presented solution.

The geometrical approach guarantees $E_t < 1$ mm and $E_r < 5$ deg for the level of noise σ_1 , which is the one evidenced in-gel during static EM measurements, confirming the feasibility of the method to be used as comparison for the experiments in gelatin.

In-gel experiments

In Tab. 4.2, the results in terms of E_t and E_r from the 3 in-gel insertions are presented as the 25th, 50th, 75th quantiles.

The results from one of the three sPBN insertions in gelatin are shown in Fig. 4.6 (Trial 1 in Tab. 4.2). On the top, the original position data retrieved by the two EM sensors embedded in the PBN are presented, along with the needle

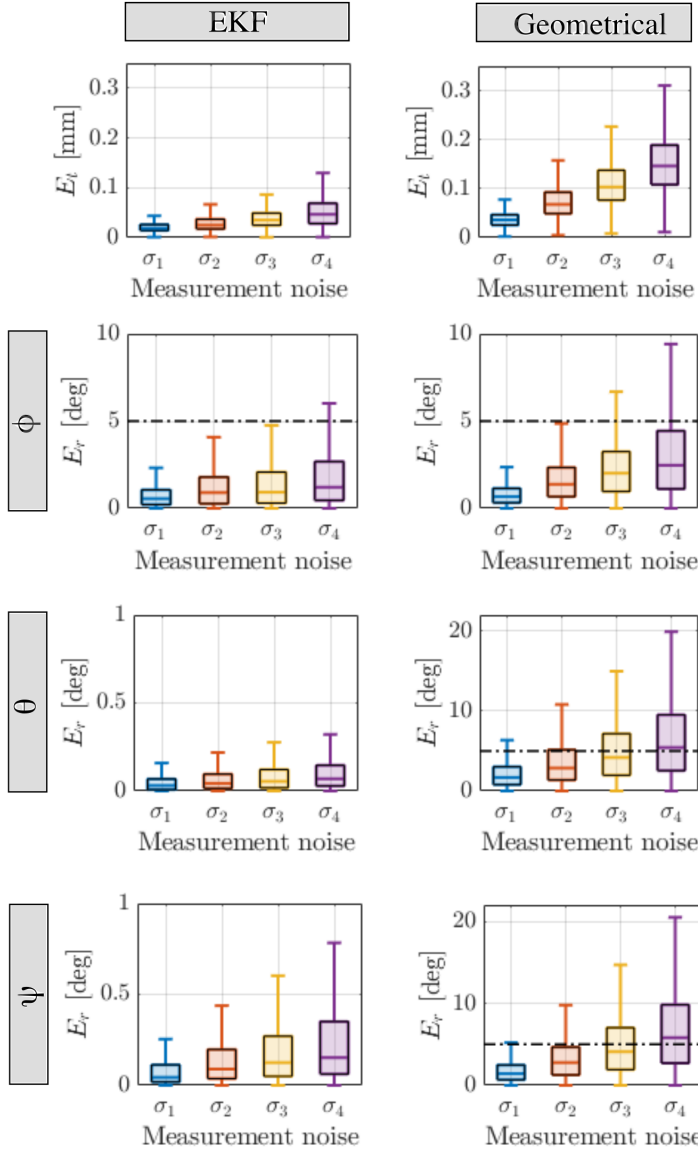


FIGURE 4.5: *Simulation results*: the graphs show the Euclidean and orientation errors (E_t, E_r) from the simulation trials at different values of noise σ . Results from the EKF and the geometrical approach are shown respectively in the left and right columns. As a yardstick, the 5 deg error tolerance is plotted, with the exception of the θ and ψ angles of the EKF where E_r is too small. Please note that the span of the y axis is different between the two methods for the θ and ψ angles.

	E_r [mm]			$E_{r,\phi}$ [deg]			$E_{r,\theta}$ [deg]			$E_{r,\psi}$ [deg]		
	25 th	50 th	75 th	25 th	50 th	75 th	25 th	50 th	75 th	25 th	50 th	75 th
Trial 1	0.16	0.29	0.46	0.63	1.40	2.57	1.98	2.66	3.33	0.37	0.98	1.97
Trial 2	0.11	0.23	0.39	1.98	2.77	4.74	0.69	1.41	2.21	0.79	1.52	2.22
Trial 3	0.32	0.40	0.47	2.71	3.71	4.90	0.27	0.43	0.76	0.53	1.11	1.44

TABLE 4.2: Results from the in-gel trials. Position error E_r is computed with respect to the original EM data. Orientation error E_r is computed with respect to the orientation measured by geometric approach, considered as gold standard. For each index of performance, the 25th, 50th, 75th quantiles are presented.

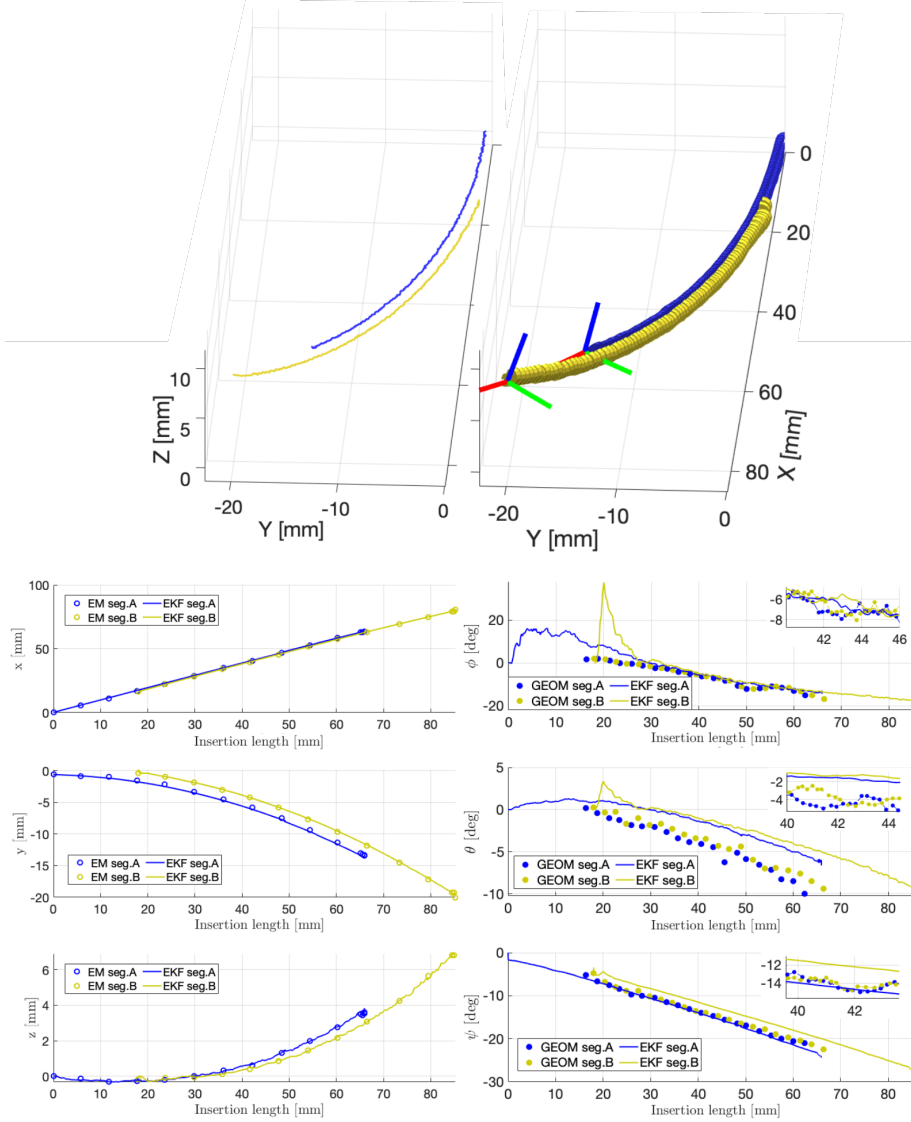


FIGURE 4.6: *In-gel results*: on the top, the original position data from the EM sensors are shown for Trial 1, along with the needle reconstruction obtained from the EKF pose estimation. In the graphs below, on the left side the comparison between the original EM position and the one estimated by the EKF is presented. The graphs on the right, instead, allow to compare the estimated orientation with respect to the one calculated by the geometric approach, considered as gold standard. A close look at the angles estimated by the two methods is possible through the three magnification windows.

reconstruction obtained from the EKF pose estimation. From the graphs below, it is possible to compare the estimated position with respect to the values from the EM sensors and the estimated orientation with respect to the geometric approach, used as gold standard. In the graphs, the EM data and the geometric results have been under-sampled respectively by a factor 25 and 15 to improve the readability of the results. From the magnification windows in Fig. 4.6, a close look to the Euler angles estimated by two methods over the insertion length is possible.

EKF results show an initial phase of orientation convergence, particularly evident for the roll angle. This phase is measured as the insertion length required to stabilize the needle within the 5 deg error margin with respect to the angles provided by the geometric approach, neglecting the initial insertion offset between segments. In Fig. 4.6, the convergence phase for Trial 1 can be measured on segment B as equal to 8 mm. The convergence phases measured for Trial 2 and Trial 3 are 7.5 mm and 10 mm, respectively. The convergence phase is overlooked in the computation of the position and orientation errors of Tab. 4.2.

4.4.2 Four-segment PBN

In-gel experiments

The results from the 3 insertions in gelatin are presented in the graphs of Fig. 4.7.

In the left part of the figure, the original position measurements from the 4 EM sensors are shown along with the reconstruction of the needle obtained from the EKF position and orientation estimation. The CAD model used for the reconstruction of the needle shaft is shown on the top-left corner of Fig. 4.7, along with its local reference frames. The reconstruction is performed step-wise, i.e. at every time step a new portion of the needle shaft is added to each segment in accordance to the position and orientation estimated by the EKF. In the right part of the figure, the graphs report the resulting position and orientation for each insertion over time. A comparison between the measured and estimated position is possible by looking at the graphs in the left column where the x - y - z coordinates are plotted for each segment over time. For the

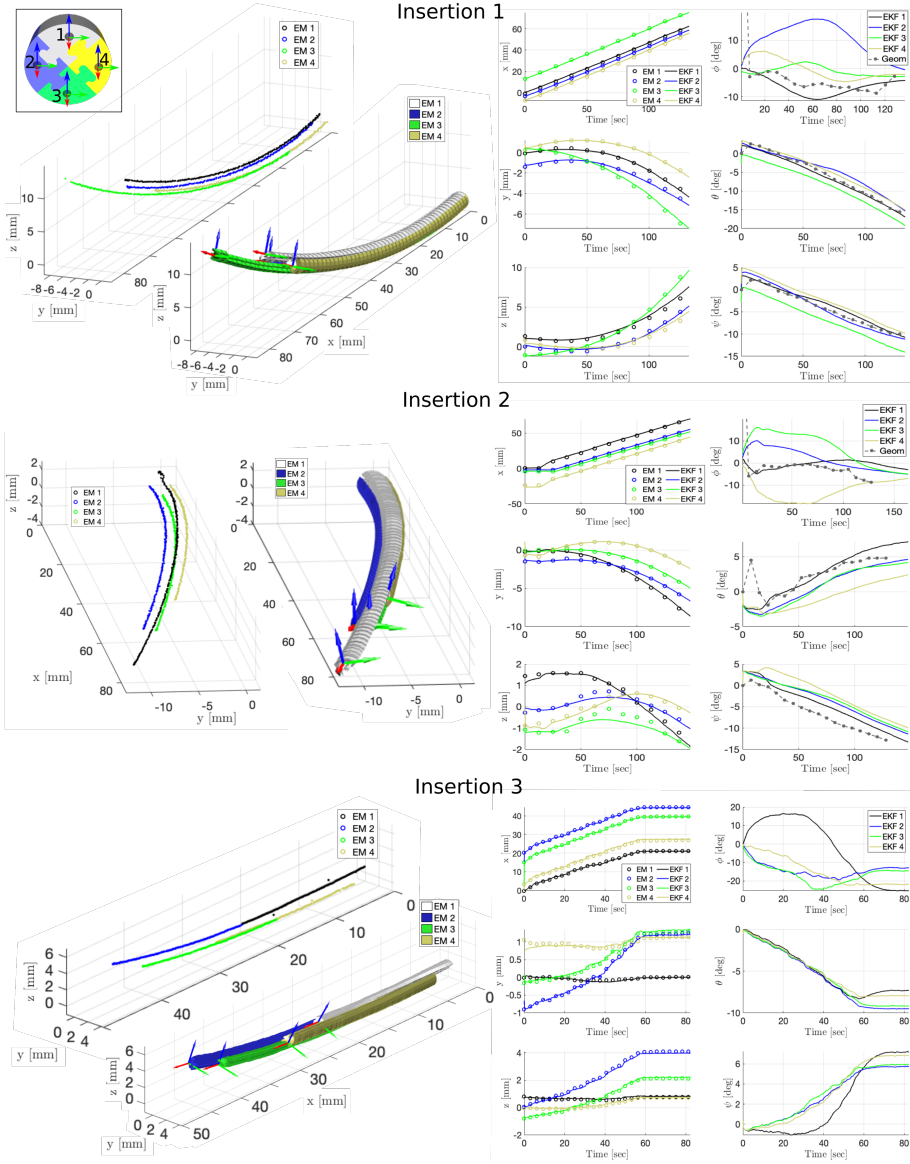


FIGURE 4.7: *In-gel results:* In the figure, the results from 3 PBN insertions in gelatin are presented. In the left part, the raw position measurements from the 4 EM sensors are plotted. Nearby, the reconstructions of the needle obtained from the position and orientation estimated by the EKF are presented. In the top-left corner, the CAD model used for the reconstruction is shown. On the right, the graphs report the estimated position and orientation for each insertion along with the original EM data and the orientation resulting from the geometric pose computation

sake of readability, the EM measurement data are presented under-sampled by a factor 20.

In the right column, the roll, pitch and yaw angles (ϕ, θ, ψ) are presented. For insertion 1 and 2, the comparison with the geometrical pose reconstruction method is possible by comparing the estimated segment orientation with the one calculated geometrically at the centerline. The lack of data in insertion 3 and in the last part of insertion 1 and 2 is due to the impossibility to define the geometrical pose when the 4 segments are not completely paired side by side, and thus the computation of the needle centerline is not possible.

4.5 Discussions

4.5.1 Two-segment PBN (sPBN)

Simulation trials on the EKF demonstrate less accurate estimation of the roll with respect to the other orientation angles. In the EKF, the roll and its derivatives are unreachable states. For these states, the initial prediction based on model inputs is not possible and, for their estimation, the EKF relies solely on the noisy measurement data, which leads to a higher estimation error. In gelatin, where modeling inaccuracies come into play, the error in pitch and yaw angles becomes similar to the one in the roll.

Compared to the EKF, a faster worsening in pose reconstruction accuracy was evidenced in simulation for the geometric approach over the raise of the measurement noise. Indeed, by filtering the measurement data with the state prediction provided by the needle kinematic model, the EKF can increase the robustness of the estimation in the presence of measurement noise. In addition, the main drawback of the geometric approach consists of the impossibility to compute the needle pose in the parts of the insertion where the needle cross-plane cannot be defined, i.e. in the offset between segments. In the in-gelatin trial shown in Fig. 4.7, this is represented by the final part of the insertion of segment B, which is the leading segment that defines the steering direction and the pose of which is essential for the sake of needle control. This drawback prevents the geometric approach from being used as a means for pose

estimation in real insertion scenarios.

The soundness of the proposed solution is confirmed by the EKF performance in gelatin. A significantly lower position error is achieved with respect to the tracking methods proposed by Khan *et al.* Khan *et al.*, 2019 and Vrooijink *et al.* Vrooijink, Abayazid, and Misra, 2013 (~30% reduction in the mean position error). Relative to the latter, a comparable orientation error is achieved, even though in Vrooijink *et al.* the roll angle was overlooked.

4.5.2 Four-segment PBN

Results obtained in the 3 insertions in gelatin demonstrated the ability of the filter to follow the position tracked by the EM sensors and estimate the full pose of each segment of the PBN needle.

The filter demonstrated a fast convergence in position tracking for all segments and in all the 3 insertions. The Root Mean Square Error (RMSE) calculated over the x, y, z position between the estimated segment tip position and the one measured by the EM sensors results $RMSE_{xyz} = (0.57 \text{ mm}, 0.04 \text{ mm}, 0.07 \text{ mm})$.

With regard to the orientation, fast convergence can be noticed for the pitch (θ) and yaw (ψ) angles. The accuracy of the estimation of pitch and yaw angles can be appreciated by comparing the data with the geometric approach and by looking at the CAD reconstructions. It is worth emphasising that, as the geometric approach computes a unique frame on the needle centerline, a one-to-one comparison with each specific needle segment is not possible and no RMSE has been computed for the orientation. The trends followed by the roll angles (ϕ) are less easy to evaluate as a longer time for convergence is needed. For insertions 1 and 2, the comparison with the geometric approach suggests a correct estimation of the roll angle.

For insertion 3, the fact that the segments are never fully paired makes impossible to use the geometric pose computation method. Still, despite the initial rise, at the end of the insertion the roll angle of segment 1 decreases to values similar to the ones of segments 2 and 3 at the start of the insertion. This suggests that, for the same insertion depth, the segments show the same level of

torsion.

The comparison among the roll angles exhibited in the 3 different insertions is not straightforward. In insertion 1, the PBN performs a deeper insertion in the gelatin with respect to insertion 3, also achieving a larger steering, as evidenced by the higher displacement in the Cartesian axes. Nonetheless, the roll angles exhibited by the PBN segments at the end of insertion 1 are confined within few positive angles with respect to the roll angles in insertion 3, which are in the range between -10 deg and -23 deg. This can be explained by the different configurations featured by the needle that determines a larger or a smaller torsion effect on the needle shaft according to the specific case. In fact, in insertion 1, the needle takes an helical shape, which may promote larger torsion with respect to other configurations. This evidence, along with the magnitude of the roll angles estimated experimentally, contradict the assumption of infinite torsional stiffness for the PBN and validate the importance of a solution able to estimate the full pose of the needle during the insertion.

4.6 Conclusion and future developments

In percutaneous intervention, the ability to track the needle position and orientation (i.e. the full pose) is of paramount importance for a robotic steering system to perform an accurate needle insertion and address needle torsion. The method presented in this chapter aims at investigating **Hypothesis 2** by proposing a solution for the on-line estimation of the full pose of a multi-segment needle, including the rotation of the needle tip about its insertion axis, i.e. the roll angle. The solution, based on an EKF, uses the position measurement of the needle tip to correct the needle state prediction obtained from a kinematic model and to infer the roll angle. In this chapter, we address **Hypothesis 2.1** and **Hypothesis 2.2** by evaluating our solution on a simplified, two-segment PBN (sPBN) and a four-segment PBN, which accommodate a sensor for position tracking on the tip of each segment.

The method has been tested on the sPBN in simulation over different insertion trajectories and levels of measurement noise to assess the performance, demonstrating reliability in terms of estimation accuracy and robustness against

measurement noise. In experiments conducted in gel, the solution showed to be able to estimate the needle pose for the entire length of the insertion with a position error < 1 mm and an orientation error < 5 deg, consistent with the state of the art. When tested in gel on the four-segment PBN, the solution demonstrated its feasibility in estimating the position of the tips of each segment (RMSE < 0.6 mm) and in estimating the needle orientation when tested against a bespoke geometric approach, even though long time of convergence was evidenced for the torsion angle. The pose estimated by the filter could thus be safely used by a control system to drive the needle insertion and address potential needle torsion.

In this work, to make the proposed solution suitable for applications where only the needle position can be tracked (e.g. where tracking is performed via X-ray fluoroscopy or US), only the 3 DoF position of the needle segment tips is considered as tracking data from the 5 DoF EM sensors. Benefits in terms of estimation performance arising from the inclusion of pitch and yaw angles from the 5 DoF EM sensors as measurement data will be the object of forthcoming investigations. Future studies will focus also on improvements derived from the use of different filtering approaches, as the Unscented KF and particle filters. Additionally, an adaptation to other types of steerable needles will also be evaluated. A possible candidate is the bevel-tip needle with base rotation, the kinematic model of which is presented in Kallem and Cowan, 2009. The needle tip position could be tracked and, similarly to the method herein presented, a state variable representing the torsional mismatch between the tip and the base of the needle could be included in the EKF to correct the needle pose estimation.

Chapter 5

Conclusions

Path planners for steerable needles in 3D focus either on a fast computation or on path optimality. A quick planning allows the intra-operative adjustment of the plan in case insertion errors arise because of uncertainties in needle motion or variations in the environment (e.g. deformations, obstacles and target movements) at the expense of a sub-optimal planning. In the second case, path optimality can be found but the time needed for its computation is unbearable in case of 3D environments.

Some types of steerable needles show the onset of frictional and shear forces that determine an unwanted torsion of the needle. This results in a discrepancy in terms of angle of rotation along the insertion axis between the needle tip and the needle base. Only if the control system is aware of this discrepancy it can counteract to keep the needle on the correct insertion path. Unfortunately, imaging techniques and electromagnetic tracking cannot sense the needle torsion and, currently, no solution exists for pose estimation of multi-segment steerable needles.

In this PhD dissertation, a pre-operative curvilinear path planner for steerable needles is presented. The algorithm can find optimized paths coping with the needle kinematics and the complexity of a neurosurgical working scenario with a computational time consistent with standard pre-operative path planners. A solution for estimating the full pose of a multi-segment steerable needle based on partial tracking information is also proposed.

The solutions were developed and tested considering the Programmable Bevel-tip Needle (PBN) as case study. The latter consists of a multi-segment steerable

needle under development within the EU EDEN2020 project and designed for percutaneous intervention in neurosurgery (drug infusion and in-situ optical diagnosis).

In Chapter 2, the planning problem (**Hypothesis 1**) is contextualized with a review of the sampling-based methods proposed in the literature for the computation of curvilinear paths. In Chapter 3, a new pre-operative planner for optimized paths computation is proposed. The solution is validated through simulated insertions in neurosurgical scenarios demonstrating improvements in terms of path length and obstacle avoidance with respect to the state of the art (**Hypothesis 1.1**) as well as a computational time suitable for pre-operative planning (**Hypothesis 1.2**). Chapter 4 addresses the problem of pose estimation for a multi-segment needle (**Hypothesis 2**) by providing a solution based on a Extended Kalman Filter and data from position sensors. The method was tested on a two-segment (**Hypothesis 2.1**) and on a four-segment (**Hypothesis 2.2**) PBN through simulation and in-gel experiments.

5.0.1 Thesis contribution

The PhD research created:

- *A new curvilinear path planner able to compute, in a time consistent with standard pre-operative path planners, a kinematically feasible path for a steerable needle in accordance with the optimization criteria of minimum path length and maximum distance from obstacles.*

The majority of the path-planning solutions focus either on a fast computation or on path optimization with respect to specific criteria. Additionally, solutions from the literature are often validated in scenarios that do not catch the complexity of a real human anatomy (Duindam et al., 2010; Patil and Alterovitz, 2010; Torres and Alterovitz, 2011). A pre-operative curvilinear path planner for steerable needles is presented able to keep the computational time consistent with standard pre-operative planning guaranteeing the quasi-optimality of the computed path. This

is obtained by confining the search within the region of reachability of the needle built upon its kinematic limits and performing an evolutionary optimization procedure resulting in larger obstacle avoidance and shorter path length with respect to solutions from literature. Additionally, a higher success rate in finding a path has been evidenced using the presented method, which was validated through simulated insertions in a real neurosurgical scenario.

- *A solution for the on-line full pose estimation of a multi-segment steerable needle using position sensors mounted on the needle tip and applicable to a two-segment and four-segment PBN.*

Percutaneous needles can be affected by torsion due to the frictional and shear forces exerted between the needle and the tissue. The possibility to track this torsion would allow the control system to correct its command allowing the needle to perform a correct insertion. The resolution of standard imaging techniques does not allow the visualization of needle rotation about the insertion axis and electromagnetic systems do not feature 6 DoF sensors small enough to be mounted on the thin steerable needles.

A solution for the accurate pose estimation of a multi-segment needle on the basis of the available tracking data and a kinematic model is proposed. The method, based on an Extended Kalman Filter, uses the position measurement of the needle segment tips retrieved through electromagnetic sensors to correct the needle state prediction obtained from a kinematic model and infer the needle roll angle about its insertion axis. The method was developed initially for a simplified, two-segment PBN in simulation and in phantom-brain gelatine demonstrating reliability in terms of estimation accuracy and robustness. In experiments conducted in gel, the solution showed to be able to estimate the needle pose for the entire length of the insertion with position and orientation errors consistent with the state of the art.

The solution was later extended to a four-segment PBN design and tested in gelatine. Results demonstrated the feasibility of the proposed method

for estimating the position and the orientation of the needle segment tips, although a long time of convergence was evidenced for the torsion angle.

5.0.2 Impact and future perspective

In minimally invasive surgery, a great interest is shown for robotic-assisted percutaneous interventions. In this context, multiple steerable needle designs have been proposed which have the advantage of performing curvilinear trajectories in the tissue and, in doing so, they can increase the range of possible insertion paths or, in cluttered workspace, the probability to find one. This technology aims at setting new standards in terms of targeting and insertion accuracy. In this perspective, this PhD dissertation proposed methods to address two open issues in steerable needle percutaneous interventions: the path planning and the real-time full pose needle estimation required to track the needle torsion during the insertion.

Concerning the first point, although the planner herein presented is suited for the PBN design, the approach used to confine the search volume within a kinematically reachable space as well as the proposed optimization algorithm can potentially be used with needles featuring different designs and/or steering mechanisms (e.g., standard bevel-tip needles or duty-cycle bevel-tip needles), provided that the needle kinematic limits are known.

In our path planner, the computational time represents a point of potential improvement. Many efforts have been lately put on multi-disciplinary approaches to increase the performance of steerable needle path planning, like the combination of sampling-based or kinematic-based methods with Reinforcement Learning. We plan to investigate the use of this technique to further reduce the time required for the path computation.

Concerning the full pose estimation solution proposed in this thesis, it is also potentially extendable to other needle designs. A possible candidate is represented by the bevel-tip needle with base rotation, the kinematic model of which is reported in Kallem and Cowan, 2009. In this case, the needle tip position could be tracked and, similarly to the method presented in this thesis,

a state variable representing the torsional mismatch between the tip and the base of the needle could be included in the model to correct the needle pose estimation.

Improvements in estimation performance could be achieved by including the orientation measurements provided by 5 DoF electromagnetic sensors. These, along with the benefits deriving by using different filtering solutions such as Unscented Kalman or particle filters, will be objects of future studies.

5.1 Scientific publications

5.1.1 Journal publications

A. Favaro, R. Secoli, F. R. Y. Baena and E. De Momi, "Model-based robust pose estimation for a multi-segment, programmable bevel-tip steerable needle", *Robotics and Automation Letters (RA-L)*, under review

A. Favaro, A. Segato, F. Muretti and E. De Momi, "An evolutionary-optimized surgical path planner for a programmable bevel-tip needle", *IEEE Transaction on Robotics (TRO)*, under review

A. Segato, V. Pieri, **A. Favaro**, M. Riva, A. Falini, E. De Momi and A. Castellano, "Automated Steerable Path Planning for Deep Brain Stimulation Safeguarding Fiber Tracts and Deep Gray Matter Nuclei", *Frontiers in Robotics and AI*, vol. 6, 8 2019

5.1.2 Conference proceedings

A. Favaro, R. Secoli, F. R. Y. Baena and E. De Momi, "Optimal pose estimation method for a multi-segment, programmable bevel-tip steerable needle", *International Conference on Intelligent Robots and Systems (IROS)*, under review

A. Favaro, L. Cerri, S. Galvan, F. R. Y. Baena, and E. De Momi, "Automatic Optimized 3D Path Planner for Steerable Catheters with Heuristic Search and

Uncertainty Tolerance” in *2018 IEEE International Conference on Robotics and Automation (ICRA)*, IEEE, 5 2018, pp. 9–16.

A. Favaro, L. Cerri, D. Scorza and E. DeMomi, “Automatic multi-trajectory planning solution for steerable catheters”, in *2018 International Symposium on Medical Robotics (ISMR)* IEEE, 3 2018, pp. 1–6.

A. Favaro; A. Lad, D. Formenti, D. D. Zani, E. De Momi, “Straight trajectory planning for keyhole neurosurgery in sheep with automatic brain structures segmentation”, in *SPIE Medical Imaging*, R. J. Webster and B. Fei, Eds. International Society for Optics and Photonics, 3 2017, p. 101352E.

Chapter 6

Appendices

6.1 Discretization of the independent variable u

The independent variable $u \in [0, 1]$ used to defined the NURBS curve in parametric form is discretized in order to compute the parameters of Section 3.3.3. This is performed according to a discretization parameter δ determined empirically and linked to the number $N_{\mathbf{P},j}$ of control points $\mathbf{P}_k \in \text{sol}_j$, such that:

$$\delta = \begin{cases} 0.1 & \text{if } N_{\mathbf{P},j} = 2 \\ 0.01 & \text{if } N_{\mathbf{P},j} = 3 \\ 0.001 & \text{if } N_{\mathbf{P},j} \geq 4 \end{cases}$$

6.2 Mutation algorithm

If $\{P_o\} \neq \emptyset$ (Line 2, Figure 3.4a), the set of control points $\{\mathbf{P}_o^{critic}\}$ that control parts of $\text{ind}_t^{j,i,a}$ where the condition $\{P_o\} \neq \emptyset$ happens is defined (Line 3). Iterating over all $\mathbf{P}_k \in \{\mathbf{P}_o^{critic}\}$ (Line 4), the weights $w_{k,t}^{j,i,a}$ is increased (Line 8) to push $\text{ind}_t^{j,i,a}$ away from the obstacle until the condition $\{P_o^k\} = \emptyset$ is reached (i.e. obstacle avoidance is achieved within the part of $\text{ind}_t^{j,i,a}$ controlled by \mathbf{P}_k , Line 7). If the weight modification leads to exceed k_{PBN} or to approach another obstacle located in the same section controlled by \mathbf{P}_k ($\#\{P_c^k\}^n > \#\{P_c^k\}$, Line 11), the weight variation (Δ) is reduced, according to a “divide and conquer” approach, as in Favaro et al., 2018b, provided that the stop condition $\Delta/2 < \Delta_{thr}$ is maintained (Lines 12-15). If $\text{ind}_t^{j,i,a}$ is feasible (i.e. $\{P_o\} = \emptyset$ and

$\{P_c\} = \emptyset$, Line 16, Figure 3.4b), all $w_{k,t}^{j,i,a}$ with $k = 2, \dots, N_{\mathbf{p},j}^{i,a} - 1$ (i.e. all weights except the ones associated to $EP_{i,a}$ and TP , Line 17) are decreased (Line 21) in order to smooth the curve and reduce its total length provided that the weight reduction does not generate obstacle collision and complies with a limit of flatness, which correspond to a stop condition (Lines 20). In case obstacle collision occurs, the “divide and conquer” approach is used (Lines 25-28).

Algorithm 1 Mutation($\text{ind}_t^{j,i,a}$)

```

1:  $\{P_c\}, \{P_o\} = \text{verify}(\text{ind}_t^{j,i,a})$ 
2: if  $\{P_o\} \neq \emptyset$  then
3:    $\{\mathbf{P}_o^{critic}\} = \text{controlPointsObs}(\text{ind}_t^{j,i,a}, \mathbf{P}_k)$ 
4:   for all  $\{\mathbf{P}_k\} \in \{\mathbf{P}_o^{critic}\}$  do
5:      $\{P_c^k\}, \{P_o^k\} = \text{verify}(\text{ind}_t^{j,i,a}, \mathbf{P}_k)$ 
6:      $\text{reset}(\Delta)$ 
7:     while  $\{P_o^k\} \neq \emptyset$  do
8:        $w_{k,t}^{j,i,a} = w_{k,t}^{j,i,a} + \Delta$ 
9:        $\text{update}(\text{ind}_t^{j,i,a})$ 
10:       $\{P_c^k\}^n \{P_o^k\}^n = \text{verify}(\text{ind}_t^{j,i,a})$ 
11:      if  $\#\{P_c^k\}^n > \#\{P_c^k\}$  or
         $\#\{P_o^k\}^n > \#\{P_o^k\}$  then
12:         $w_{k,t}^{j,i,a} = w_{k,t}^{j,i,a} - \Delta$ 
13:         $\text{update}(\text{ind}_t^{j,i,a})$ 
14:        if  $\Delta/2 < \Delta_{thr}$  then break
15:        else  $\Delta = \Delta/2$ 
16:        end if
17:      end if
18:    end while
19:  end for
20: end if
21: if  $\{P_c\} = \emptyset$  and  $\{P_o\} = \emptyset$  then
22:   for all  $\{w_{k,t}^{j,i,a}, k = 2, \dots, N_{\mathbf{P},j}^{i,a} - 1\}$  do
23:      $\{P_o^k\} = \text{verify}(\text{ind}_t^{j,i,a}, \mathbf{P}_k)$ 
24:      $\text{reset}(\Delta)$ 
25:     while  $\{P_o^k\} = \emptyset$  and  $\text{ind}_t^{j,i,a} > k_{thr}$  do
26:        $w_{k,t}^{j,i,a} = w_{k,t}^{j,i,a} - \Delta$ 
27:        $\text{update}(\text{ind}_t^{j,i,a})$ 
28:        $\{P_o^k\}^{new} = \text{verify}(\text{ind}_t^{j,i,a})$ 
29:       if  $\{P_o^k\}^{new} \neq \emptyset$  then
30:          $w_{k,t}^{j,i,a} = w_{k,t}^{j,i,a} + \Delta$ 
31:          $\text{update}(\text{ind}_t^{j,i,a})$ 
32:         if  $\Delta/2 < \Delta_{thr}$  then break
33:         else  $\Delta = \Delta/2$ 
34:         end if
35:       end if
36:     end while
37:   end for
38: end if return  $\text{ind}_t^{j,i,a}$ 

```

Bibliography

- Abayazid, Momen, Marco Kemp, and Sarthak Misra (May 2013). "3D flexible needle steering in soft-tissue phantoms using Fiber Bragg Grating sensors". In: *Proceedings - IEEE International Conference on Robotics and Automation*. IEEE, pp. 5843–5849. ISBN: 9781467356411. DOI: 10.1109/ICRA.2013.6631418.
- Abayazid, Momen et al. (Jan. 2015). "Ultrasound-guided three-dimensional needle steering in biological tissue with curved surfaces". In: *Medical Engineering and Physics* 37.1, pp. 145–150. ISSN: 18734030. DOI: 10.1016/j.medengphy.2014.10.005.
- Abolhassani, Niki, Rajni Patel, and Mehrdad Moallem (2007). "Needle insertion into soft tissue: A survey". In: *Medical Engineering and Physics* 29.4, pp. 413–431. ISSN: 13504533. DOI: 10.1016/j.medengphy.2006.07.003.
- Alterovitz, Ron, Sachin Patil, and Anna Derbakova (2011). "Rapidly-exploring roadmaps: Weighing exploration vs. refinement in optimal motion planning". In: *Proceedings - IEEE International Conference on Robotics and Automation*, pp. 3706–3712. ISBN: 9781612843865. DOI: 10.1109/ICRA.2011.5980286.
- Alterovitz, Ron, Thierry Siméon, and Ken Goldberg (2008). "The stochastic motion roadmap: A sampling framework for planning with Markov motion uncertainty". In: *Robotics: Science and Systems*. ISBN: 9780262524841. DOI: 10.7551/mitpress/7830.003.0031.
- Baek, Donghoon et al. (2018). "Path Planning for Automation of Surgery Robot based on Probabilistic Roadmap and Reinforcement Learning". In: *2018 15th International Conference on Ubiquitous Robots, UR 2018*, pp. 342–347. ISBN: 9781538663349. DOI: 10.1109/URAI.2018.8441801.

- Baykal, Cenk, Chris Bowen, and Ron Alterovitz (2019). "Asymptotically optimal kinematic design of robots using motion planning". In: *Autonomous Robots* 43.2, pp. 345–357. ISSN: 15737527. DOI: 10.1007/s10514-018-9766-x.
- Berg, Nick J. van de, Jenny Dankelman, and John J. van den Dobbela (2015). "Design of an actively controlled steerable needle with tendon actuation and FBG-based shape sensing". In: *Medical Engineering and Physics*. ISSN: 18734030. DOI: 10.1016/j.medengphy.2015.03.016.
- Berg, Nick J. van de et al. (Oct. 2015). "Design Choices in Needle Steering—A Review". In: *IEEE/ASME Transactions on Mechatronics* 20.5, pp. 2172–2183. ISSN: 1083-4435. DOI: 10.1109/TMECH.2014.2365999.
- Bergeles, Christos and Pierre E. Dupont (2013). "Planning stable paths for concentric tube robots". In: *IEEE International Conference on Intelligent Robots and Systems*, pp. 3077–3082. ISBN: 9781467363587. DOI: 10.1109/IROS.2013.6696792.
- Bernardes, M. C. et al. (2011). "Adaptive path planning for steerable needles using duty-cycling". In: DOI: 10.1109/iros.2011.6094594.
- Bernardes, M. C. et al. (Sept. 2013). "Robot-assisted automatic insertion of steerable needles with closed-loop imaging feedback and intraoperative trajectory replanning". In: *Mechatronics* 23.6, pp. 630–645. ISSN: 09574158. DOI: 10.1016/j.mechatronics.2013.06.004. URL: <https://linkinghub.elsevier.com/retrieve/pii/S0957415813001177>.
- Bernardes, Mariana C. et al. (2012). "Semi-automatic needle steering system with robotic manipulator". In: *Proceedings - IEEE International Conference on Robotics and Automation*, pp. 1595–1600. ISBN: 9781467314039. DOI: 10.1109/ICRA.2012.6225185.
- Burgner-Kahrs, Jessica, D. Caleb Rucker, and Howie Choset (Dec. 2015). "Continuum Robots for Medical Applications: A Survey". In: *IEEE Transactions on Robotics* 31.6, pp. 1261–1280. ISSN: 15523098. DOI: 10.1109/TRO.2015.2489500.
- Caborni, Chiara et al. (June 2012). "Risk-based path planning for a steerable flexible probe for neurosurgical intervention". In: *2012 4th IEEE RAS & EMBS International Conference on Biomedical Robotics and Biomechatronics (BioRob)*.

- IEEE, pp. 866–871. ISBN: 978-1-4577-1200-5. DOI: 10.1109/BioRob.2012.6290859. URL: <http://ieeexplore.ieee.org/document/6290859/>.
- Chatelain, Pierre, Alexandre Krupa, and Maud Marchal (May 2013). “Real-time needle detection and tracking using a visually servoed 3D ultrasound probe”. In: *2013 IEEE International Conference on Robotics and Automation*. IEEE, pp. 1676–1681. ISBN: 978-1-4673-5643-5. DOI: 10.1109/ICRA.2013.6630795.
- Cowan, Noah J. et al. (2011). “Robotic needle steering: Design, modeling, planning, and image guidance”. In: *Surgical Robotics: Systems Applications and Visions*. Boston, MA: Springer US, pp. 557–582. ISBN: 9781441911254. DOI: 10.1007/978-1-4419-1126-1{_}23.
- Danielsson, Per Erik (Nov. 1980). “Euclidean distance mapping”. In: *Computer Graphics and Image Processing* 14.3, pp. 227–248. ISSN: 0146664X. DOI: 10.1016/0146-664X(80)90054-4. URL: <http://linkinghub.elsevier.com/retrieve/pii/0146664X80900544>.
- De Momi, E. et al. (Nov. 2014). “Multi-trajectories automatic planner for StereoElectroEncephaloGraphy (SEEG)”. In: *International Journal of Computer Assisted Radiology and Surgery* 9.6, pp. 1087–1097. ISSN: 18616429. DOI: 10.1007/s11548-014-1004-1. URL: <http://link.springer.com/10.1007/s11548-014-1004-1>.
- Duindam, Vincent et al. (June 2010). “Three-dimensional motion planning algorithms for steerable needles using inverse kinematics”. In: *International Journal of Robotics Research* 29.7, pp. 789–800. ISSN: 02783649. DOI: 10.1177/0278364909352202. URL: <http://journals.sagepub.com/doi/10.1177/0278364909352202>.
- Engh, Johnathan A. et al. (Oct. 2010). “Percutaneous intracerebral navigation by duty-cycled spinning of flexible bevel-tipped needles”. In: *Neurosurgery* 67.4, pp. 1117–1122. ISSN: 0148396X. DOI: 10.1227/NEU.0b013e3181ec1551. URL: <https://academic.oup.com/neurosurgery/article/67/4/1117/2556761>.
- Essert, Caroline et al. (2012). “Automatic computation of electrode trajectories for Deep Brain Stimulation: A hybrid symbolic and numerical approach”. In: *International Journal of Computer Assisted Radiology and Surgery* 7.4, pp. 517–532. ISSN: 18616429. DOI: 10.1007/s11548-011-0651-8.

- Fausser, Johannes, Georgios Sakas, and Anirban Mukhopadhyay (2018). "Planning nonlinear access paths for temporal bone surgery". In: *International Journal of Computer Assisted Radiology and Surgery*. ISSN: 18616429. DOI: 10.1007/s11548-018-1712-z.
- Fausser, Johannes et al. (2019a). "Planning for flexible surgical robots via bézier spline translation". In: *IEEE Robotics and Automation Letters*. ISSN: 23773766. DOI: 10.1109/LRA.2019.2926221.
- Fausser, Johannes et al. (2019b). "Toward an automatic preoperative pipeline for image-guided temporal bone surgery". In: *International Journal of Computer Assisted Radiology and Surgery*. ISSN: 18616429. DOI: 10.1007/s11548-019-01937-x.
- Favaro, Alberto et al. (Mar. 2018a). "Automatic multi-trajectory planning solution for steerable catheters". In: *2018 International Symposium on Medical Robotics, ISMR 2018*. Vol. 2018-Janua. IEEE, pp. 1–6. ISBN: 9781538625125. DOI: 10.1109/ISMR.2018.8333284. URL: <http://ieeexplore.ieee.org/document/8333284/>.
- Favaro, Alberto et al. (May 2018b). "Automatic Optimized 3D Path Planner for Steerable Catheters with Heuristic Search and Uncertainty Tolerance". In: *Proceedings - IEEE International Conference on Robotics and Automation*. IEEE. IEEE, pp. 9–16. ISBN: 9781538630815. DOI: 10.1109/ICRA.2018.8461262. URL: <https://ieeexplore.ieee.org/document/8461262/>.
- Fischl, Bruce (Aug. 2012). "FreeSurfer". In: *NeuroImage* 62.2, pp. 774–781. ISSN: 10538119. DOI: 10.1016/j.neuroimage.2012.01.021. URL: <http://linkinghub.elsevier.com/retrieve/pii/S1053811912000389>.
- Fu, Mengyu et al. (2018). "Safe Motion Planning for Steerable Needles Using Cost Maps Automatically Extracted from Pulmonary Images". In: *IEEE International Conference on Intelligent Robots and Systems*, pp. 4942–4949. ISBN: 9781538680940. DOI: 10.1109/IROS.2018.8593407.
- Gammell, Jonathan D., Siddhartha S. Srinivasa, and Timothy D. Barfoot (May 2015). "Batch Informed Trees (BIT): Sampling-based optimal planning via the heuristically guided search of implicit random geometric graphs". In: *Proceedings - IEEE International Conference on Robotics and Automation 2015-June*. June, pp. 3067–3074. ISSN: 10504729. DOI: 10.1109/ICRA.2015.7139620. URL: <http://arxiv.org/abs/1405.5848>.

- Gilbert, Hunter B., D. Caleb Rucker, and Robert J. Webster (2016). "Concentric tube robots: The state of the art and future directions". In: *Springer Tracts in Advanced Robotics*. Vol. 114, pp. 253–269. ISBN: 9783319288703. DOI: 10.1007/978-3-319-28872-7{_}15.
- Glozman, Daniel and Moshe Shoham (June 2007). "Image-guided robotic flexible needle steering". In: *IEEE Transactions on Robotics* 23.3, pp. 459–467. ISSN: 15523098. DOI: 10.1109/TRO.2007.898972. URL: <http://ieeexplore.ieee.org/document/4252165/>.
- Hart, Peter E et al. (1968). "A Formal Basis for the Heuristic Determination of Minimum Cost Paths". In: *IEEE Transactions on Systems Science and Cybernetics*. ISSN: 0212-1611. DOI: 10.3305/nh.2014.29.1.7039.
- Hong, Ayoung et al. (2019). "3D path planning for flexible needle steering in neurosurgery". In: *International Journal of Medical Robotics and Computer Assisted Surgery*. ISSN: 1478596X. DOI: 10.1002/rcs.1998.
- Jalel, Sawssen, Philippe Marthon, and Atef Hamouda (2015). "Optimized NURBS Curves Modelling Using Genetic Algorithm for Mobile Robot Navigation". In: *Lecture Notes in Computer Science (including subseries Lecture Notes in Artificial Intelligence and Lecture Notes in Bioinformatics)*, pp. 534–545. ISBN: 9783319231914. DOI: 10.1007/978-3-319-23192-1{_}45.
- Jijie, Xu et al. (2008). "Motion planning for steerable needles in 3D environments with obstacles using Rapidly-exploring random trees and backchaining". In: *4th IEEE Conference on Automation Science and Engineering, CASE 2008*. ISBN: 9781424420230. DOI: 10.1109/COASE.2008.4626486.
- Jordan, Matthew and Alejandro Perez (2013). "Optimal Bidirectional Rapidly-Exploring Random Trees". In: *Computer Science and Artificial Intelligence Laboratory*.
- Kallem, Vinutha and Noah J. Cowan (Feb. 2009). "Image guidance of flexible tip-steerable needles". In: *IEEE Transactions on Robotics* 25.1, pp. 191–196. ISSN: 15523098. DOI: 10.1109/TRO.2008.2010357.
- Karaman, Sertac and Emilio Frazzoli (June 2011). "Sampling-based algorithms for optimal motion planning". In: *International Journal of Robotics Research* 30.7, pp. 846–894. ISSN: 02783649. DOI: 10.1177/0278364911406761. URL: <http://journals.sagepub.com/doi/10.1177/0278364911406761>.

- Karaman, Sertac et al. (2011). "Anytime motion planning using the RRT". In: *Proceedings - IEEE International Conference on Robotics and Automation*. ISBN: 9781612843865. DOI: 10.1109/ICRA.2011.5980479.
- Kavraki, Lydia E. and Steven M. LaValle (2016). "Motion planning". In: *Springer Handbook of Robotics*, pp. 139–161. ISBN: 9783319325521. DOI: 10.1007/978-3-319-32552-1{_}7.
- Kavraki, Lydia E. et al. (1996). "Probabilistic roadmaps for path planning in high-dimensional configuration spaces". In: *IEEE Transactions on Robotics and Automation*. ISSN: 1042296X. DOI: 10.1109/70.508439.
- Khan, Fouzia et al. (July 2019). "Multi-Core Optical Fibers With Bragg Gratings as Shape Sensor for Flexible Medical Instruments". In: *IEEE Sensors Journal* 19.14, pp. 5878–5884. ISSN: 1530-437X. DOI: 10.1109/JSEN.2019.2905010.
- Khatib, Oussama (1986). "Real-Time Obstacle Avoidance for Manipulators and Mobile Robots". In: *Autonomous Robot Vehicles*. Ed. by Ingemar J Cox and Gordon T Wilfong. New York, NY: Springer New York, pp. 396–404. ISBN: 978-1-4613-8997-2. DOI: 10.1007/978-1-4613-8997-2{_}29. URL: http://link.springer.com/10.1007/978-1-4613-8997-2_29.
- Ko, Seong Young, Luca Frasson, and Ferdinando Rodriguez Y Baena (Oct. 2011). "Closed-loop planar motion control of a steerable probe with a programmable bevel inspired by nature". In: *IEEE Transactions on Robotics* 27.5, pp. 970–983. ISSN: 15523098. DOI: 10.1109/TRO.2011.2159411.
- Kuffner, James J. and Steven M. La Valle (2000a). "RRT-connect: an efficient approach to single-query path planning". In: *Proceedings - IEEE International Conference on Robotics and Automation*. Vol. 2, pp. 995–1001. DOI: 10.1109/robot.2000.844730.
- (2000b). "RRT-connect: an efficient approach to single-query path planning". In: *Proceedings - IEEE International Conference on Robotics and Automation*. Vol. 2. IEEE, pp. 995–1001. ISBN: 0-7803-5886-4. DOI: 10.1109/robot.2000.844730. URL: <http://ieeexplore.ieee.org/document/844730/>.
- Kuntz, Alan et al. (Sept. 2015). "Motion planning for a three-stage multilumen transoral lung access system". In: *IEEE International Conference on Intelligent Robots and Systems*. Vol. 2015-Decem. IEEE, pp. 3255–3261. ISBN:

9781479999941. DOI: 10.1109/IROS.2015.7353829. URL: <http://ieeexplore.ieee.org/document/7353829/>.
- LaValle, S M (1998). "Rapidly-Exploring Random Trees: A New Tool for Path Planning". In: *In*. ISSN: 1098-6596. DOI: 10.1.1.35.1853.
- Leibrandt, Konrad, Christos Bergeles, and Guang Zhong Yang (2016). "Implicit active constraints for safe and effective guidance of unstable concentric tube robots". In: *IEEE International Conference on Intelligent Robots and Systems*. Vol. 2016-Novem, pp. 1157–1163. ISBN: 9781509037629. DOI: 10.1109/IROS.2016.7759195.
- (June 2017). "Concentric Tube Robots: Rapid, Stable Path-Planning and Guidance for Surgical Use". In: *IEEE Robotics & Automation Magazine* 24.2, pp. 42–53. ISSN: 1070-9932. DOI: 10.1109/MRA.2017.2680546. URL: <http://ieeexplore.ieee.org/document/7927737/>.
- Li, Pan et al. (2014). "A combination method of artificial potential field and improved conjugate gradient for trajectory planning for needle insertion into soft tissue". In: *Journal of Medical and Biological Engineering* 34.6, pp. 568–573. ISSN: 16090985. DOI: 10.5405/jmbe.1804. URL: <http://jmbe.bme.ncku.edu.tw/AIP/AIP-JMBE1804.pdf>.
- Likhachev, Maxim et al. (2005). "Anytime Dynamic A*: An Anytime, Replanning Algorithm." In: *ICAPS*, pp. 262–271.
- Liu, Fangde et al. (July 2016). "Fast and Adaptive Fractal Tree-Based Path Planning for Programmable Bevel Tip Steerable Needles". In: *IEEE Robotics and Automation Letters* 1.2, pp. 601–608. ISSN: 2377-3766. DOI: 10.1109/LRA.2016.2528292.
- Lobaton, Edgar et al. (2011). "Planning curvature-constrained paths to multiple goals using circle sampling". In: *Proceedings - IEEE International Conference on Robotics and Automation*, pp. 1463–1469. ISBN: 9781612843865. DOI: 10.1109/ICRA.2011.5980446.
- Misra, S. et al. (Nov. 2010). "Mechanics of flexible needles robotically steered through soft tissue". In: *International Journal of Robotics Research* 29.13, pp. 1640–1660. ISSN: 02783649. DOI: 10.1177/0278364910369714.
- Navaei Lavasani, Saeedeh et al. (2020). "Compensation of dynamic electromagnetic field distortion using simultaneous localization and mapping

- method with application in endobronchial ultrasound-transbronchial needle aspiration (EBUS-TBNA) guidance". In: *International Journal of Medical Robotics and Computer Assisted Surgery*. ISSN: 1478596X. DOI: 10.1002/rcs.2035.
- Okazawa, Stephen et al. (2005). "Hand-held steerable needle device". In: *IEEE/ASME Transactions on Mechatronics*. ISSN: 10834435. DOI: 10.1109/TMECH.2005.848300.
- Patil, Sachin and Ron Alterovitz (Sept. 2010). "Interactive motion planning for steerable needles in 3D environments with obstacles". In: *2010 3rd IEEE RAS and EMBS International Conference on Biomedical Robotics and Biomechanics, BioRob 2010*, pp. 893–899. ISSN: 2155-1774. DOI: 10.1109/BIOROB.2010.5625965. URL: <http://ieeexplore.ieee.org/document/5625965/>.
- Patil, Sachin, Jur Van Den Berg, and Ron Alterovitz (2012). "Motion planning under uncertainty in highly deformable environments". In: *Robotics: Science and Systems*. Vol. 7, pp. 241–248. ISBN: 9780262517799. DOI: 10.7551/mitpress/9481.003.0036.
- Patil, Sachin et al. (2014). "Needle steering in 3-D Via rapid replanning". In: *IEEE Transactions on Robotics* 30.4, pp. 853–864. ISSN: 15523098. DOI: 10.1109/TRO.2014.2307633.
- Petruska, Andrew J. et al. (2016). "Magnetic needle guidance for neurosurgery: Initial design and proof of concept". In: *Proceedings - IEEE International Conference on Robotics and Automation*. Vol. 2016-June, pp. 4392–4397. ISBN: 9781467380263. DOI: 10.1109/ICRA.2016.7487638.
- Piegl, Les and Wayne Tiller (Aug. 1996). "The NURBS Book". In: *Computer-Aided Design* 28.8, pp. 665–666. ISSN: 00104485. DOI: 10.1016/0010-4485(96)86819-9. URL: <http://linkinghub.elsevier.com/retrieve/pii/0010448596868199>.
- Pinzi, Marlene, Stefano Galvan, and Ferdinando Rodriguez y Baena (2019). *The Adaptive Hermite Fractal Tree (AHFT): a novel surgical 3D path planning approach with curvature and heading constraints*. DOI: 10.1007/s11548-019-01923-3.
- Ralovich, Kristóf et al. (2014). "6DoF catheter detection, application to intracardiac echocardiography". In: *Medical image computing and computer-assisted*

- intervention : MICCAI ... International Conference on Medical Image Computing and Computer-Assisted Intervention* 17.Pt 2, pp. 635–642. ISSN: 16113349. DOI: 10.1007/978-3-319-10470-6{_}79.
- Razali, Noraini Mohd and John Geraghty (2011). “Genetic algorithm performance with different selection strategies in solving TSP”. In: *Proceedings of the World Congress on Engineering 2011*, pp. 1134–1139. ISBN: 9789881925145. DOI: 10.1053/joms.2000.16615.
- Reed, K.B., A.M. Okamura, and N.J. Cowan (Dec. 2009). “Modeling and Control of Needles With Torsional Friction”. In: *IEEE Transactions on Biomedical Engineering* 56.12, pp. 2905–2916. ISSN: 0018-9294. DOI: 10.1109/TBME.2009.2029240.
- Reed, Kyle B. et al. (2008). “Integrated planning and image-guided control for planar needle steering”. In: *Proceedings of the 2nd Biennial IEEE/RAS-EMBS International Conference on Biomedical Robotics and Biomechatronics, BioRob 2008*. ISBN: 9781424428830. DOI: 10.1109/BIOROB.2008.4762833.
- Reed, Kyle B. et al. (Dec. 2011). “Robot-assisted needle steering”. In: *IEEE Robotics and Automation Magazine* 18.4, pp. 35–46. ISSN: 10709932. DOI: 10.1109/MRA.2011.942997.
- Rossa, Carlos and Mahdi Tavakoli (2017). “Issues in closed-loop needle steering”. In: *Control Engineering Practice*. ISSN: 09670661. DOI: 10.1016/j.conengprac.2017.03.004.
- Rucker, D. Caleb, Bryan A. Jones, and Robert J. Webster (May 2010). “A model for concentric tube continuum robots under applied wrenches”. In: *Proceedings - IEEE International Conference on Robotics and Automation*. IEEE, pp. 1047–1052. ISBN: 9781424450381. DOI: 10.1109/ROBOT.2010.5509701. URL: <http://ieeexplore.ieee.org/document/5509701/>.
- Rucker, Daniel Caleb (2011). “The mechanics of continuum robots: Model-based sensing and control”. In: *Ph.D thesis, Graduate school of Vanderbilt University* 3506877, p. 197. URL: <http://search.proquest.com/docview/1011310658?accountid=37552>.
- Sadjadi, H., K. Hashtrudi-Zaad, and G. Fichtinger (Aug. 2012). “Needle deflection estimation using fusion of electromagnetic trackers”. In: *2012 Annual*

- International Conference of the IEEE Engineering in Medicine and Biology Society*. IEEE, pp. 952–955. ISBN: 978-1-4577-1787-1. DOI: 10.1109/EMBC.2012.6346090.
- Schulman, John et al. (2014). “Motion planning with sequential convex optimization and convex collision checking”. In: *International Journal of Robotics Research* 33.9, pp. 1251–1270. ISSN: 17413176. DOI: 10.1177/0278364914528132.
- Scorza, Davide et al. (Oct. 2017). “Retrospective evaluation and SEEG trajectory analysis for interactive multi-trajectory planner assistant”. In: *International Journal of Computer Assisted Radiology and Surgery* 12.10, pp. 1727–1738. ISSN: 18616429. DOI: 10.1007/s11548-017-1641-2. URL: <http://link.springer.com/10.1007/s11548-017-1641-2>.
- Secoli, R., F. Rodriguez, and Baena (2018). “Experimental validation of curvature tracking with a programmable bevel-tip steerable needle”. In: *2018 International Symposium on Medical Robotics, ISMR 2018*. Vol. 2018-Janua. IEEE, pp. 1–6. ISBN: 9781538625125. DOI: 10.1109/ISMR.2018.8333302.
- Secoli, Riccardo and Ferdinando Rodriguez Y. Baena (June 2016). “Adaptive path-following control for bio-inspired steerable needles”. In: *Proceedings of the IEEE RAS and EMBS International Conference on Biomedical Robotics and Biomechatronics*. Vol. 2016-July. IEEE, pp. 87–93. ISBN: 9781509032877. DOI: 10.1109/BIOROB.2016.7523603.
- Secoli, Riccardo and Ferdinando Rodriguez Y Baena (2013). “Closed-loop 3D motion modeling and control of a steerable needle for soft tissue surgery”. In: *Proceedings - IEEE International Conference on Robotics and Automation*. IEEE, pp. 5831–5836. ISBN: 9781467356411. DOI: 10.1109/ICRA.2013.6631416.
- Segato, Alice et al. (Aug. 2019). “Automated Steerable Path Planning for Deep Brain Stimulation Safeguarding Fiber Tracts and Deep Gray Matter Nuclei”. In: *Frontiers in Robotics and AI* 6. ISSN: 2296-9144. DOI: 10.3389/frobt.2019.00070. URL: <https://www.frontiersin.org/article/10.3389/frobt.2019.00070/full>.
- Seiler, Konstantin M. et al. (2012). “Using Lie group symmetries for fast corrective motion planning”. In: *International Journal of Robotics Research* 31.2, pp. 151–166. ISSN: 02783649. DOI: 10.1177/0278364911429977.

- Shahriari, Navid et al. (Nov. 2015). "Design and evaluation of a computed tomography (CT)-compatible needle insertion device using an electromagnetic tracking system and CT images". In: *International Journal of Computer Assisted Radiology and Surgery* 10.11, pp. 1845–1852. ISSN: 18616429. DOI: 10.1007/s11548-015-1176-3.
- Smith, David K. (1996). "Dynamic Programming and Optimal Control. Volume 1". In: *Journal of the Operational Research Society* 47.6, pp. 833–834. ISSN: 0160-5682. DOI: 10.1057/jors.1996.103.
- Sudhakara, Priyanka, Velappa Ganapathy, and Karthika Sundaran (Mar. 2018). "Trajectory Planning Using Enhanced Probabilistic Roadmaps For Pliable Needle Robotic Surgery". In: *2018 International Conference on Recent Trends in Electrical, Control and Communication (RTECC)*. IEEE, pp. 61–64. ISBN: 978-1-5386-4310-5. DOI: 10.1109/RTECC.2018.8625678. URL: <https://ieeexplore.ieee.org/document/8625678/>.
- Sun, Wen, Sachin Patil, and Ron Alterovitz (2015). "High-frequency replanning under uncertainty using parallel sampling-based motion planning". In: *IEEE Transactions on Robotics* 31.1, pp. 104–116. ISSN: 15523098. DOI: 10.1109/TRO.2014.2380273.
- Swensen, John P. et al. (Nov. 2014). "Torsional dynamics of steerable needles: Modeling and fluoroscopic guidance". In: *IEEE Transactions on Biomedical Engineering* 61.11, pp. 2707–2717. ISSN: 15582531. DOI: 10.1109/TBME.2014.2326161.
- Torabi, Meysam et al. (2009). "Guiding medical needles using single-point tissue manipulation". In: *Proceedings - IEEE International Conference on Robotics and Automation*. ISBN: 9781424427895. DOI: 10.1109/ROBOT.2009.5152853.
- Torres, Luis G. and Ron Alterovitz (2011). "Motion planning for concentric tube robots using mechanics-based models". In: pp. 5153–5159. DOI: 10.1109/iro.2011.6095168.
- Torres, Luis G., Cenk Baykal, and Ron Alterovitz (2014). "Interactive-rate motion planning for concentric tube robots". In: *Proceedings - IEEE International Conference on Robotics and Automation*, pp. 1915–1921. DOI: 10.1109/ICRA.2014.6907112.

- Vrooijink, Gustaaf J., Momen Abayazid, and Sarthak Misra (May 2013). "Real-time three-dimensional flexible needle tracking using two-dimensional ultrasound". In: *Proceedings - IEEE International Conference on Robotics and Automation*. IEEE, pp. 1688–1693. ISBN: 9781467356411. DOI: 10.1109/ICRA.2013.6630797.
- Vrooijink, Gustaaf J. et al. (2014). "Needle path planning and steering in a three-dimensional non-static environment using two-dimensional ultrasound images". In: *International Journal of Robotics Research* 33.10, pp. 1361–1374. ISSN: 17413176. DOI: 10.1177/0278364914526627.
- Watts, Thomas, Riccardo Secoli, and Ferdinando Rodriguez Y. Baena (Apr. 2019). "A Mechanics-Based Model for 3-D Steering of Programmable Bevel-Tip Needles". In: *IEEE Transactions on Robotics* 35.2, pp. 371–386. ISSN: 15523098. DOI: 10.1109/TRO.2018.2879584.
- Webster, Robert J. et al. (2006). "Nonholonomic modeling of needle steering". In: *Springer Tracts in Advanced Robotics*. Vol. 21, pp. 35–44. ISBN: 3540288163. DOI: 10.1007/11552246{_}4.
- Wooram Park et al. (2005). "Diffusion-Based Motion Planning for a Nonholonomic Flexible Needle Model". In: *Proceedings of the 2005 IEEE International Conference on Robotics and Automation*. Vol. 2005. IEEE, pp. 4600–4605. ISBN: 0-7803-8914-X. DOI: 10.1109/ROBOT.2005.1570829.
- Yang, Liang et al. (2016). *Survey of Robot 3D Path Planning Algorithms*. DOI: 10.1155/2016/7426913.
- Zhao, Yan-Jiang et al. (2015). "3D Motion Planning for Robot-Assisted Active Flexible Needle Based on Rapidly-Exploring Random Trees". In: *Journal of Automation and Control Engineering*, pp. 360–367. ISSN: 23013702. DOI: 10.12720/joace.3.5.360-367.
- Zhao, Yan Jiang et al. (2016). "3D Dynamic Motion Planning for Robot-Assisted Cannula Flexible Needle Insertion into Soft Tissue". In: *International Journal of Advanced Robotic Systems*. ISSN: 17298814. DOI: 10.5772/64199.